

Errata

In the " χ_{ij} " and the " d_{ij} " notation for the nonlinear susceptibility tensor components, it is understood that $\chi_{ij} = 2d_{ij}$. For all discussions appearing in Section 3 that give numerical values for χ_{ij} , the quantity χ_{ij} should be replaced by $\chi_{ij}/2$. For example, on page 71, column 2, line 13 the phrase, "... $|\chi_{31}|$ (4.6 pm V⁻¹)..." should be replaced by, "... $|\chi_{31}|/2$ (4.6 pmV⁻¹)..." Similarly, in column 2, line 15, $|\chi_{31}| = 5.44$ pm V⁻¹ should be replaced by $|\chi_{31}|/2 = 5.44$ pm V⁻¹, and so on. With these replacements, the discussion on pages 71 and 72 is consistent with the data presented in Fig. 13.

Chapter 2

CRYSTAL GROWTH, CHARACTERIZATION, AND DOMAIN STUDIES IN LITHIUM NIOBATE AND LITHIUM TANTALATE FERROELECTRICS

Venkatraman Gopalan

*Materials Research Laboratory and Department of Materials Science and Engineering,
Pennsylvania State University, University Park, Pennsylvania, USA*

Norman A. Sanford, J. A. Aust

*National Institute of Standards and Technology, Optoelectronics Division 815, Boulder,
Colorado, USA*

K. Kitamura, Y. Furukawa

*National Institute for Research in Inorganic Materials (NIRIM), 13th Research Group,
1-1, Namiki, Tsukuba-shi, 305 Japan*

Contents

1. Introduction	58
2. Crystal Growth with Controlled Lithium Stoichiometry	58
2.1. Introduction	58
2.2. Double Crucible Czochralski Method	59
2.3. Crystal Growth Procedure	60
2.4. Characterization of Grown Crystals of Stoichiometric LiTaO ₃	60
2.5. Characterization of Grown Crystals of Stoichiometric LiNbO ₃	61
2.6. Discussions	61
3. Crystal Uniformity Studies by Maker Fringe Analysis	63
3.1. Introduction	63
3.2. Experimental Apparatus and Data Collection	64
3.3. Modeling of Maker Fringes for <i>x</i> - and <i>z</i> -Cut LiNbO ₃ Wafers	64
3.4. <i>o</i> -Polarized Maker Fringes and Thickness Maps of <i>x</i> -Cut Wafers	67
3.5. <i>e</i> -Polarized Maker Fringes and Variations in Composition of LiNbO ₃ Wafers	69
3.6. Photoelastic Strain Revealed by Perturbations in the Maker Fringes for <i>x</i> -Cut LiNbO ₃	72
3.7. Concluding Remarks	75
4. Ferroelectric Domains and Domain Walls	75
4.1. Introduction	75
4.2. Domain Reversal	76
4.3. Domain Wall Structure	85
5. The Dynamics of Domain Nucleation and Growth	93
5.1. Introduction	93
5.2. Congruent Lithium Tantalate	93
5.3. Congruent Lithium Niobate	107
5.4. Stoichiometric Lithium Niobate and Tantalate	111
6. Concluding Remarks	112
6.1. Summary of Reviewed Work	112

6.2. Fundamental Scientific Issues	112
Acknowledgments	112
References	112

1. INTRODUCTION

Ferroelectricity in lithium niobate (LiNbO_3) and lithium tantalate (LiTaO_3) crystals was discovered by Matthias and Remeika in 1949 [1]. They emerged as key technological materials in the areas of nonlinear optics, [2] integrated optics [3], acoustic wave devices [4], and optical holography [5]. An unprecedented interest in these materials was seen in 1990s. This is seen from Figure 1 which shows the results of a literature search for technical publications relating to either lithium niobate or lithium tantalate. This trend was driven by many factors. The emergence of photonics [6] for communications, data storage, display, biomedical, and defense applications resulted in an increasing need for a versatile solid-state platform with a range of linear and nonlinear optical properties, such as silicon in semiconductor industry. The crystal growth for lithium niobate and lithium tantalate is perfected to an extent that high quality, single crystal, single domain wafers of these materials are available commercially and inexpensively in up to 4 in wafers. Their high electro-optic and nonlinear optical coefficients, transparency in a wavelength range from near UV to far infrared, large photovoltaic, and photocurrents in doped crystals, and the possibility of patterning ferroelectric domains into various shapes and sizes created this surge in interest. As is often the case, a widespread technological application of these materials preceded a complete understanding of many of the fundamental physical processes occurring in these materials. This chapter focuses on four specific areas where significant progress was made in understanding these materials. The first is the growth of single crystals with noncongruent melt compositions. While congruent crystals are excess in Niobium, the growth of crystals with varying [Li] resulted in the discovery that many physical properties sensitively depend on [Li]/[ND] ratio in the crystal. The second area of focus is the study of uniformity in crystal composition, wafer thickness, and strains using the sensitive Maker fringe technique. The third area of focus is a variety of experimental studies on the structure of a ferroelectric domain wall, and strains, electric fields, and optical birefringence associated with these walls. Advances in the phenomenological theory of domain wall structure in LiNbO_3 and LiTaO_3 are also reviewed in the light of these new experimental studies. The fourth area reviews the advances in the real-time studies of the dynamics of antiparallel ferroelectric domains in these materials under external driving forces. While one can observe a moving domain wall on a video monitor today, it is interesting to note that ferroelectric domain reversal in these materials was believed to be impossible at room temperature, hence the nickname "frozen ferroelectric" given to LiNbO_3 by Megaw [7].

The organization of this chapter is as follows. Section 2 discusses the crystal structure and growth of noncongruent single crystals of lithium niobate and lithium tantalate using double crucible Czochralski technique. Section 3 discusses in detail, the technique, theory, and analysis of using Maker fringes to characterize ferroelectric crystals. Section 4 focuses on the phenomena of ferroelectric domains, and discusses ferroelectric hysteresis, internal fields, the role of nonstoichiometry in domain reversal, the structure of a domain wall and its interaction with lattice defects, and

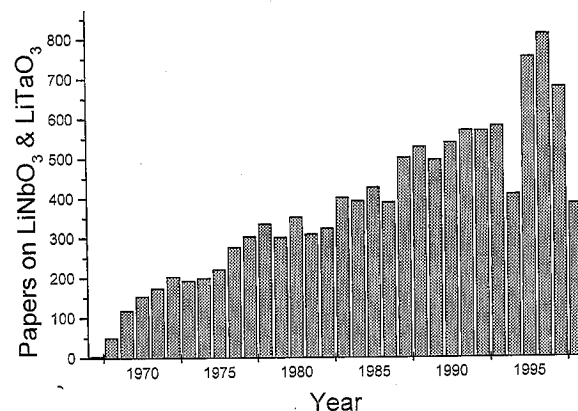


Fig. 1. The trend in the number of publications written on lithium niobate and lithium tantalate ferroelectrics over the years. The data were retrieved by searching for references in every year [yr] using INSPECTM using the search command "BI(LiNbO₃? Or lithium niobate Or LiTaO₃? Or Lithium tantalate) and PY(yr)."

phenomenological modeling of domain wall structure in these materials. Section 5 covers the real-time studies of the dynamics of ferroelectric domains under external driving forces. Section 6 summarizes the current status of understanding of physical processes in these materials, and the open issues that still need to be addressed.

Two excellent reviews on lithium niobate already exist in literature covering a period from early days of discovery to the late 1980s [8, 9]. Considering the current level of activity in this field as evident from Figure 1, a complete review of this field is beyond the scope of this chapter. For the most part, this review is restricted to the work done by the contributing authors, and therefore is not intended to be comprehensive. Specific fields that found extensive development, but are excluded from this review, are device technologies including integrated and nonlinear optics, acoustics, and holographic data storage devices based on LiNbO_3 and LiTaO_3 , variants of the LiNbO_3 and LiTaO_3 structures obtained by doping elements such as hydrogen, Ti, MgO, Fe, and Er, and thin film deposition and characterization of LiNbO_3 and LiTaO_3 .

2. CRYSTAL GROWTH WITH CONTROLLED LITHIUM STOICHIOMETRY

2.1. Introduction

Although commonly referred to as " LiNbO_3 " and " LiTaO_3 ," these phases exist over a wide solid solution range. Figure 2(a) and (b) shows the phase diagrams of Nb_2O_5 - Li_2O and Ta_2O_5 - Li_2O , respectively, near the congruent composition [10, 11]. The congruent melting composition, which is used in the conventional Czochralski (CZ) method for the commercial crystal growth [12], shifts toward the Nb or Ta excess composition side from the stoichiometric composition. Therefore, all LiNbO_3 (to be referred to as LN) and LiTaO_3 (to be referred to as LT) produced commercially should contain large amounts of cation vacancies. The

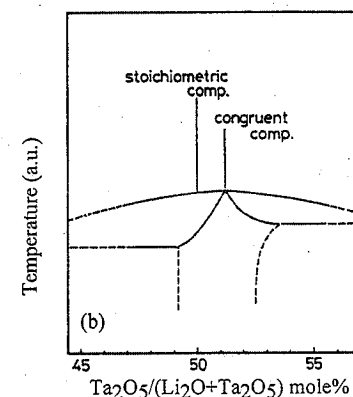
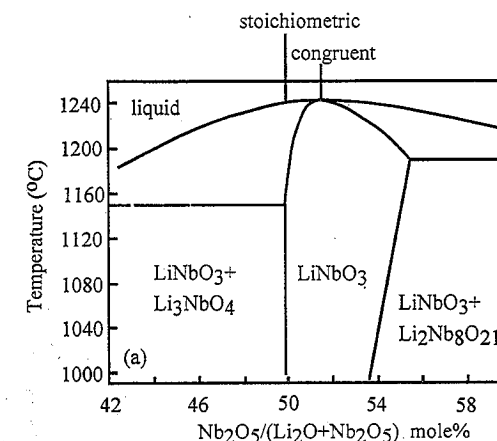


Fig. 2. The phase diagrams of (a) Nb_2O_5 - Li_2O , reprinted with permission from J. R. Carruthers et al., *J. Appl. Phys.*, 42, 1846, (© 1971 Amer. Institute of Phys.) and (b) Ta_2O_5 - Li_2O . Reprinted from *J. Cryst. Growth*, 10, S. Miyazawa and H. Iwasaki, 276, (© 1971), with permission from Elsevier Science.

growth of stoichiometric compositions of these crystals is difficult through conventional Czochralski due to phase separation in growing from lithium-rich melt. This problem was solved by Kitamura et al. [13] and Furukawa et al. [14] by the use of the double crucible Czochralski method (DCCZ). This section primarily reviews the progress in crystal growth by this group. The essential growth procedures are described in detail, and selected characteristics of the grown crystal are presented. As will be seen in later sections, the physical properties of these ferroelectrics such as domain structure, domain switching and internal fields, and the optical properties show a very high sensitivity to the lithium stoichiometry in the crystal. Therefore, the ability to finely control lithium stoichiometry is of immense value.

2.2. Double Crucible Czochralski Method

It can be seen from the Li_2O - Nb_2O_5 phase diagram that the stoichiometric LiNbO_3 crystal coexists in equilibrium with a Li-rich melt (Li_2O 58–60 mol %) [10, 15, 16]. The Li_2O - Ta_2O_5 phase diagram reported by Miyazawa and Iwasaki [11] is very similar to that of the Li_2O - Nb_2O_5 system [10]. It was also shown that the stoichiometric LiTaO_3 crystal coexists in equilibrium with a Li-rich melt (Li_2O 58–60 mol %). Consequently, the stoichiometric LiNbO_3 and LiTaO_3 crystals must be grown from a Li-rich melt of

the appropriate composition. A growth system, named the double crucible Czochralski (DCCZ) method equipped with an automatic powder supply system as schematically shown in Figure 3 was designed by authors [13, 17] to maintain the Li-rich melt from which the stoichiometric LN and LT crystals were grown. The melt in the inner crucible (inner melt) was Li-rich from which the stoichiometric crystals were grown by the Czochralski technique. The composition of the outer melt is maintained to be of stoichiometric composition. Holes in the wall of the inner crucible allows the outer melt to flow into the inner melt. Stoichiometric LN and LT powders were continuously supplied to the outer crucible by an automatic powder supply system at the same rate as the increase in weight of the growing crystal. The principle therefore is to add the material to the outer melt that one removes from the inner melt by crystal growth, such that the lithium composition of the melt does not change.

The growth apparatus designed by the Kitamura et al. [13, 17] consists of three main parts: the double crucible, the automatic powder supply system, and the Czochralski growth apparatus. They are described in detail here.

Double crucible: The crucible materials used normally are platinum for LiNbO_3 and iridium for LiTaO_3 growth. This difference is due to the difference in the melting temperatures of LiNbO_3 ($\sim 1250^\circ\text{C}$) and LiTaO_3 (1650°C). Melting temperature of Pt and Ir are 1770 and 2410°C , respectively. To heat the material above 1600°C , the crucible is heated above 1700°C which is too close to the melting temperature of platinum, and therefore, an iridium crucible is used for LiTaO_3 . However, Pt can be heated in air, while Ir oxidizes easily. Therefore, Pt is preferred for LiNbO_3 crystal growth.

The crucible has a double chamber structure which divides the melt into two parts. The inner crucible is a cylinder (60–85-mm diameter, 55–90-mm height) placed on the bottom of the outer crucible (125-mm diameter, 70-mm height). Three holes are cut symmetrically at the bottom of the inner cylinder. During growth, the melt in the outer crucible can flow into the inner crucible through these slits.

Automatic powder supply system: In the supply system, calcined stoichiometric LN or LT powder is placed in a holding container (hopper) at the top of this apparatus. The powder is delivered from the bottom of this container by a "cork-screw" mechanism. The weight of the holding container including the powder is monitored every second by an electronic balance. The weight decrease per unit time period of the powder in the hopper is always monitored and adjusted to be equal to the calculated crystal growth rate by automatically modifying the rotation rate of the cork-screw mechanism. This is continuously monitored and controlled by computer. The powder expelled from the cork-screw mechanism falls through an alumina tube into the outer melt. The bottom of the alumina tube is positioned a few centimeters above the outer crucible. The powder supply rate could be controlled within a range of $1\text{--}40\text{ g h}^{-1}$. The accuracy of the supply rate in this system depends on the powder conditions. It was found that the supply rate of coarse grained powder was better than the supply rate of fine grained powder in controlling the amount of supplied feedback.

Growth apparatus: The growth apparatus used was of an ordinary CZ furnace equipped with a 30-kW, 20-KHz radio frequency heater. A load cell was equipped with the apparatus to monitor the weight of the growing crystal, and the automatic diameter control program was also used. Crystal growth was also monitored and

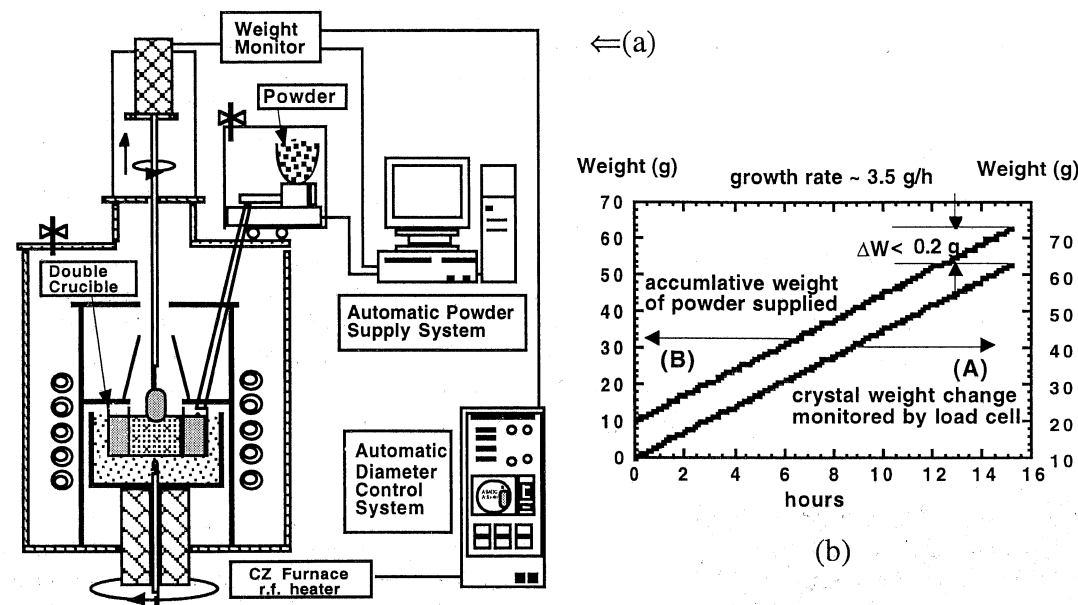


Fig. 3. (a) A schematic of the double crucible Czochralski (DCCZ) method for growing noncongruent compositions of lithium niobate and lithium tantalate. Reprinted from *J. Cryst. Growth*, 116, K. Kitamura et al., 327, © (1992), with permission from Elsevier Science. (b) A plot of crystal weight change and stoichiometric powder weight added to the melt with time. Reprinted from *J. Cryst. Growth*, 197, Y. Furukawa et al., 889, © (1999), with permission from Elsevier Science.

controlled from the office by the remote access control system using a local area network.

2.3. Crystal Growth Procedure

Li_2CO_3 powder of 99.99% purity and Nb_2O_5 or Ta_2O_5 powder of 99.99% purity were mixed at the appropriate proportions in a plastic-ball mill and calcined at 1000°C for 12 h. To obtain the coarse grain powder with stoichiometric composition, the calcined powder was pressed at a hydrostatic pressure of 1.5 ton cm^{-2} . The pressed powder is heated to 1150°C for LN and 1250°C for LT initiating the enhanced grain growth, then the coarse grains of 200 to $500\text{-}\mu\text{m}$ diameter were selected as a feeding material.

The Li-rich (Li_2O 58–60 mol %) powder is pressed under the same conditions and placed in the inner crucible. Stoichiometric composition powder is fed in the outer crucible. Upon heating in the Czochralski furnace, the powder in the outer crucible is completely molten fast to become a heat transfer fluid, and subsequently the powder in the inner crucible starts to melt. This is because the radio frequency power is mainly coupled to the outer crucible and not to the inner crucible. The crucible is rotated at a rate of 0.05–0.1 rpm in the counterdirection to the seed rotation to promote the mixture of feeded stoichiometric powder with Li-rich melt. The crucible is placed at the center of the work coil position and surrounded with a ZrO_2 bubble insulator. The temperature of the bottom crucible and the melt surface are monitored by a thermocouple (type B).

With iridium crucible growth of LT, growth is accomplished in an oxygen and nitrogen gas mixture flow with a volume ratio of oxygen to nitrogen 1:100 to prevent excessive oxidation of the crucible. For platinum crucible growth of LN, growth is performed in air. The humidity of the atmosphere can also be controlled to control hydrogen incorporation in the grown crystal. The growth

direction of crystals can be either the z-axis, which is the polarization axis of the ferroelectric, or the crystallographic y-axis which lies in the mirror plane and normal to the z-axis, or the x-axis which is perpendicular to both the y- and z-axes. The presence of subgrain boundaries in the crystals results in cracking of the crystal [18]. The crystals grown with the y-axis as the growth direction result in the highest quality crystals due to the absence of low angle grain boundaries. The x-axis growth results in the poorest growth quality [18]. The z-axis growth is intermediate between the two. It is observed that in LiNbO_3 , the z-axis and the y-axis growth is relatively easy while the x-axis growth is difficult. In LiTaO_3 , the y-axis growth is the easiest, while z-axis growth and x-axis growth are quite difficult by conventional Czochralski growth.

With the DCCZ method using Li-rich melt, the z-axis growth of crystals has also become easy. Though the reasons for these preferences are not entirely clear, it is believed that, the temperature gradient in the depth direction as well as the radial direction affects the crystal growth and cracking [14]. The seed rotation rate of 4 rpm and the pulling rate of 2.0–0.5 mm are standard for most crystals. The coarse grained stoichiometric powder is supplied at a rate of about $1\text{--}6 \text{ g h}^{-1}$ as determined by the weight increase monitored by the load cell.

2.4. Characterization of Grown Crystals of Stoichiometric LiTaO_3

Figure 4(a) shows examples of as-grown stoichiometric LiTaO_3 crystals grown with the y-axis as the growth direction. The stoichiometric LiTaO_3 crystals are colorless, transparent, and crack-free with a size of 50-mm diameter and 150-mm length. One of the noticeable features of stoichiometric LiTaO_3 is that as-grown crystals are colorless even grown under the reduced atmosphere without oxygen, whereas the congruent crystals get dark color if grown un-

Table I. Curie Temperature and Lattice Parameters of the Grown Stoichiometric LiTaO_3 Crystal*

Sample	Curie temperature T_c ($^\circ\text{C}$)	Lattice parameters (\AA)	
		a_o	c_o
Congruent LiTaO_3 crystal			
Shoulder (from Li_2O 48.5 mol % melt)	601 ± 1	5.1543 ± 0.0002	13.7808 ± 0.0007
Stoichiometric LiTaO_3 crystal			
Shoulder (from Li_2O 58 mol % melt)	675 ± 1	5.1516 ± 0.0002	13.7744 ± 0.0007
Shoulder (from Li_2O 59 mol % melt)	685 ± 1	5.1512 ± 0.0002	13.7736 ± 0.0007
Tail (from Li_2O 59 mol % melt)	684 ± 1	5.1511 ± 0.0002	13.7730 ± 0.0007
Stoichiometric LiTaO_3 powder	690 ± 1	5.1509 ± 0.0002	13.7725 ± 0.0007

*Reprinted from *J. Cryst. Growth*, 197, Y. Furukawa et al., 889, © (1999), with permission from Elsevier Science.

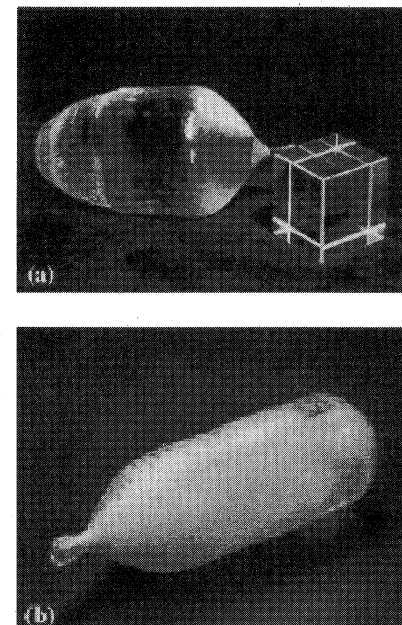


Fig. 4. (a) As-grown 50 mm diameter stoichiometric LiTaO_3 crystals grown along the y-axis, and a polished and poled cube from the boule. (b) As-grown stoichiometric LiNbO_3 crystals along the z-axis.

der the same atmosphere. In the case of LiNbO_3 , the color centers are shown to be related to $(\text{Nb}_{\text{Li}}\text{--Nb}_{\text{Nb}})$ bipolaronic defects [19] and therefore a lack of Nb_{Li} antisite defects in stoichiometric crystals results in a lack of color. Similarly, $(\text{Ta}_{\text{Li}}\text{--Ta}_{\text{Ta}})$ bipolaronic defects may be the responsible for color centers in LiTaO_3 . Etching experiments using a mixed solution of HF and HNO_3 show that the as-grown crystal from the Li-rich melt have a ferroelectric multi-domain structure. The as-grown crystals are first annealed at 1000°C for 24 h in an air atmosphere to relieve the strain, and then are poled above the Curie temperature by the conventional field cooling method [14]. In this process, the crystal is cooled under an external electric field in the z-direction through the Curie temperature. The crystal composition is estimated from the lattice parameters and Curie temperature (T_c) of the samples taken from sections at the shoulder (about 5 mm from the seed) and at the tail. The results are summarized in Table I. The crystal grown from the Li-rich melt (Li_2O : 59 mol %) exhibits a Curie tempera-

ture of 685°C , while that of the congruent melt composition (Li_2O 48.5 mol %) crystals was 601°C . For comparison, the powder sintered from a stoichiometric mixture of Li_2CO_3 and Ta_2O_5 shows a Curie temperature of 690°C . Some impurity concentrations in the stoichiometric LiTaO_3 crystals were analyzed by the ICP-MS (Inductive Coupled Plasma with Mass Spectrometry) method. The iron concentration was 0.9 wt ppm as Fe. Copper and chromium were contained less than 0.1 and 0.2 wt ppm, respectively.

Figure 5(a) is a comparison of the transmittance between the stoichiometric and the congruent crystal, where the latter was grown by the conventional Czochralski method. The absorption edges of the stoichiometric and congruent LiTaO_3 are 260 and 275 nm, respectively. The optical homogeneity of grown crystals were characterized by the Cross-Nikol method and the Mach-Zender interferometer. Stoichiometric LiTaO_3 crystals show no growth striations and have small refractive index changes less than 1×10^{-5} throughout the 1-cm^3 cubic sample.

2.5. Characterization of Grown Crystals of Stoichiometric LiNbO_3

The grown crystals are annealed under flowing oxygen for a day at 1000°C to remove any residual strain or oxygen vacancy. An as-grown, z-axis boule, 45-mm diameter and 120-mm length is shown in Figure 4(b). Table II shows the lattice parameters and the Curie temperature (T_c) [13, 20] of the crystal taken from sections at the shoulder (about 1 cm from the seed) and at the tail. Within experimental error, the chemical composition through the crystal was uniform and close to the stoichiometric composition.

The ferroelectric domain structure perpendicular to the growth axis is observed using acid etch. The largest part of the crystal was found to be single domain, where the negative end of the dipole faced the melt. At the periphery (about 1–2 mm from the rim) were domains of the opposite polarity observed. The transmittance of both stoichiometric and congruent crystals is shown in Figure 5(b). The absorption edge in stoichiometric LN is shifted to lower wavelengths by $\sim 20 \text{ nm}$ similar to the LiTaO_3 crystals.

2.6. Discussions

The DCCZ method coupled with a smooth and continuous powder supply system have some advantages in the growth of various materials. First, the surface level of the melt is always constant. This suggests that the crystals can be grown under the condition,

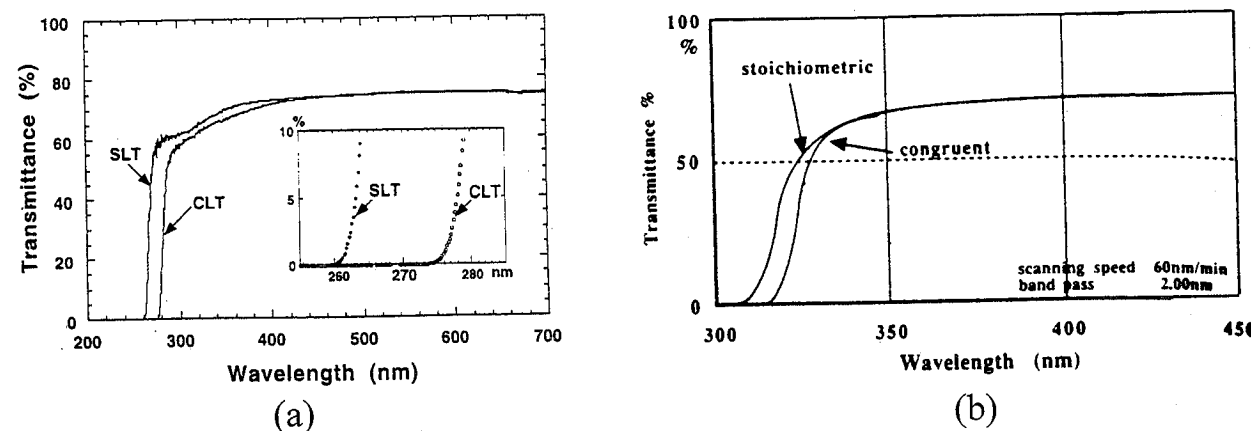


Fig. 5. (a) Transmittance spectrum of congruent and stoichiometric LiTaO₃ crystals. Reprinted from *J. Cryst. Growth*, 116, K. Kitamura et al., 327, © (1992), with permission from Elsevier Science. (b) Transmittance spectrum of congruent and stoichiometric LiNbO₃ crystals.

Table II. Curie Temperature and Lattice Parameters of the Grown Stoichiometric LiNbO₃ Crystal*

Sample	Curie temperature T_c (°C)	Lattice parameters (Å)	
		a_o	c_o
Stoichiometric LiNbO ₃ crystal [13]			
Shoulder	1190±3	5.1487±0.0001	13.8583±0.0005
End	1187±3	5.1486±0.0001	13.8603±0.0005
Stoichiometric LiNbO ₃	1198 [33]	5.1474	13.8561 [20]
Congruent LiNbO ₃	1138 [25]	5.1505	13.8650 [20]

*Reprinted from *J. Cryst. Growth*, 116, K. Kitamura et al., 327, © (1992), with permission from Elsevier Science.

diminishing the effect of changes in melt convection caused by a decrease in the depth of the melt during conventional Czochralski growth. Homogeneous doping throughout the crystal and stoichiometry control can be realized. Moreover, large crystals can be grown from the shallow double crucible.

(i) *Thermal condition in the growth system*: A suitable thermal environment must be established to exclude the spiral growth or cracks in large diameter LiTaO₃ crystals [18, 21]. Furukawa et al. varied the thermal gradients by changing the crucible-RF coil position in LiTaO₃ growth. The vertical and radial temperature gradient just below the liquid surface, $(dT/dZ)_{z=-5-0\text{ mm}}$ and $(dT/dr)_{r=2\text{ mm}}$ were varied from 30 to 10°C cm⁻¹ and from 3 to 1°C cm⁻¹, respectively. The vertical gradient just above the liquid surface, $(dT/dz)_{z=0-5\text{ mm}}$, was varied from 150 to 20°C cm⁻¹. Both vertical and radial temperature gradients in their experiments are smaller than those in the conventional CZ system reported by Brandle and Miller [18] and Matsumura [21]; consequently, crack-free stoichiometric LiTaO₃ crystals were successfully grown. Moreover, spiral growth, often observed near the end of conventional CZ growth, was not observed in DCCZ growth even when crystals were grown under the lowest temperature gradient. Other noticeable characteristics in the double crucible system using a radio frequency (rf) heater is that the radial temperature gradient is very gentle in contrast to the vertical temperature gradient. This is because the rf frequency power mainly coupled to the outer crucible and not to the inner crucible, and inner melt was heated by the heat transfer through the outer melt.

Therefore the radial temperature gradient and thermal fluctuation of the melt are small in this system. Thus, the flow pattern on the liquid surface, which was strongly observed in the conventional Czochralski growth [22] in LiNbO₃ and LiTaO₃ becomes weak.

Another important advantage is that the DCCZ method with an rf heating system can prove a longer working life time of the crucible without deformation after many growth runs. During the cooling process after the growth, the outer melt solidifies and swells surrounding the inner crucible since it is the coldest part, consequently, the wall of outer crucible is free from stress and is not damaged. Therefore the DCCZ might be applied to the conventional CZ growth to reduce the production cost dominated by the recasting of the Ir crucible.

(ii) *Stoichiometry control*: Assuming a linear relationship between the Curie temperature and crystal composition [23-25] the Li/(Ta+Li) atomic ratio in the grown crystal from Li₂O excess melt (58-59 mol %) was estimated in a range of 0.4977 to 0.4992. The LiNbO₃ crystals grown by Kitamura et al. [13] showed a Li/(Li+Nb) ~ 0.499. The maximum compositional variations throughout the stoichiometric crystals were also estimated to be in the range of 0.002. This compositional variation might be caused by an imperfect mixing of raw materials and Li₂O evaporation during growth. Although the Li/(Ta, Nb+Li) atomic ratio of grown crystal is mainly varied by the manner of initial charging, the exact melt composition which produces exact stoichiometric solid composition has not been determined so far. To control the chemical composition of grown crystal more precisely, further

study is necessary concerning optimum initial melt composition. To grow homogeneous crystals by the DCCZ method, a smooth and continuous powder supply is necessary. The precise control of feeding was easily accomplished for higher density LiTaO₃ powder (7.5 g cm⁻³) than for LiNbO₃ (4.5 g cm⁻³). Using the coarse grained powder the deviation of the actual amount of LiTaO₃ powder supplied to the grown crystal weight was nearly zero, for example, deviation was 0.10 g after the growth of 650 g in crystal weight.

(iii) *Issues in the growth from off-congruent melt*: It was reported that the mechanical twinning is the most severe problem encountered in the stoichiometric LiNbO₃ grown from a melt of excess Li₂O or a melt of K₂O-doped [26]. This mechanical twin is formed just after the crystal growth: it is nucleated on the bottom surface of the grown crystal. The main cause of twinning is the stress which can be provided during the growth and cooling process of the crystal, this stress is more severe in the stoichiometric crystal grown from off-congruent melt than in the crystal grown from congruent melt. However, mechanical twinning is not observed in stoichiometric LiTaO₃ crystals even attached with some Li₂O excess flux. The main reason is probably that the as-grown LiTaO₃ which has a multi-domain structure is much stronger against the stress introduced at the detaching process than the LiNbO₃ crystal which has a completely single domain structure in the as-grown stage. Therefore, the careful tailing process which can reduce the stress at the bottom surface of the grown crystal from the off-congruent melt is not necessary in the growth of stoichiometric LiTaO₃.

In many cases, the optical properties of complex oxide compounds depend on their stoichiometry. As shown in Figure 5, the transmittance of stoichiometric crystals near the absorption edge is superior to that of congruent crystals, illustrating the importance of lithium stoichiometry control. Stoichiometric LiTaO₃ show more than 1 order of magnitude lower coercive field for ferroelectric domain switching as discussed in Section 4, which is desirable for the fabrication of integrated optical devices with domain structure control. Given a strong sensitivity of physical properties of the crystals to lithium stoichiometry, it becomes imperative that the crystal composition and local inhomogeneities be characterized sensitively for any real application of these materials. In the following section, we describe in detail, the technique of Maker fringe analysis to sensitively probe local changes in optical properties of these crystals, from which one can deduce the changes in the composition, local strains, and electric fields within the crystal.

3. CRYSTAL UNIFORMITY STUDIES BY MAKER FRINGE ANALYSIS

3.1. Introduction

Issues of manufacturing yield and reliability for a wide range of integrated optical waveguide devices based on congruently grown LiNbO₃ have become a matter of concern. This trend was propelled by the increasing demands on this material for uses in optical fiber gyro systems, the wide range of applications enabled by periodically poled lithium niobate (PPLN) technology, and the upsurge in demand for high-speed LiNbO₃ modulators for telecommunications [27-29]. In spite of the enormous success and popularity of this material, problems with crystal growth still remain and it is not uncommon to read reports of inconsistent device yields

across batches of wafers even after meticulous attention is paid to processing details [30-32]. Waveguides in this material are typically fabricated by the diffusion of Ti stripes and methods of ion exchange [33, 34]. Some of the problems with inconsistent results undoubtedly arise from errors in processing while others may be traced to nonuniformity in the substrate LiNbO₃ wafers.

Compositional variations are closely linked to variations in the diffusivity of Ti which is one of the most common waveguide forming dopants used in this material. It is reported that variations in the Li₂O composition of 0.02 mol % produce changes of 2% in the diffusivity of Ti [35]. Such a variation in the waveguide dopant profile would certainly impact the reproducibility and characteristics of, for example, waveguide directional coupler structures [36]. In the discussion that follows it is shown that a compositional variation by this degree is not unusual over a batch of wafers cut from a single boule. It is therefore beneficial to develop new nondestructive metrology tools that augment traditional methods such as interferometry, optical inspection, and X-ray analysis, to compare the similarity and quality of wafers before they enter the processing line.

Second-harmonic generation (SHG) offers an attractive metrology approach to examine LiNbO₃ wafer uniformity. For example, the *o*-polarized pump, *e*-polarized SHG orientation can be extremely sensitive to variations in birefringence. Using the common pump wavelength of 1064 nm provided by a Nd:YAG laser, birefringence variations as low as 5×10^{-6} are readily resolved in standard commercially produced congruent *x*-cut wafers. The conventional designations of crystal optics are used in this discussion where the electric-field vector of an *e*-polarized ray may have components both parallel and perpendicular to the optic axis (*c*-axis) of the crystal while the electric field vector of an *o*-polarized ray is strictly perpendicular to the optic axis. The index of refraction for an *e*-polarized ray is n_e for the special case of propagation perpendicular to the optic axis. An *o*-polarized ray will always experience a refractive index of n_o . The index of refraction for a general *e*-polarized ray that propagates with components that are both parallel and perpendicular to the optic axis is a function of n_o , n_e , and the angle between the ray propagation direction and the optic axis. This is described further in Section 3.3 and in standard textbooks [37].

Composition variations in LiNbO₃ are directly related to variations in birefringence. The Li/Nb mole ratio may vary by more than ±0.02% during the growth of a LiNbO₃ boule and between separately grown boules [38]. A variation in composition by this amount will result in a variation in the extraordinary index n_e of approximately 2×10^{-4} at 632 nm with the ordinary index n_o remaining essentially constant [39]. Additionally, SHG may be used to infer and to approximate photoelastic strain in the material. Consider the pump conditions described for use in the examination of an *x*-cut wafer. The *e*-polarized SHG power is roughly 10^3 – 10^4 times larger than the *o*-polarized SHG that is simultaneously produced. Careful examination of the weaker *o*-polarized data reveals a residual signature arising from the dominant *e*-polarized SHG. This effect is commensurate with an aggregate photoelastic strain of roughly 10^{-4} that effectively mixes the *e*- and *o*-polarized SHG fields. The work presented in this review considers SHG in the form of Maker fringes which are defined as oscillations of the SHG intensity transmitted through the plate as a function of the pump beam angle of incidence [40]. Least-squares solution routines were used to fit the experimental data with analytical models describing the Maker fringes for various pump-SHG polariza-

tion conditions. This permitted measurements of n_e , approximate strain, and sample thickness at the location on the wafer where the fringes were recorded. Here again, n_e may be directly related to composition. Performing such scans on a gridlike fashion over the entire wafer allowed maps of these quantities to be produced. Performing such mapping on wafers cut sequentially from an entire boule allowed trends in crystal growth to be revealed. Sanford and Aust published preliminary work that described the use of Maker fringe analysis to produce maps of birefringence and strain in LiNbO₃ [41]. Earlier work that originally suggested the use of Maker fringes for the characterization of LiNbO₃ wafers and boules was given by Lunt et al. [42, 43].

3.2. Experimental Apparatus and Data Collection

The experimental conditions used to produce and to record Maker fringes are now described. Consider the situation shown in Figure 6(a) that illustrates the pump and SHG polarization conditions considered for x - and z -cut plates. An o -polarized pump field indicated by the associated wave vector γ^o is incident on the x -cut wafer at an angle θ_i . An e -polarized pump field incident on a z -cut plate is indicated by the wave vector γ^e . The pump field in the media drives a nonlinear source polarization (whose wave vector is indicated by k^p) that produces an e -polarized SHG field (whose wave vector is indicated by k^s) and an o -polarized SHG field (whose wave vector is indicated by k^s). Throughout this discussion a convention is used whereby quantities superscripted by p and s refer to pump and SHG fields, respectively, *not* states of polarization. The x, y, z coordinate system conforms to the crystal axes. Figure 6(a) represents only a subset of the four pump-SHG cases possible, namely, e - and o -polarized pumping leading to both e - and o -polarized SHG. However, for the purposes of the present discussion, it is sufficient to consider only the cases of o -polarized pumping leading to e - and o -polarized SHG for an x -cut plate, and e -polarized pumping giving rise to e -polarized SHG for a z -cut plate.

Figure 6(b) illustrates a schematic of the apparatus used to generate and to collect e -polarized and o -polarized Maker fringe data. The pump beam was produced by a simultaneously mode locked (82-MHz), Q -switched (800-Hz) Nd:YAG laser. The average pump power incident on a sample was typically attenuated to 25 mW and the pump was generally focused to a $1/e$ spot diameter of $\sim 70 \mu\text{m}$. Polarizers and waveplates were used to set the polarization state of the pump as needed. Polarizing beam splitters and harmonic separators selected and filtered the e - and o -polarized SHG outputs that were detected with separate photomultiplier tubes, current sensitive preamplifiers, and boxcar averagers. The analog SHG signals were collected and processed by a computer that also controlled the automated stage assembly as illustrated in Figure 6(b).

3.3. Modeling of Maker Fringes for x - and z -Cut LiNbO₃ Wafers

3.3.1. o -Polarized Pumping of an x -Cut Wafer

A brief description of the theoretical development used to model Maker fringes generated by x - and z -cut LiNbO₃ wafers is now presented. Our analysis is derived directly from Maxwell's equations, employs the full birefringence of the material, and also takes into account multiple Fabry-Perot resonances of the pump and

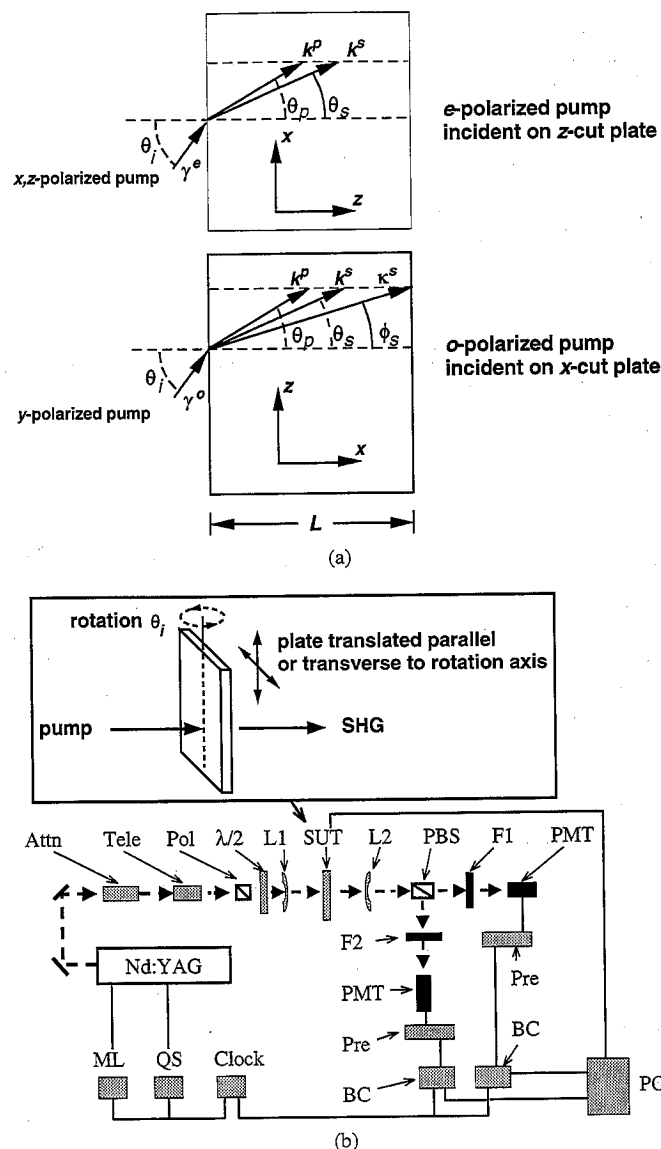


Fig. 6. (a) A schematic showing the pump and SHG wave vectors for the cases of an o -polarized pump producing o - and e -polarized SHG in an x -cut plate and an e -polarized pump producing e -polarized SHG in a z -cut plate. In both orientations Maker fringes are produced by rotating the plate about the y -axis. For the x -cut plate the o -polarized pump field incident at θ_i is indicated by wave vector γ^o , the resulting nonlinear source polarization propagating at an angle θ_p is indicated by wave vector k^p , the o -polarized SHG propagating at an angle θ_s is indicated by wave vector k^s , and the e -polarized SHG propagating at an angle θ_s is indicated by wave vector k^s . The situation for the z -cut plate is similar, however, it is understood here that all wave vectors represent e -polarized fields. (b) A schematic showing the automated rotation-translation system used to position and to rotate the LiNbO₃ wafers for the generation and collection of Maker fringes. The input pump beam and the wafer rotation axis y_L are fixed. The sample is translated parallel or transverse to y_L to define the grid over which Maker fringe scans are collected. The elements labeled in the block diagram of the apparatus are: Optical attenuator (Attn), beam-expanding telescope (tele), polarizer (Pol), half-wave plate ($\lambda/2$), pump focusing lens (L1), sample under test attached to automated rotation-translation stage assembly (SUT), SHG collimating lens (L2), polarizing beam splitter (PBS), harmonic separator and pump filters (F1, F2), photomultiplier tube (PMT), current sensitive pre-amplifier (Pre), boxcar averager (BC), control computer (PC), crystal quartz oscillator (Clock), Q -switch driver (QS), mode lock driver (ML).

SHG. Accordingly, the full development is somewhat tedious and an unnecessary complication for the present discussion. Interested readers will find a detailed theoretical description of Maker fringes for x -cut wafers given by Sanford and Aust [44]. A complete description of Maker fringes for z -cut wafers, which considers all four e - and o -polarized pump and SHG conditions, was given by Aust [45]. Additionally, a comprehensive study of Maker fringe analysis applied to LiNbO₃ and a number of other materials was given by Shoji et al. [46].

Following Shen, the pump, SHG, and nonlinear source polarization fields are all described by complex quantities [47]. The y -polarized pump field $E_y^{p,T_1} = \hat{y}E_y^{p,T_1}$ for the case of a single pass of the pump through an x -cut LiNbO₃ plate as illustrated in Figure 6(a) is defined by

$$E_y^{p,T_1} = \hat{y}TE_y^{p,i} \exp[i(\gamma_x^p x + \gamma_z^p z - \omega_p t)] \quad (1)$$

Here $\gamma_x^p = (2\pi/\lambda_p)n_o^p \cos \theta_p$, $\gamma_z^p = (2\pi/\lambda_p)n_o^p \sin \theta_p$, T is the Fresnel transmission coefficient of the pump field at the air-LiNbO₃ boundary, ω_p is the angular frequency of the pump field, n_o^p is the ordinary index of refraction at the pump wavelength, and λ_p is the vacuum wavelength of the pump field. The superscript T_1 refers to the entrance face of the sample corresponding to $x = 0$. Throughout this discussion boldface type is reserved to describe vector quantities. Tensors are distinguished by a tilde (\sim) over the symbol. The nonlinear source polarization \mathbf{P} is most conveniently derived by using the simplified matrix form of the third-rank tensor $\tilde{\chi}$ that describes the second-order dielectric susceptibility for LiNbO₃ (class 3m). The components P_x, P_y, P_z of \mathbf{P} are given by

$$\begin{bmatrix} P_x \\ P_y \\ P_z \end{bmatrix} = \epsilon_o \begin{bmatrix} 0 & 0 & 0 & 0 & \chi_{15} & \chi_{16} \\ \chi_{21} & \chi_{22} & 0 & \chi_{24} & 0 & 0 \\ \chi_{31} & \chi_{32} & \chi_{33} & 0 & 0 & 0 \end{bmatrix} \begin{bmatrix} (E_x^{p,T_1})^2 \\ (E_y^{p,T_1})^2 \\ (E_z^{p,T_1})^2 \\ 2E_x^{p,T_1}E_y^{p,T_1} \\ 2E_x^{p,T_1}E_z^{p,T_1} \\ 2E_y^{p,T_1}E_z^{p,T_1} \end{bmatrix} \quad (2)$$

All the nonzero elements χ_{ij} are expressed in picometers per volt. Additionally, in the usual convention, $\chi_{21} = -\chi_{22}$, $\chi_{31} = \chi_{32}$, $\chi_{15} = \chi_{24}$, and $\chi_{16} = \chi_{21}$ [37]. Further simplification occurs in the absence of dispersion of the electronic contribution to the nonlinear polarizability giving $\chi_{31} = \chi_{15}$ as described by Kleinman [48]. The pump field produces a nonlinear source polarization $\mathbf{P} = \hat{y}P_y + \hat{z}P_z$ in the media where $\mathbf{P} = \epsilon_o(\hat{y}\chi_{22} + \hat{z}\chi_{31})(E_y^{p,T_1})^2$ or

$$\mathbf{P} = \epsilon_o(\hat{y}\chi_{22} + \hat{z}\chi_{31})(TE_y^{p,i})^2 \exp[i(k_x^p x + k_z^p z - \omega t)] \quad (3)$$

where $2\gamma_x^p = k_x^p$ and $2\gamma_z^p = k_z^p$. Thus, the nonlinear coefficients χ_{22} and χ_{31} enable the o -polarized pump to simultaneously produce o - and e -polarized SHG.

Inclusion of both the linear and the nonlinear source polarizations into Maxwell's equations allows the derivation of a set of wave equations that describe the complex second-harmonic fields \mathbf{E} and \mathbf{H} where

$$\nabla \times \mathbf{H} = \epsilon_o \tilde{\epsilon} \cdot \frac{\partial \mathbf{E}}{\partial t} + \frac{\partial \mathbf{P}}{\partial t} \quad (4a)$$

$$\nabla \times \mathbf{E} = -\mu_o \frac{\partial \mathbf{H}}{\partial t} \quad (4b)$$

The dielectric tensor is diagonal in the system of coordinates in which the Cartesian axes conform to the principal axes of the crystal where it is understood that $\epsilon_{11} = \epsilon_{22} = n_o^2$, $\epsilon_{33} = n_e^2$, and that these indices are evaluated at the second-harmonic wavelength λ . Equations (4a) and (4b) lead directly to a wave equation for the y -polarized component of the SHG field E_y ,

$$\partial_{xx}^2 E_y + \partial_{zz}^2 E_y + k^2 n_o^2 E_y = -\frac{k^2}{\epsilon_o} P_y \quad (5)$$

with $k = 2\pi/\lambda$ and $P_y = \epsilon_o \chi_{22} (E_y^{p,T_1})^2$. Wave equations for the e -polarized SHG field components may be derived from Eqs. (4a) and (4b) with the added constraint that $\nabla \cdot \mathbf{D} = 0$ where the electric displacement $\mathbf{D} = \epsilon_o \tilde{\epsilon} \cdot \mathbf{E} + \mathbf{P}$. These are

$$n_o^2 \partial_{xx}^2 E_x + n_e^2 \partial_{zz}^2 E_x + k^2 (n_o n_e)^2 E_x = -\frac{1}{\epsilon_o} \partial_{xz}^2 P_z \quad (6a)$$

and

$$n_o^2 \partial_{xx}^2 E_z + n_e^2 \partial_{zz}^2 E_z + k^2 (n_o n_e)^2 E_z = -\frac{1}{\epsilon_o} (\partial_{zz}^2 P_z + k^2 n_o^2 P_z) \quad (6b)$$

where $P_z = \epsilon_o \chi_{31} (E_y^{p,T_1})^2$. The general solutions for the SHG field components are

$$E_x = \{E_x^o \exp[i(k_x^s x + k_z^s z)] + A_x \exp[i(k_x^p x + k_z^p z)]\} \times \exp(-i\omega t) \quad (7a)$$

$$E_y = \{E_y^o \exp[i(k_x^s x + k_z^s z)] + A_y \exp[i(k_x^p x + k_z^p z)]\} \times \exp(-i\omega t) \quad (7b)$$

and

$$E_z = \{E_z^o \exp[i(k_x^s x + k_z^s z)] + A_z \exp[i(k_x^p x + k_z^p z)]\} \times \exp(-i\omega t) \quad (7c)$$

With the definition of θ_s given in Figure 6, the wave vector components for the homogeneous portions of Eqs. (7a) and (7c) describing the e -polarized SHG, and the dependence of the index of refraction on θ_s , are consistent with the standard results from crystal optics where

$$n(\theta_s) = \frac{n_e n_o}{\sqrt{n_e^2 \sin^2 \theta_s + n_o^2 \cos^2 \theta_s}} \quad k_x^s = kn(\theta_s) \cos \theta_s$$

$$\text{and } k_z^s = kn(\theta_s) \sin \theta_s$$

The wave vector components for the homogeneous portion of the o -polarized SHG field described by Eq. (7b) are given by $k_x^s = kn_o \cos \phi_s$ and $k_z^s = kn_o \sin \phi_s$.

The solutions for the homogeneous SHG field amplitudes E_x^o , E_y^o , E_z^o , and the amplitudes of SHG fields radiated into the air at the air-LiNbO₃ interfaces at $x = 0, L$ are found by equating the amplitudes of the tangential components of \mathbf{E} and \mathbf{H} at these interfaces. In many instances, an adequate description of Maker fringes may be obtained by considering only a single pass or a finite number of passes of the pump and SHG fields through the media in accordance to the development leading to Eqs. (7). In the more general case, however, the sample must be treated as a Fabry-Perot resonator. The resonance analysis is complicated by the fact that the multiple internal reflections of the pump and

SHG fields overlap and interfere to a varying extent defined by θ_i , the pump beam diameter, and the sample thickness L . Numerical examples comparing the single-pass analysis with an approximate double-pass ray analysis were previously given by Sanford and Aust [44]. However, for the results presented here involving multiple passes of the pump and SHG, the plate is treated as a Fabry-Perot resonator with no approximations made for a fixed number of passes of the pump and SHG. The details of this approach are given by Aust [45]. Modeling the transition from the fully resonant regime near $\theta_i = 0$ to the nonresonant regime at larger values of $|\theta_i|$, where multiple passes of the pump and SHG cease to interfere, was performed with a heuristic approximation that took into consideration the Gaussian beam diameters of the pump and SHG and the thickness of the plate. To avoid the added complexity that the pump-SHG resonances introduce, some authors have used antireflection coated samples to force the validity of a single-pass approximation for the measurements of χ_{ij} coefficients [46]. For the most part such a simplifying expedient is fine, however, as described in Section 3.5, there may be some risk of incorrectly fitting the envelope of the fringes and computing an erroneous value of χ_{31} for the o -pumped e -SHG configuration in either x - or y -cut plates.

We define the x , y , and z SHG field amplitudes leaving the plate at $x = L$ as $E_x^{(T_2)o}$, $E_y^{(T_2)o}$, and $E_z^{(T_2)o}$, respectively, with the associated field components given by

$$E_x^{T_2} = \{E_x^{(T_2)o} \exp[i(k_x(x-L) + k_z z)]\} \exp(-i\omega t) \quad (8a)$$

$$E_y^{T_2} = \{E_y^{(T_2)o} \exp[i(k_x(x-L) + k_z z)]\} \exp(-i\omega t) \quad (8b)$$

and

$$E_z^{T_2} = \{E_z^{(T_2)o} \exp[i(k_x(x-L) + k_z z)]\} \exp(-i\omega t) \quad (8c)$$

where the superscript T_2 refers to the exit plane at $x = L$. The normalized e - and o -polarized SHG powers leaving the plate at $x = L$ are defined by \bar{P}_e and \bar{P}_o where

$$\bar{P}_e = \frac{(|E_x^{(T_2)o}|^2 + |E_z^{(T_2)o}|^2)}{[\chi_{31}(E_y^{P,i})^2]^2} \quad (9a)$$

and

$$\bar{P}_o = \frac{|E_y^{(T_2)o}|^2}{[\chi_{22}(E_y^{P,i})^2]^2} \quad (9b)$$

3.3.2. e -Polarized Pumping of a z -Cut Wafer

The approach to derive a set of wave equations describing SHG produced by z -cut plates is quite similar as that used for the x -cut plates. Looking back at Figure 6(a), a z -cut plate may be modeled by interchanging x with z and y with $-y$ and proceeding along the same mathematical path as outlined for the treatment of x -cut plates. One notes immediately that for z -cut plates rotated about y the description of the o -pumped o -SHG case is exactly the same as for x -cut plates rotated about y . Also, the o -pumped e -SHG case is quite similar to that given for the x -cut plates. A comprehensive description of all four cases involving o - and e -polarized

pumping producing o - and e -polarized SHG in z -cut LiNbO_3 was given by Aust [45]. It is instructive to close our theoretical survey by outlining the solution for the case of e -polarized pumping producing e -polarized SHG. The e -polarized pump field $E_{x,z}^{P,T_1}$ within the z -cut plate is described by

$$E_{x,z}^{P,T_1} = \hat{x}E_x^{(P,T_1)o} \exp[i(\gamma_x^{Pe}x + \gamma_z^{Pe}z - \omega_p t)] + \hat{z}E_z^{(P,T_1)o} \exp[i(\gamma_x^{Pe}x + \gamma_z^{Pe}z - \omega_p t)] \quad (10)$$

Since the pump field is now an e -polarized wave, the components of the wave vectors in the media are further distinguished by the superscript p_e to avoid confusion with the previous case involving o -polarized pumping of an x -cut plate. The wave vector components γ_x^{Pe} and γ_z^{Pe} are defined by

$$\gamma_x^{Pe} = (2\pi/\lambda_p)n(\theta_p)\sin\theta_p \text{ and } \gamma_z^{Pe} = (2\pi/\lambda_p)n(\theta_p)\cos\theta_p$$

where now the index of refraction of the pump is dependent upon the angle θ_p as given by

$$n(\theta_p) = \frac{n_e^p n_o^p}{\sqrt{(n_e^p)^2 \cos^2 \theta_p + (n_o^p)^2 \sin^2 \theta_p}}$$

Here, n_e^p and n_o^p are the extraordinary and the ordinary indices of refraction at the pump wavelength. The pump field drives the nonlinear source polarization $\mathbf{P} = \hat{x}P_x + \hat{z}P_z$ where now

$$P_x = \hat{x}2\epsilon_0\chi_{31}E_x^{(P,T_1)o}E_z^{(P,T_1)o} \exp[i(k_x^{Pe}x + k_z^{Pe}z - \omega t)] \quad (11a)$$

and

$$P_z = \hat{z}\epsilon_0[\chi_{31}(E_x^{(P,T_1)o})^2 + \chi_{33}(E_z^{(P,T_1)o})^2] \times \exp[i(k_x^{Pe}x + k_z^{Pe}z - \omega t)] \quad (11b)$$

where $k_x^{Pe} = 2\gamma_x^{Pe}$ and $k_z^{Pe} = 2\gamma_z^{Pe}$. The term P_z appearing in Eq. (11b) should not be confused with the similar factor described earlier for o -polarized pumping of an x -cut plate. Finally, wave equations for the e -polarized SHG field components E_x and E_z may now be derived. These are

$$n_e^2 \partial_{zz}^2 E_x + n_o^2 \partial_{xx}^2 E_x + (n_e n_o)^2 k^2 E_x = \frac{-1}{\epsilon_0} [(n_e k)^2 P_x + \partial_{xx}^2 P_x + \partial_{xz}^2 P_z] \quad (12a)$$

and

$$n_o^2 \partial_{xx}^2 E_z + n_e^2 \partial_{zz}^2 E_z + (n_e n_o)^2 k^2 E_z = \frac{-1}{\epsilon_0} [(n_o k)^2 P_z + \partial_{zz}^2 P_z + \partial_{xz}^2 P_x] \quad (12b)$$

Once again, these fields should not be confused with the e -polarized SHG field components described earlier for the x -cut case. The resulting expression for the normalized SHG power emerging from the z -cut plate at $z = L$ is defined as \bar{P}_e^z . This quantity is similar to the normalized e -polarized output power given for the x -cut example. However, \bar{P}_e^z does not conveniently factor in terms a single χ_{ij} coefficient, thus for brevity, it is not reduced further.

3.4. o -Polarized Maker Fringes and Thickness Maps of x -Cut Wafers

As discussed earlier, the ordinary index of refraction may be regarded as independent of compositional variations. This immediately enables the use of the o -polarized Maker fringes for measuring the sample thickness. The resulting thickness data may then be used as input in the analysis of the e -polarized data for computing birefringence and hence composition variations. Figure 7 illustrates a simulation of the sensitivity of the o -polarized Maker fringes to sample thickness when Fabry-Perot resonances of the pump and SHG are considered. In this example the pump beam diameter was approximately $70 \mu\text{m}$ and the indices of refraction were computed at a temperature of at 30°C using the well-known Sellmeier equations of Edwards and Lawrence [49]. The result illustrates that a 10-nm thickness variation in a sample nominally 1 mm thick may be resolved by the Maker fringe data for θ_i within $\pm 5^\circ$. The walk-off of the multiple internal reflections of the pump and SHG as θ_i increases is included in the simulation and is illustrated by the damping of the high-frequency fringes when $|\theta_i|$ exceeded $\sim 10^\circ$. Of course, for a thinner sample with the same pump diameter, or a larger pump diameter with the same sample thickness, the high-frequency fringes would persist for larger values of $|\theta_i|$. Figure 7 also illustrates the result of the single-pass approximation that illustrates that the thickness resolution degrades to 100 nm when the resonance of the pump and SHG is neglected.

The precision of the thickness measurement is limited by the inherent uncertainty in the Sellmeier results for n_o^p and n_o and by approximate modulo 2π artifacts with respect to thickness that exist within the simulations of the Maker fringes. With regard to the latter, in the single-pass approximation the o -polarized SHG power \bar{P}_o is described by a term proportional to $\cos[(k_x^p - k_x^s)L]$ where L is the thickness of the sample. This suggests that computing the absolute sample thickness from Maker fringe data

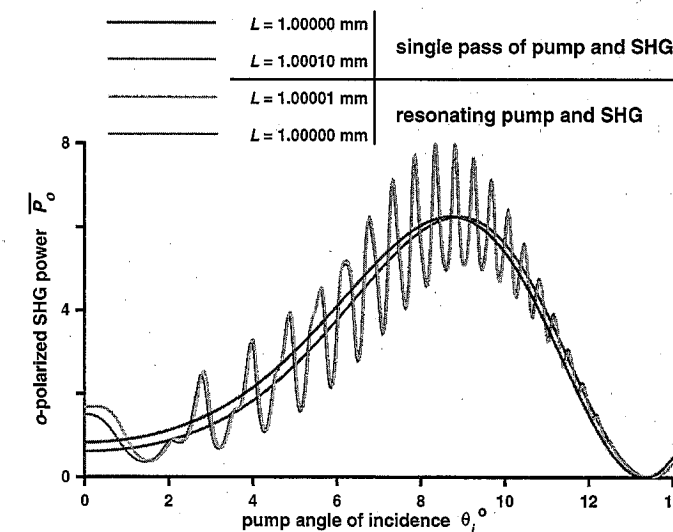


Fig. 7. A simulation illustrating the sensitivity of the o -polarized Maker fringes to small changes in thickness L for an x -cut plate. When multiple pump-SHG passes are neglected, the thickness resolution is approximately ± 100 nm. When the multiple passes are included, the thickness resolution is approximately ± 10 nm. The walk-off of the multiple reflections is illustrated in the fading amplitude of the high-frequency Maker fringes with increasing θ_i .

may be ambiguous by integer multiples of twice the coherence length $\pm m 2l_c^{(o,o)}$ (m = integer) for the o -pump o -SHG interaction where the coherence length $l_c^{(o,o)} = \lambda/2|n_o^p - n_o|$ giving $2l_c^{(o,o)} \sim 5.84 \mu\text{m}$. An illustration of this effect appears in Figure 8 for $m = 0, 1, 2$. The simulations illustrated in Figures 7 and 8 indicate that an unambiguous thickness map for a LiNbO_3 plate of nominal thickness $L = 1$ mm can be derived from the o -polarized SHG fringe data provided that $|\theta_i|$ extends to a range between 30° – 90° . Accordingly, the following procedure was employed in mapping sample thickness. In all the Maker fringe scans of a series, $|\theta_i|$ was typically 50° or larger. A "coarse" least-square thickness search algorithm was used that calculated a bound on L to within $\pm 2l_c^{(o,o)}$. Using this as an initial thickness value in a second higher resolution search algorithm operating on the same data set, the thickness was computed to within $\sim \pm 100$ nm using only the single-pass approximation and optionally omitting the high-frequency SHG fringe data near $\theta_i = 0$. Alternatively, including the high-frequency fringes and the full Fabry-Perot resonances of the pump and SHG permitted calculation of thickness to within ± 10 nm at best. The sample was then stepped to the next scan point and the process repeated. However, if the taper of the plate between these locations was less than $\sim 5.8 \mu\text{m}$ (the value of thickness leading to a 2π modulo ambiguity) it was sufficient to use the solution for the previous scan location as the initial value in the new thickness search. There is an inherent uncertainty of roughly $\pm 2 \times 10^{-4}$ in the original refractive index data used to derive the temperature-dependent Sellmeier equations used here [50].

For a Maker fringe scan at a location on a sample with negligible taper, this inherent uncertainty in refractive index imposes an absolute uncertainty of approximately $\pm 0.2 \mu\text{m}$ on the accuracy of the resulting thickness calculation. If there is sufficient taper at the scan location, or the sample is not properly located on the rotation axis on the automated rotation-translation stage system, the pump beam may sweep through a varying sample thickness during the traversal of θ_i ; thus leading to a chirp in the SHG fringe

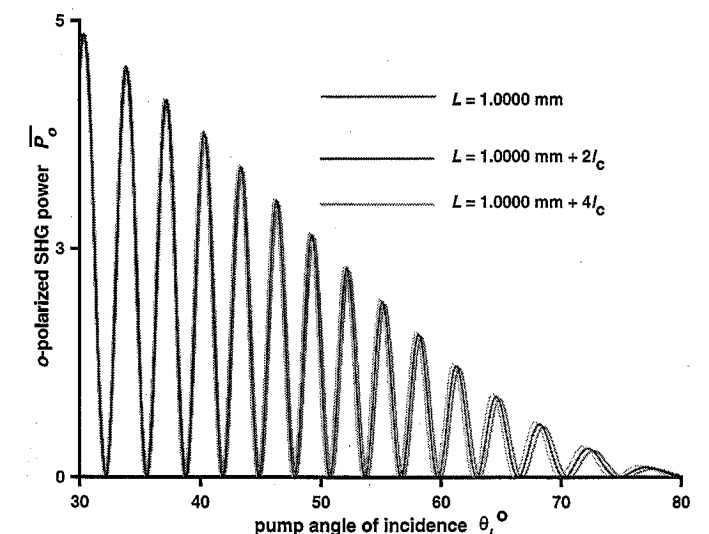


Fig. 8. The ambiguity of the o -polarized Maker fringes with respect to variations in L by multiples of twice the coherence length is reduced for (roughly) $30^\circ < |\theta_i| < 90^\circ$. Fitting fringe data that extends to this angular range allows for the unambiguous calculation of the sample thickness to within ± 100 nm for a plate nominally 1-mm thick in the single-pass regime.

frequency and an increase in overall uncertainty of the computed thickness.

Examples of fitting *o*-polarized Maker fringe data and generating full thickness maps of LiNbO₃ wafers are now discussed. In all of the work presented here for *x*-cut plates the samples were nominally 1-mm thick. All of the 76-mm diameter *x*-cut wafers examined were sequentially cut from a single boule. Figure 9(a) illustrates fitting our fully resonant simulation code to a typical data set. Figure 9(b) shows a thickness map for a 44×44-mm section computed for the central portion of a commercially produced 76-mm diameter *x*-cut LiNbO₃ wafer. In this case, Maker fringe scans were performed sequentially on a 19×19 grid with a point separation (mesh) of 2.444 mm. As illustrated in Figure 9(b) the coordinate grid is defined with ordinate z_c and abscissa y_c and is indexed from left-to-right, bottom-to-top, with point #1 located at the origin of the contour map ($z_c = 0$, $y_c = 0$) and point #361 located at the extreme upper right corner ($z_c = 19$, $y_c = 19$). For clarity, the sense of the *y*- and *z*-crystal axes are indicated on the figure and this orientation applies to all wafer maps presented.

The rate of data collection was limited by the *Q*-switching repetition rate of 800 Hz, the angular resolution of θ_i , and the extent of traversal of θ_i . Recording the high-frequency Maker fringes required setting the increment of θ_i to 0.1° and a typical scan involved sweeping θ_i through $\pm 50^\circ$. Therefore, sufficient signal averaging per increment of θ_i required approximately 4 min per scan or 24 h for a full 361-point grid. Over this period of time the ambient laboratory temperature could drift by as much as $\pm 1^\circ\text{C}$. The sample temperature T was recorded during each individual scan and the reading was stored and associated with the corresponding Maker fringe data. The temperature data permitted computation of the indices of refraction via the temperature-dependent Sellmeier equations. These index values were then used in the fitting of the model to the Maker fringe data for the computation of thickness L at each scan location. The data and fit illustrated in Figure 9(a) correspond to scan point #200 in Figure 9(b). The thickness map illustrated in Figure 9(b) was fairly typical for the 76-mm diameter wafers examined. These often showed thickness variations on the order of ± 2 – $7\ \mu\text{m}$ from margin to center. We examined 25 such wafers taken from a set that was cut in sequence from a single boule where wafer #1 was from the top of the boule and wafer #38 was from the bottom. For purposes of comparison with larger plates, the thickness map of a 100-mm diameter *x*-cut wafer is shown in Figure 9(c). This wafer was cut from a completely different boule than that represented in the 76-mm diameter series. In this case, the map is composed of a 21×21 grid with a 3-mm mesh. Referring back to Figure 9(a), note that the envelope of the SHG signal departs from the simulation and that the first fringe null does not go to zero. Both of these deviations between the data and the model are attributed in part to effects of photoelastic strain whereby the dominant *e*-polarized SHG signal corrupts the weaker *o*-polarized signal. Some of this effect could also be attributed to background leakage of the polarization optics resulting in incomplete rejection of the *e*-polarized signal in the detection channel for the *o*-polarized SHG. However, the degree of corruption of the *o*-polarized SHG data varied significantly over a single wafer and was sometimes altogether negligible. The effect also varied considerably between wafers. These issues are discussed further in Section 3.6.

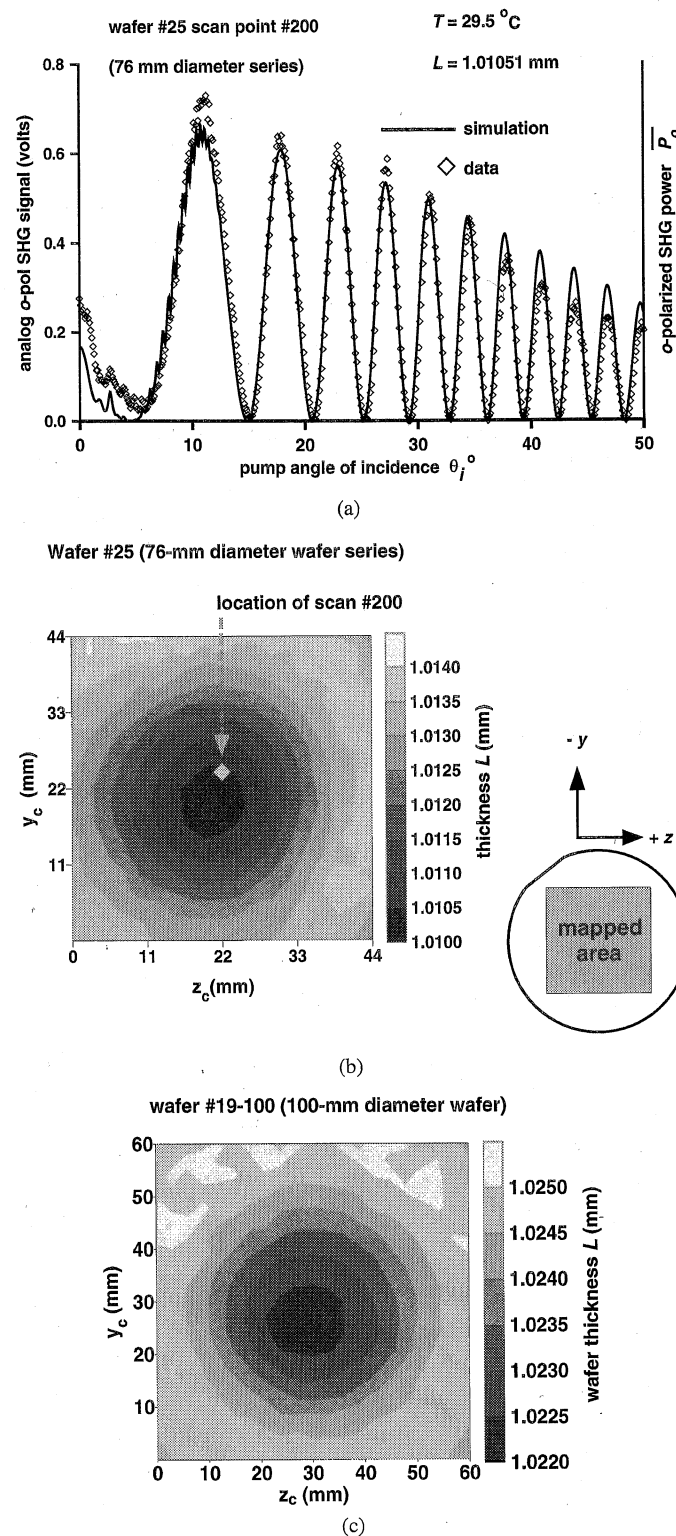


Fig. 9. (a) An example of fitting *o*-polarized Maker fringe data to compute sample thickness. The data collection temperature $T = 29.5^\circ\text{C}$ and the computed thickness for this scan, as located on the wafer in Figure 9(b), was $L = 1.01051\ \text{mm}$. (b) Thickness map for wafer #25 of the 76-mm diameter *x*-cut series. Note that z_c and y_c refer to the coordinate axes for the contour map while x , y , and z are the crystal axes of the wafer as shown. (c) Thickness map over a 60×60-mm area for a 100-mm diameter *x*-cut LiNbO₃ wafer.

3.5. *e*-Polarized Maker Fringes and Variations in Composition of LiNbO₃ Wafers

Our aim here is inferring compositional variations in LiNbO₃ wafers through the dependence of n_e on the Li₂O mole fraction. Once again, variations in the ordinary indices of refraction due to fluctuations in composition are presumed negligible. Therefore, fitting the *e*-polarized SHG fringes involves using n_e as a variable parameter so it is important to search for modulo 2π artifacts that may arise in this regard. In the single-pass approximation, the oscillation of *e*-polarized Maker fringe intensity is described by a term proportional to $\cos[(k_x^p - k_x^s)L]$. The coherence length $l_c^{(o,e)}$ for this *o*-pump *e*-SHG interaction is given by $l_c^{(o,e)} = \lambda/2|n_o^p - n_e^s|$. Evaluation of the Sellmeier equations at 30°C and $\theta_i = 0$ gives $2l_c^{(o,e)} = 230.9\ \mu\text{m}$ so there is little concern for complications of thickness-induced ambiguities in fitting the *e*-polarized Maker fringes. For $L = 1\ \text{mm}$, n_o^p held constant, and $\theta_i = 0$, from the discussion so far it seems reasonable that the variation in extraordinary index $\Delta^S n_e$ that produces an ambiguous Maker fringe simulation is $\Delta^S n_e = \pm 5.32 \times 10^{-4}$ where $n_e = n_e^S + \Delta^S n_e$ and n_e^S is the extraordinary index at 532 nm derived from the temperature-dependent Sellmeier equations. As illustrated in the simulations displayed in Figure 10(a), this conclusion is not valid for *o*-polarized pumping producing *e*-polarized SHG because a phase-matching condition nearly occurs which leads to a significant shift in the envelopes of SHG fringes between the cases $\Delta^S n_e = 0, \pm 5.32 \times 10^{-4}$. Thus, in fitting the *e*-polarized fringes, one must be careful to extend the range of θ_i enough to fit both the envelope and the frequency of the fringes. Figure 10(b) illustrates an example of fitting our simulation to *e*-polarized SHG data collected at a temperature of 29.3°C from wafer #30 of the sequentially cut 76-mm diameter set. The computed value of n_e which yielded the fit shown was $n_e = 2.23385$ which corresponded to a variation from the Sellmeier result by $\Delta^S n_e = -6.19 \times 10^{-4}$. Two nearly equivalent fits to the fringe frequency would be obtained by choosing $n_e = 2.23385 \pm 5.32 \times 10^{-4}$, however, as illustrated in Figure 5(a) the fringe envelopes would be either too low or too high, respectively. The accuracy of the computed values of n_e obtained by fitting the model to the *e*-polarized SHG data was limited by the accuracy of the Sellmeier results for n_o which were described in the previous section. The precision of the computed values of n_e for all the examples given here is $\pm 5 \times 10^{-6}$ and was set by the iteration interval in the least-squares fitting procedure.

A correction to dn_e^S/dT must also be considered before discussing full wafer maps of the computed index n_e . As described earlier, for data grids composed of 361 or 441 points with $-50^\circ < \theta_i < 50^\circ$, a data acquisition session for a single wafer could take upwards of 29 h. Over this period of time the ambient lab temperature T could vary by as much as $\pm 1^\circ\text{C}$ around the typical base temperature of roughly 29°C . When the temperature fluctuated to this extent over the course of data collection, maps of $\Delta^S n_e$ displayed trends resembling the temperature history of the laboratory. These observations suggested that dn_e^S/dT as computed by the Sellmeier equation was slightly in error since temperature-induced fluctuations should not occur in maps of $\Delta^S n_e$ if the temperature dependence is correct. In the range from 28 to 32°C the Sellmeier equation predicts $dn_e^S/dT = 5.62 \times 10^{-5}$ and $dn_o^p/dT = 5.50 \times 10^{-6}$. Since the majority of the temperature-dependent birefringence is carried in n_e^S , it is reasonable to assume that only dn_e^S/dT requires correction. Wafer #35 of the sequential-cut series was used to

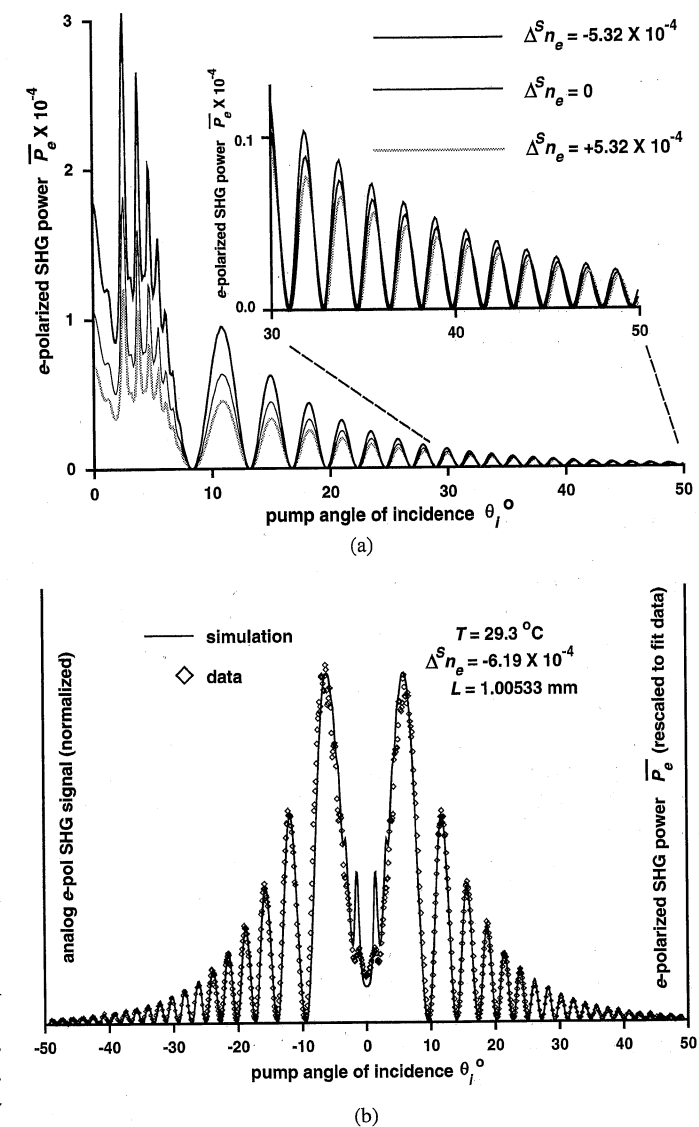


Fig. 10. (a) Simulation illustrating the effect of offsets in extraordinary index that preserve the frequency but displace the envelope of the *e*-polarized Maker fringes. $T = 30^\circ\text{C}$, $L = 1\ \text{mm}$. (b) Typical fit of simulation to *e*-polarized Maker fringe data.

estimate the correction. Repetitive Maker fringe scans were performed on a one-dimensional grid along a diameter parallel to z while the laboratory temperature was raised from 28.9 to 30.5°C . Fitting these data and averaging the results allowed us to estimate that $dn_e^S/dT = 5.48 \times 10^{-5}$ in this temperature range.

Full wafer maps of n_e scaled to a temperature of 29°C are illustrated in Figure 11(a)–(d). Figure 11(a)–(c) shows the results for three of the sequentially cut 76-mm diameter wafers taken from near the top, middle, and bottom of the boule, respectively. For these three wafers, data was collected on a 19×19 grid with a 2.444-mm mesh. Figure 11(d) illustrates the results obtained from the 100-mm diameter wafer where the data collection was performed on a 21×21 grid with a 3.00-mm mesh. In these figures, \bar{n}_e and $\Delta^S n_e$ represent the average values of n_e and $\Delta^S n_e$, respectively, for the entire wafer. These results show some typical trends. For example, a gradient in n_e is often observed that is oriented primarily

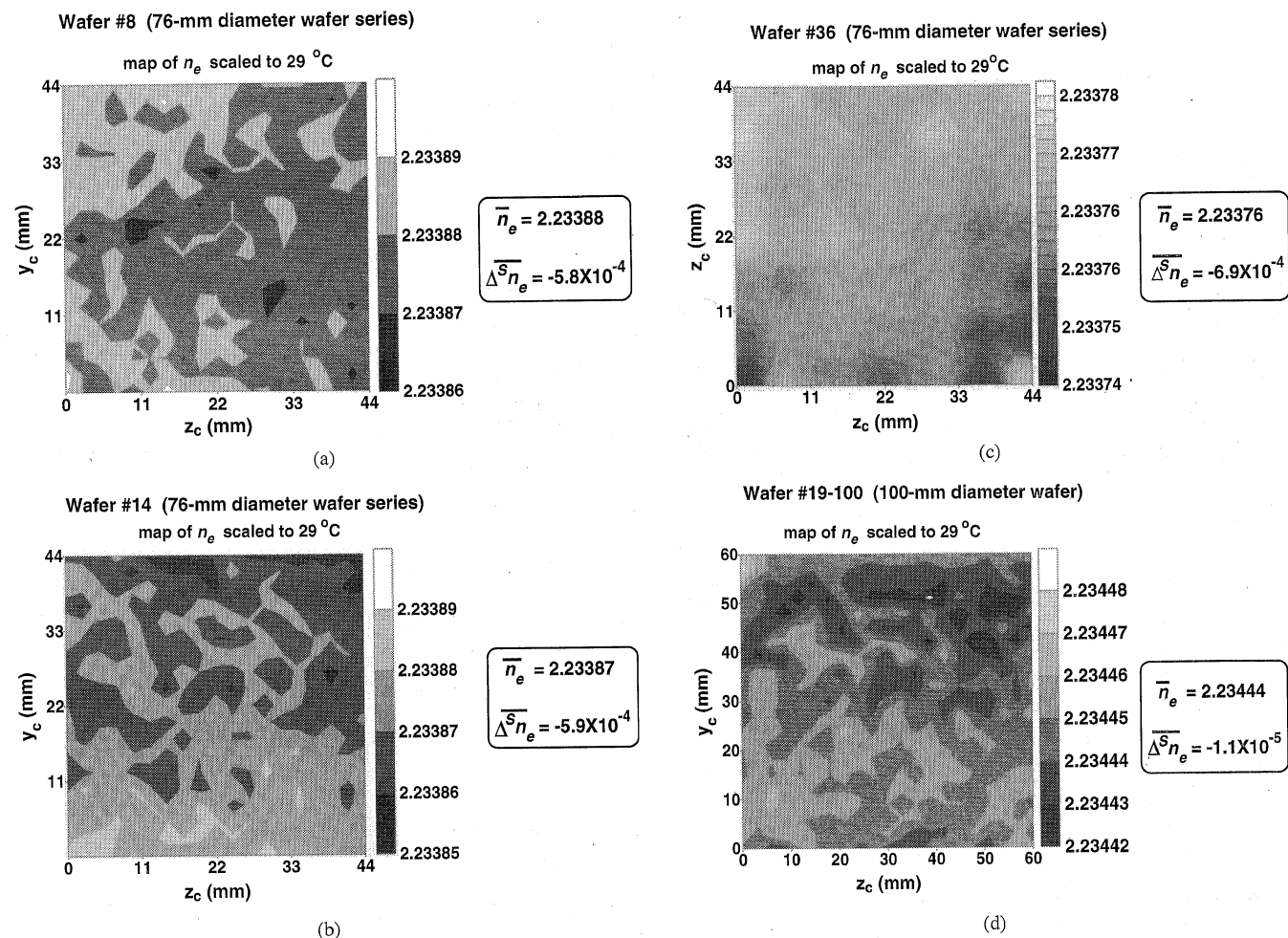


Fig. 11. (a) Map of n_e at 29°C for wafer #8 of the 76-mm diameter series. (b) Map of n_e at 29°C for wafer #14 of the 76-mm diameter series. (c) Map of n_e at 29°C for wafer #36 of the 76-mm diameter series. (d) Map of n_e at 29°C for the 100-mm diameter x-cut wafer.

in the $+z_c$ direction as shown in Figure 11(a). In Figure 11(b)–(d), however, the gradient in n_e also displays $\pm y_c$ components. It seems plausible that these effects result in part from the poling field inducing a migration of Li^+ ions. As described by Bordui et al., poling is generally performed separately from crystal growth where an electric field of roughly 0.5 V cm^{-1} is applied along the polar axis while the boule is cooled through the Curie temperature T_c ($\sim 1144^\circ\text{C}$) [38]. These conditions are thought to eliminate any poling-induced migration of Li^+ ions and associated composition variations. However, the authors also reported that more aggressive poling conditions will indeed produce composition variations on the order of $0.01 \text{ mol } \% \text{ Li}_2\text{O}$ over a distance of several centimeters. Even with low poling fields applied for an extended period of time it seems unlikely that the migration of a highly mobile ion such as Li^+ could be completely avoided especially at temperatures in the vicinity of T_c . For example, the diffusion coefficient D ($\text{cm}^2 \text{ s}^{-1}$) for Li ions in LiNbO_3 crystals at 1125°C is approximately 7×10^{-9} and 1×10^{-9} for diffusion perpendicular and parallel to the c axis, respectively, as given by Carruthers et al. [51]. Migration of Li ions under the action of electric-field poling of a boule should produce a Li-depleted portion of the crystal adjacent to the (+) poling electrode along with an increase in n_e with respect to the Li-rich portion adjacent to the (–) poling electrode. This effect is qualitatively illustrated in the results presented in

these wafer maps where the y – z trend seen in the variation in n_e is typically a few parts in 10^{-5} .

Gradients in the Li concentration are also a known consequence of crystal growth and a comparison of wafers taken from the top and bottom of a boule may show a substantial difference in \bar{n}_e . The results illustrated in Figure 11(a) and (c) for sequentially cut wafers #8 and #36, respectively, show that this is indeed the case. In general, it is difficult to maintain the preferred congruent composition, now believed to be $48.38 \text{ mol } \% \text{ Li}_2\text{O}$, for the entire growth of a crystal and it is also difficult to predict if the trend of growth will be toward a Li-rich or a Li-depleted crystal [38]. Additionally, a comparison of the results for $\Delta^S n_e$ computed for wafers taken from the sequentially cut 76-mm diameter series and the 100-mm diameter wafer reveal a substantial difference between the respective host boules. In particular, for plate #22 of the 76-mm diameter series $\Delta^S n_e = -6.6 \times 10^{-4}$ and for the 100-mm diameter plate $\Delta^S n_e = -1.1 \times 10^{-5}$. As a final comparison, a similar analysis was performed on a z-cut plate of nominal thickness 0.2 mm . In this case $\Delta^S n_e = -1.0 \times 10^{-3}$ was calculated at the SHG wavelength and $\Delta^S n_e = -6.2 \times 10^{-4}$ was calculated at the pump wavelength.

These results may be put into context by examining the literature to determine what was the most probable composition of

Variation of index and composition in LiNbO_3 boule #124

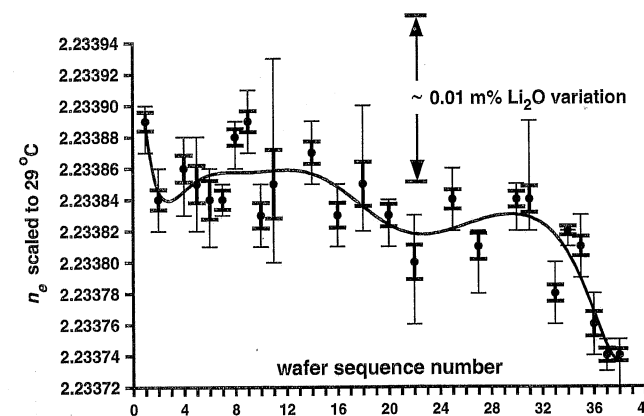


Fig. 12. Variation of \bar{n}_e for 25 x-cut wafers, all 76 mm in diameter, cut in sequence from a single boule. The heavy error bars indicate the standard deviation of \bar{n}_e for each wafer. The light error bars indicate the maximum and minimum excursion of n_e computed for each wafer. All data are scaled to a common temperature of 29°C . The polynomial fit was included only as an aid to the eye.

the LiNbO_3 samples used by Nelson and Mikulyak to measure the refractive index data that was ultimately used by Edwards and Lawrence to infer their Sellmeier equations [49, 50]. A survey of the literature that encompasses these results and the efforts of, Bordui et al. [38], Byer et al. [52], Carruthers et al. [10], and Bergman et al. [39], reveals that the composition of the Nelson's samples were most likely $\sim 48.30 \text{ mol } \% \text{ Li}_2\text{O}$. Thus, wafers indicating a relatively small value of $\Delta^S n_e$, as was the case for the 100-mm diameter plate, tend toward this reduced Li composition. This is in contrast, however, to the preferred target congruent composition of $48.38 \text{ mol } \% \text{ Li}_2\text{O}$ described by Bordui et al. for modern LiNbO_3 [38]. Finally, compiling these results further leads to the estimation that the composition dependence of the extraordinary index of refraction $dn_e/dC = -0.0112 [\text{mol } \% \text{ Li}_2\text{O}]^{-1}$. Figure 12 displays a graph of n_e as a function of wafer number for the 25 sequentially cut 76-mm diameter wafers examined. These data indicate that the top of the boule was Li_2O depleted with respect to the bottom by approximately $0.013 \text{ mol } \%$. This trend is consistent with reported limitations of Czochralski crystal growth methods where composition along the growth direction was inferred by recording variations in the bulk SHG phase matching temperature in samples measuring several mm^3 that were cut from near the top, middle, and bottom of test boules [38, 53]. The trends illustrated in Figure 12 are similar to those reported by Ivanova et al. [54]. Also displayed in Figure 12 are the standard deviations of \bar{n}_e for each wafer as indicated by the heavy error bars. The maximum and minimum excursions of n_e for the various wafers are indicated by the lighter error bars. One should note that the drawbacks of the bulk phase matching method in examining crystal homogeneity are that it requires samples several millimeters thick to obtain a phase matching peak $\sim 1^\circ\text{C}$ full width at half-maximum (FWHM), and it also requires that all or large portions of the boule be sacrificed for the measurements. In contrast, the Maker fringe analysis may be performed on finished wafers in the production stream and the results used to correlate with latter stages of device fabrication on the same wafers.

Taken together, these results illustrate that there may be a fairly wide composition space represented within a batch of wafers cut from the same boule, and an even wider space for wafers taken from separate boules. Indeed, in comparing LiNbO_3 samples supplied from a variety of manufacturers the excursion of $\Delta^S n_e$ could conceivably range from 0 to -1×10^{-3} across the set as they indeed have for the x- and z-cut samples described here. The corresponding range in composition space of $\sim 0.09 \text{ mol } \% \text{ Li}_2\text{O}$ may have a variety of consequences. For example, in their work with measuring the nonlinear χ_{ij} coefficients in a number of materials, Shoji et al. reported index data for y-cut LiNbO_3 commensurate with $\Delta^S n_e \sim -1 \times 10^{-3}$ for samples nominally 1-mm thick [46]. They also reported a lower value for $|\chi_{31}|$ (4.6 pm V^{-1}) than was commonly reported in the past. For example, Dmitriev et al. give $|\chi_{31}| = 5.44 \text{ pm V}^{-1}$ [55]. The large offset in birefringence reported by Shoji et al. may be true, however, if it is in error by a modulo 2π artifact in n_e , an exaggerated SHG amplitude in their simulation for the o-pump e-SHG case may have resulted on the y-cut sample they examined. This could then have led to an underestimation of $|\chi_{31}|$. Variations of the SHG envelope with respect to such index ambiguities were illustrated in Figure 10(a) and (b) for x-cut material and there should be no substantive difference between x-cut and y-cut plates for the present discussion. The results shown in these figures suggest that the index ambiguity of $\pm 5.32 \times 10^{-4}$ expected for plates roughly 1-mm thick could easily result in an error of $\pm 20\%$ in the measurement of $|\chi_{31}|$.

With these caveats present, a preferred approach to measure χ_{31} may be first to directly measure the ratio of χ_{31}/χ_{33} in a z-cut plate utilizing the e-pumped e-SHG Maker fringe configuration described in Figure 6(a) and Section 3.3. In this case one is always working in a regime where the coherence length is relatively low so that ambiguities in birefringence on the order of a few parts in 10^{-4} will not have a noticeable effect on the amplitude and envelope of the Maker fringes. With the ratio χ_{31}/χ_{33} established, one may then calculate χ_{31} with respect to a separately measured value of χ_{33} performed on a different sample. An alternative approach described here was to perform Maker fringe analysis in repeated succession on the z-cut plate described previously and a y-cut crystalline quartz reference plate simultaneously mounted on the rotation–translation stage assembly. SHG data were alternately collected from each plate with the pump beam maintained at the same power. The samples were mounted such that the z-cut LiNbO_3 plate was rotated about its y-axis, the y-cut quartz plate was rotated about its z-axis, and the pump polarization was maintained perpendicular to the rotation axis. The SHG produced by the quartz reference plate was modeled in a manner similar to the approach described in Section 3.3. Fitting these data required simultaneously reconciling χ_{11} for quartz with χ_{31} and χ_{33} for LiNbO_3 . The results are illustrated in Figure 13 and the simulation for LiNbO_3 included the offsets to n_e at both the pump and the SHG wavelengths that were given previously for this sample. Simultaneously fitting the SHG envelopes for quartz and LiNbO_3 required setting $\chi_{11} = 0.32 \text{ pm V}^{-1}$ for quartz with $\chi_{31} = -5.4 \text{ pm V}^{-1}$ and $\chi_{33} = -25.2 \text{ pm V}^{-1}$ for LiNbO_3 . The error for all three nonlinear coefficients was estimated at roughly $\pm 8\%$. The value for χ_{11} agrees with the results given by Hagimoto and Mito and falls within their uncertainty of $\pm 0.02 \text{ pm V}^{-1}$ [56]. The value for χ_{33} agrees with Shoji et al. and falls within their $\pm 5\%$ uncertainty [46]. However, the result for χ_{31} is larger than the value of 4.6 pm V^{-1} given by Shoji et al. but is nevertheless consistent with the results of the earlier work reported by Dmitriev [55].

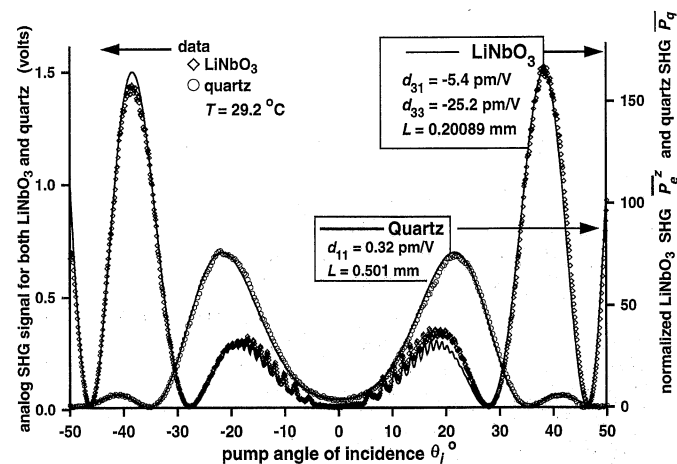


Fig. 13. Maker fringes produced by a z-cut LiNbO₃ plate compared with fringes generated under identical pumping conditions from a plate of crystalline quartz. Both samples measured roughly 1 cm² and were mounted adjacent to one another on the automated stage assembly. The system was programmed to alternatively scan one sample and then the other. Several pairs of scans were performed and compared to insure negligible drift in pump power.

3.6. Photoelastic Strain Revealed by Perturbations in the Maker Fringes for x-Cut LiNbO₃

In this section the role of static strain is explored as it contributes to the optical inhomogeneity of LiNbO₃. Strain in the material is a well-known consequence of crystal growth and is directly displayed using high-resolution X-ray diffraction imaging [57]. Index of refraction variations attributed to strain falling roughly within the range from 10⁻⁵ to 10⁻⁴ were observed by linear interferometry [58]. Observations of biaxiality in LiNbO₃ further raise the issue of strain-induced index ellipse rotations [8]. Perturbations in the Maker fringes that suggest the presence of strain were revealed by two observations. The first, and most evident, was the corruption of the weaker *o*-polarized SHG fringes by the dominant *e*-polarized fringes. This effect varied substantially between different locations on a sample and thus could not be attributed to a finite leakage of the *e*-SHG into the detection channel for the *o*-polarized signal. The second effect was an asymmetry of the *e*-polarized fringes with respect to θ_i that could not be accounted for by a systematic error in the assignment of $\theta_i = 0$ (normal incidence of the pump) in the data collection procedures. These effects were attributed to small strain-induced rotations of the optic axis about the *x*- and *y*-axes, respectively.

The intermixing of the *e*- and *o*-polarized SHG is described first. Since bulk SHG builds up as a quadratic function of length, the ratio of the maximum *e*- and *o*-polarized SHG power is approximately $(\chi_{31}l_c^{o,e}/\chi_{22}l_c^{o,o})^2 = 9.6 \times 10^3$ where the coherence lengths were given earlier (for $T = 29^\circ\text{C}$), and the values for the nonlinear coefficients were $\chi_{31} = -5.4 \text{ pm V}^{-1}$ and $\chi_{22} = 2.2 \text{ pm V}^{-1}$ [59]. The corresponding approximate ratio of the normalized *e*- and *o*-polarized SHG power is $\bar{P}_e/\bar{P}_o = (l_c^{o,e}/l_c^{o,o})^2$ with $\bar{P}_e/\bar{P}_o = 1.6 \times 10^3$. These estimates may be verified by comparing the amplitude scales of the normalized *e*- and *o*-polarized SHG power illustrated in Figures 10 and 7, respectively. With these observations and the help of Figure 14(a), one can intuitively see that a strain-induced index ellipse rotation ζ of the optic axis *z* about *x* that results in a projection of only $\sim 10^{-3}$ of the *e*-polarized SHG

amplitude $E_z^{(T_2)o}$ onto the analyzer (laboratory) y_L -axis will result in the corruption of the *o*-polarized SHG fringes. Evidence for this effect is readily seen in the superimposed *o*- and *e*-polarized SHG data shown in Figure 14(b). The extra structure appearing in the *o*-polarized SHG fringe data that aligns exactly with the simultaneously recorded *e*-polarized SHG are indicated by the arrows.

Modeling this effect was described by Sanford and Aust [44]. They defined a factor P_o which represents the total normalized *o*-polarized SHG power resulting from the vector addition of $\hat{y}E_y^{(T_2)o}$ and the component of $E_z^{(T_2)o}$ projected onto y_L where

$$P_o = |\chi_{22}E_y^{(T_2)o}|^2 + |\zeta\chi_{31}E_z^{(T_2)o}|^2 + 2\zeta\chi_{22}\chi_{31}\text{Re}\{E_y^{(T_2)o}[E_z^{(T_2)o}]^*\} \quad (13)$$

Under the assumption that static strain is the only mechanism that contributes to the rotation and associated index perturbations, an approximate relation between strain and ζ may be derived with

$$\zeta \cong \frac{(n_en_o)^2}{(n_e^2 - n_o^2)} [P_{41}(S_1 - S_2) + 2P_{44}S_4] \quad (14)$$

A discussion of the photoelastic properties of LiNbO₃ was given by Weiss and Gaylord [60]. Values for the photoelastic tensor elements $P_{44} = 0.146$ and $P_{41} = -0.151$ were given by Avakyants et al. [61]. Using least-square solution routines to fit the *o*-polarized SHG data to Eq. (13), one finds that $|\zeta|$ may vary in the range from 0 to 0.007 rad over a wafer. Equation (14) then suggests that the corresponding aggregate strain varies in the range from 10⁻⁴ to 10⁻³ but it is not possible to separate the contribution of the axial strain components S_1 and S_2 from the shear component S_4 . Maps of ζ computed for wafers #4, #14, and #30 taken from near the top, middle, and bottom of the 76-mm diameter set are shown in Figure 14(c)–(e). These results suggest that wafers cut from near the center of the boule carry less variation in strain over equivalent cross-sectional areas than those taken from either end. The observation that the maps of ζ also display annular features further suggests an association with thermal gradients during crystal growth.

The second phenomena that may be attributed to strain was observed directly in the *e*-polarized SHG fringes. In many cases, asymmetric shifts of the *e*-polarized fringes with respect to θ_i were observed. These effects were distinct from the symmetric fringe displacements associated with composition dependent variations in n_e between remote scan locations as discussed in Section 3.5. The asymmetric fringe shifts compel consideration of a strain-induced index ellipse rotation ϑ about the *y*-axis and inclusion of this as a variable parameter in the least-square routines used to fit the *e*-polarized SHG fringes. An approximate expression for ϑ was given by Sanford and Aust [44],

$$\vartheta \cong \frac{(n_en_o)^2}{(n_e^2 - n_o^2)} [P_{44}S_5 + P_{41}S_6] \quad (15)$$

Once again an aggregate strain of approximate magnitude 1×10^{-4} was found and results in a rotation ϑ of $\sim 1 \times 10^{-3}$ rad. A simulation of this effect for $\vartheta = 2 \times 10^{-3}$ rad is illustrated in Figure 15(a) and shows the magnitude of asymmetric fringe displacement where the nulls near $\theta_i = \pm 10^\circ$ are both shifted by approximately 0.4° . A displacement of these fringes by about the same magnitude which is symmetric with respect to θ_i occurs for a variation in n_e of approximately 5×10^{-6} . In this case the null near

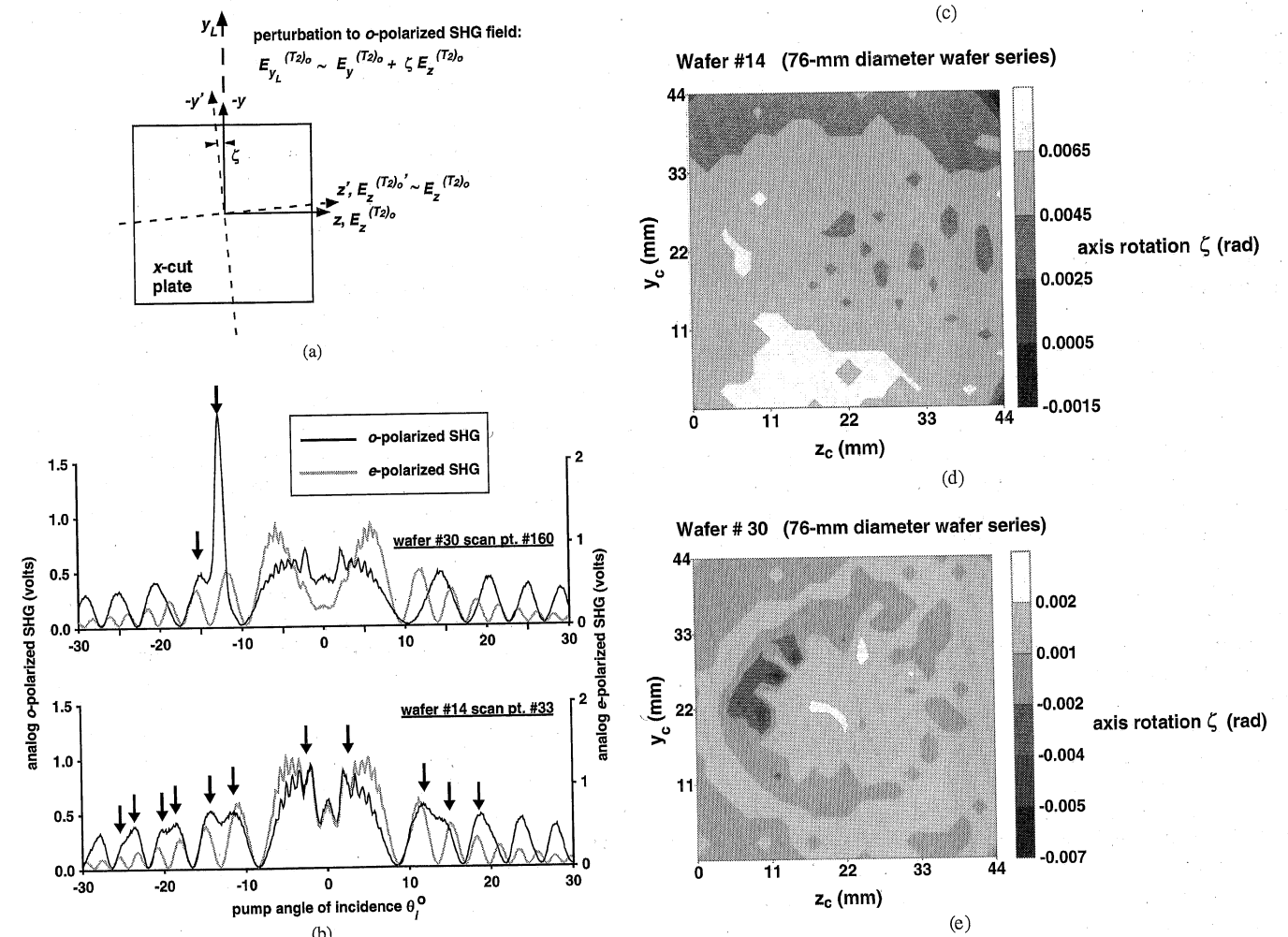


Fig. 14. (a) Schematic showing the strain-induced rotation ζ of the optic axis about *x* for an *x*-cut plate. Also illustrated is the resulting projection of the *e*-polarized SHG field onto the analyzer axis y_L of the detection optics for the *o*-polarized SHG. (b) An example of data illustrating the corruption of the weaker *o*-polarized Maker fringes by the dominant *e*-polarized SHG is shown for the locations indicated on the 76-mm diameter wafers #14 and #30. (c) A full wafer map of the axis rotation ζ for wafer #4 of 76-mm diameter series. (d) A full wafer map of the axis rotation ζ for wafer #14 of 76-mm diameter series. (e) A full wafer map of the axis rotation ζ for wafer #30 of 76-mm diameter series.

10° will be shifted by roughly -0.4° and the null near -10° will be shifted roughly 0.4° . Strains that produce rotations of the index ellipse about x or y by $\sim 10^{-3}$ rad directly perturb n_o and n_e by $\sim 10^{-6}$. Thus, the primary effects of these index ellipse rotations that emerge in the Maker fringe data are the mixing of the o - and e -polarized fringes, and asymmetric angular displacements of the e -polarized fringes. Direct index variations of n_o and n_e on the order of 10^{-6} leading to symmetric displacement of the fringes, similar to that discussed in Section 3.5 in regard to the composition dependence of the birefringence, are not resolved. Maps of ϑ for the 100-mm diameter x -cut wafer and wafer #14 of the 76-mm diameter series are shown in Figure 15(b) and (c), respectively. The results for the 100-mm diameter illustrate that ϑ displays a gradient with respect to z which is apparently associated with the poling field of the boule. On the other hand, wafer #14 of the 76-mm diameter series is rather featureless in this regard.

These approximate photoelastic analysis methods cannot be regarded as a means to extract absolute strain in LiNbO₃ since, for example, some stray leakage of the e -polarized SHG will always be present in the o -SHG detection optics either through slight alignment errors of the samples in the Maker fringe system or through the extinction limit of the polarizers. This possibility was tested by adding a constant background contribution of the e -polarized SHG into the solution procedures for computing the admixture of the e -polarized SHG into the o -polarized SHG. The numerical results indicated that such a constant background addition did not substantially change the computed maps of ζ .

The possibility was also considered that static internal electric fields may contribute to a rotation of the optic axis about x or y via contributions of the linear electro-optic effect and the converse piezoelectric effect. However, these effects were determined to be minimal in most instances and the rationale supporting this conclusion is now described. For example, Prokhorov described a model whereby thermal cycling will produce excess pyroelectric charging at grain boundaries in a LiNbO₃ crystal [8]. Moreover, internal electric fields arising in part from polarized defect sublattices are known to exist in the material [62–64]. Misorientation of grains on the order of 10^{-3} rad could then result in x - or y -directed static electric fields resulting from x or y projections of the primary z -directed pyroelectric or internal fields generated within the grains. However, the magnitude of such fields must be on the order of 1 kV mm^{-1} to produce a rotation of the optic axis by approximately 10^{-3} rad. The typical magnitude of these z -directed internal fields is on the order of $1\text{--}10 \text{ kV mm}^{-1}$. A misorientation of 10^{-3} rad would then produce x - or y -directed fields of approximate magnitude 1 V mm^{-1} which are insufficient to generate the rotation of the optic axis observed via the linear electro-optic effect. One can also consider the effects of the strong internal electric fields producing strains via the converse piezoelectric effect [60]. Using the simplified matrix notation, the converse piezoelectric effect links strains S_j produced by static electric fields E_i through the piezoelectric tensor d_{ij} where $S_j = d_{ij}E_i$. Thus, the nonzero elements of strain resulting from the dominantly z -directed internal field are $S_1 = d_{31}E_3$, $S_2 = d_{32}E_3$, and $S_3 = d_{33}E_3$. The strains S_1 and S_2 are equal since $d_{31} = d_{32}$. Comparing these results with Eqs. (14) and (15) again leads one to the conclusion that primarily z -directed internal fields do not significantly contribute to the strain-induced rotations of the optic axis. Strains S_1 and S_2 arising from internal fields cancel out of Eq. (14) and strain S_3 does not appear in either Eq. (14) or Eq. (15). In Section 4.2.3, perturbations to Maker fringes produced by z -cut

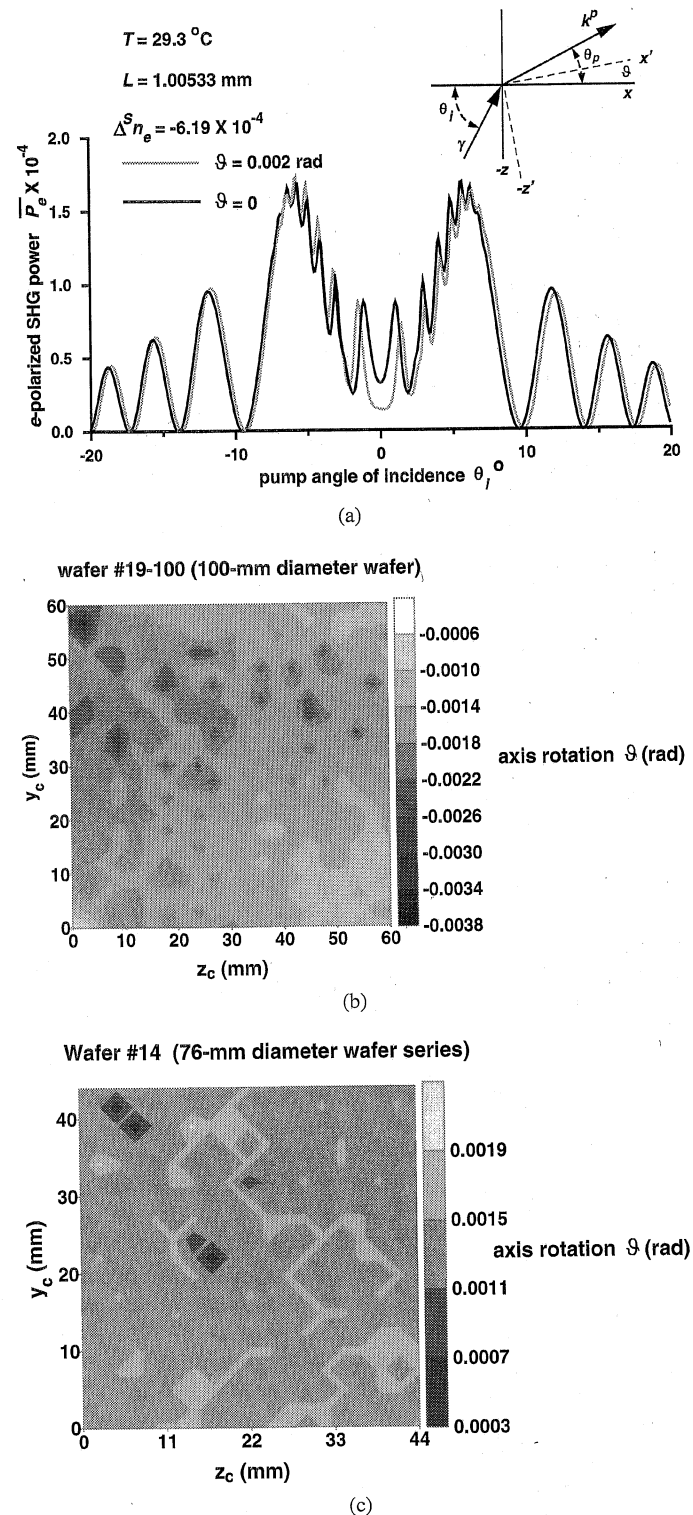


Fig. 15. (a) The effect on the e -polarized SHG of a rotation ϑ of the optic axis about y is illustrated. (b) A full wafer map of ϑ for the 100-mm diameter x -cut LiNbO₃ plate. (c) A full wafer map of ϑ for wafer #14 of the 76-mm diameter series.

LiNbO₃ plates subjected to internal and external z -directed electric fields on the order of several kilovolts per millimeter are discussed.

3.7. Concluding Remarks

Maker fringe analysis is a powerful measurement tool for finished LiNbO₃ wafers that offers simultaneous nondestructive evaluation of composition, refractive index, strain variations, wafer thickness, taper, r_{ij} coefficients, in addition to the more traditional measurements of the nonlinear optical χ_{ij} coefficients. The analysis method also lends itself to process evaluation of integrated optical devices since features near the surface resulting from mechanical or chemical processing that perturb the optical properties to a depth on the order of a coherence length may be resolved. For example, examining the uniformity of an annealed proton-exchanged layer in x -cut LiNbO₃ using Maker fringe analysis was described by Sanford and Aust [41]. With the increasing application demands being placed on the material, such a range of metrologies may become more important for complete characterization of a wafer prior to device processing or at various stages of processing. An important issue that requires further examination is the influence of composition variations on the fabrication yield and performance of various integrated optical devices. As reflected in part through Refs. [27–36], significant progress was made in this regard, however more work is required to more fully correlate the dependence of waveguide fabrication methods and finished device performance within the composition space of the base material. Device performance and yield issues for high-speed integrated optical modulators and gyro components include transverse mode size, waveguide loss, modulator drive voltage, uniformity of oxide-substrate interfaces, strains induced by oxide layers and electrodes, and the splitting ratio of branched waveguide structures. Concerns for nonlinear optical devices include the correlation of wafer uniformity with the yield of PPLN fabrication, domain uniformity, and the reliable fabrication of structures which simultaneously combine PPLN and optical waveguides on the same substrate.

4. FERROELECTRIC DOMAINS AND DOMAIN WALLS

4.1. Introduction

The crystal structure of ferroelectric LiNbO₃ and LiTaO₃ belong to the space group of $R3c(C_{3v})$ with rhombohedral (trigonal) symmetry and classified as oxygen octahedra, ferroelectrics. The framework of the crystal structure is composed of oxygen octahedra which are joined together by their faces as shown in Figure 16 [65–70]. The octahedra are two-thirds filled (one-third each by Li and transition metals Nb or Ta) and one-third empty. In the high temperature prototype phase, ($R\bar{3}c$) the crystal structure is paraelectric, transforming to a ferroelectric phase through a second-order phase transition at 1198°C (1138°C) for stoichiometric (congruent) LiNbO₃ [25, 71] and $\sim 690^\circ\text{C}$ (601°C) for stoichiometric (congruent) LiTaO₃ [14]. The structural transformation accompanying this phase transition is the movement of both lithium and transition ions along the trigonal symmetry axis with respect to the oxygen sublattice. The transition ion (Ta or Nb) moves from the center of the octahedra to an asymmetric occupation site along the threefold rotation axis (the trigonal axis). The

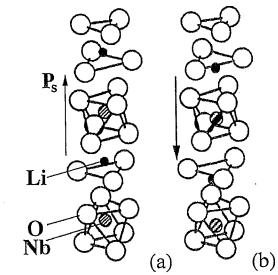


Fig. 16. (a) Schematic of the crystal structure of lithium niobate and lithium tantalate. (b) Cation positions in the paraelectric and ferroelectric phases.

mean position of the lithium ion shifts along the trigonal axis in the same direction as the Ta (or Nb) movement, from the center of a close-packed oxygen triangle into the neighboring octahedra. This leaves the other octahedra adjacent to the oxygen triangle empty. The creation of a spontaneous ferroelectric polarization, P_s is a direct consequence of this relative movement of oxygen and cations in the lattice. This unique trigonal axis is denoted c -axis or z -axis. Since the movement of cations can be in any one of the two antiparallel directions along the trigonal axis, the spontaneous polarization can be created along any of these two different directions, $+P_s$ or $-P_s$ as shown in Figure 16. Any uniformly polarized region is called a domain, and two different regions in a crystal exhibiting $+P_s$ and $-P_s$ polarizations, are separated by a 180° domain wall, so called because the polarization is reversed by 180° across the wall. The trigonal symmetry also results in three polar axes (typically denoted by axis $+y$) perpendicular to the z -axis which are 120° apart and lie in the three c -glide planes which are parallel to the z -axis. Figure 17 schematically shows the normal view of the close-packed oxygen planes perpendicular to the x -axis. There exist three different O–O bond lengths in a given close-packed oxygen plane, the largest among them being the oxygen triangle separating the lithium-occupied and the empty octahedra.

The crystal structure can be represented as either hexagonal, rhombohedral, or the orthorhombic unit cells. The interrelations between these three axes systems is also shown in Figure 17. The three x -axes in Figure 17 represent the hexagonal axes, the (x, y) axes represent the orthorhombic axes, and the three y -axes, represent the rhombohedral axes. The most commonly used axes notation among crystal growers are the cubic, x -, y -, and z -axes. The x -, y -, and z -cut crystals refer to the planes of the crystal defined by the surface normal along x , y and z , respectively.

As a ferroelectric, the spontaneous polarization P_s is reversible by external electric fields. Indeed this process of electric-field patterning of domains into diverse shapes such as gratings, lenses, and prisms is key to a large family of nonlinear-optical devices that perform laser light scanning [72] focusing [73] and frequency conversion [74]. Ironically, domain reversal in these materials was considered impossible at room temperature until lately. Extrapolating from the dependence of coercive field dependence with temperature from $200\text{--}620^\circ\text{C}$ for LiTaO₃, Ballman et al. [75] estimated a coercive field of $\sim 5 \text{ MV mm}^{-1}$ at room temperature, which is far in excess of the breakdown voltage of the material, hence precluding domain inversion at room temperature. A similar conclusion was drawn for lithium niobate [7]. These conclusions were further justified by arguing that for the domain-inversion process, the lithium ions have to pass through an adjacent oxygen triangle in

the close-packed oxygen plane. At room temperature, the smallest ion that could pass through this oxygen triangle is estimated to be ~ 0.62 Å in LiNbO_3 and ~ 0.63 Å in LiTaO_3 , which are less than the ionic radius for lithium (0.68 Å). Therefore Megaw [7] labeled LiNbO_3 as a frozen ferroelectric. Niizeki et al. [76] calculated the radius of the opening in the oxygen triangle adjacent to the lithium ion as a function of temperature, based on the lattice parameter data of Abrahams et al. [68–70]. This data showed that only after 200°C, the opening in the oxygen triangle enlarges significantly enough to allow a lithium ion through the layer, and allowing domain inversion in LiNbO_3 . All the previous studies on domain switching appear to have been performed on nonstoichiometric compositions of LiNbO_3 and LiTaO_3 crystals.

One of the significant advances made is that domain inversion is shown to be possible at room temperature under external fields. The coercive fields for congruent crystals are found to be ~ 21 – 22 kV mm $^{-1}$ at room temperature which is ~ 250 times lower than the predicted value by Ballman et al. [75]. Further, the coercive field shows a large sensitivity to the lithium concentration in the crystals [77, 78]. The lithium deficiency in single crystals of LiNbO_3 and LiTaO_3 appears to give rise to a range of other physical phenomena, such as built-in internal fields [64, 79] optical birefringence strains, and electric fields at the domain walls [81, 82] and a change in the preferred domain wall orientations. These are the topics covered in this chapter.

4.2. Domain Reversal

4.2.1. Ferroelectric Hysteresis at Room Temperature

The domain reversal in z-cut LiNbO_3 and LiTaO_3 crystals sensitively depends on the lithium stoichiometry and temperature. The starting z-cut crystals used for the studies reported by

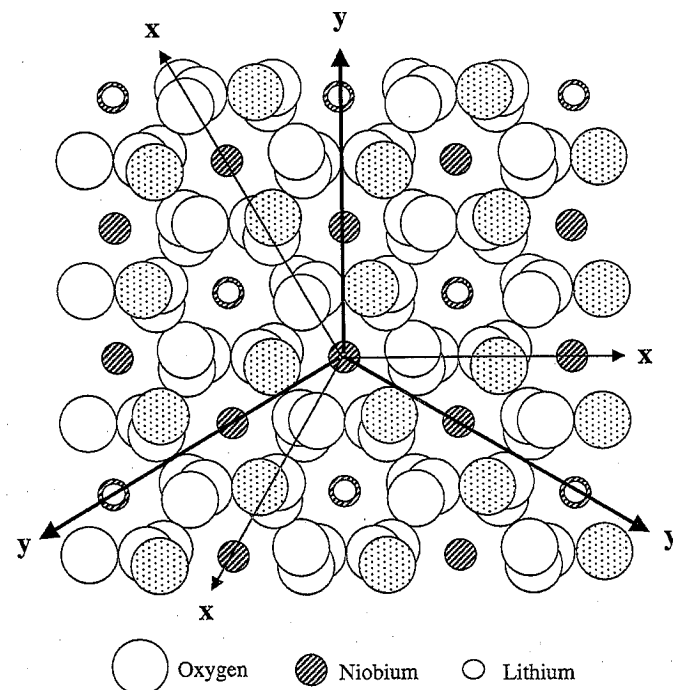


Fig. 17. The [0001] projection of the crystal structure of LiNbO_3 and LiTaO_3 .

Gopalan et al. [64, 79] were of optical grade, of congruent composition, and single domain. They were referred to as “virgin crystals” and their domain state referred to as State I. The polarization of the crystal is reversed at room temperature by applying a dc field across the crystal thickness. The electrodes are typically water

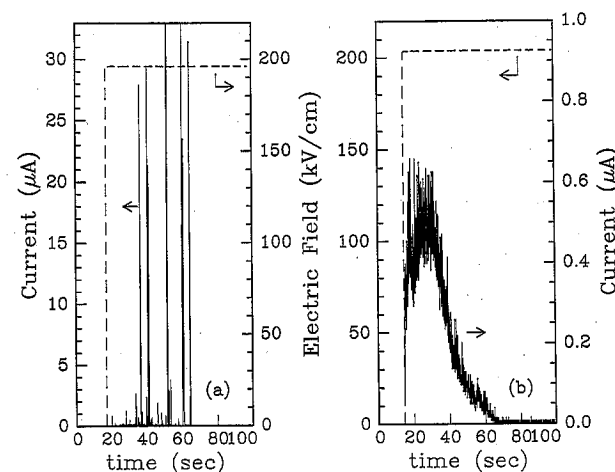


Fig. 18. Transient currents observed during domain reversal for (a) congruent LiNbO_3 (b) congruent LiTaO_3 . Reprinted from V. Gopalan, T. E. Mitchell, and K. E. Sickafus, *Solid State Commun.*, 109, 111 (1999).

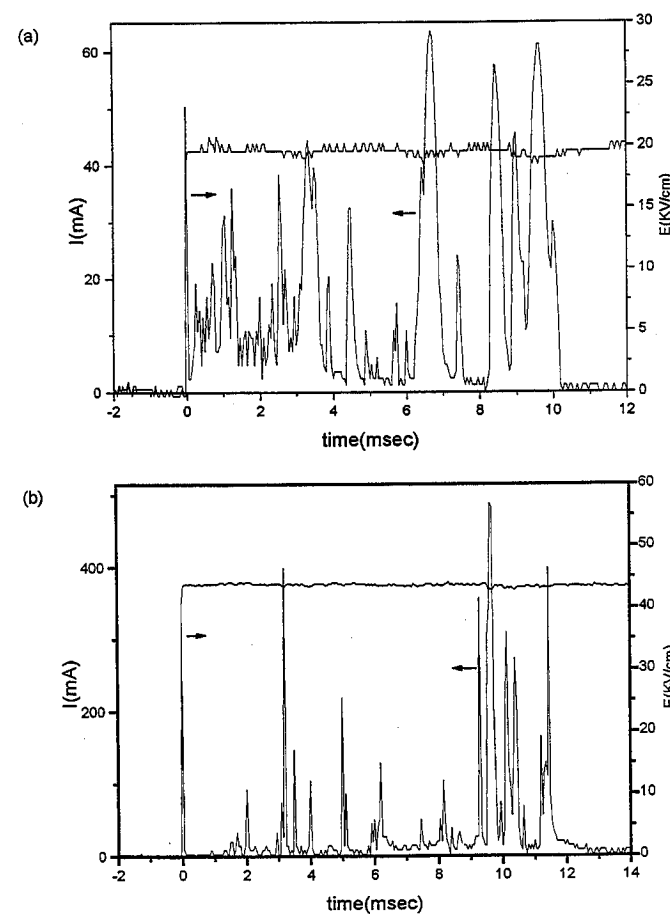


Fig. 19. Transient currents for (a) stoichiometric LiTaO_3 (b) stoichiometric LiNbO_3 .

based salt solutions of nitrates (such as MgNO_3 , KNO_3) or chlorides (e.g., LiCl). Metal films of Au, Pt, Ta, can also be deposited on the positive and negative z-faces and can be used as electrodes. Examples of transient currents, i , observed during domain reversal is shown for both congruent LiNbO_3 and LiTaO_3 in Figure 18(a) and (b), respectively, and for stoichiometric LiNbO_3 and LiTaO_3 in Figure 19(a) and (b). The applied electric field is either linearly ramped, or applied as steps or pulses. The total integrated charge, q , under the current pulses is given by $q = \int i dt = 2P_s A$ where A is the area of the electrodes, and P_s is the spontaneous polarization. This is used to measure the spontaneous polarization of the crystals, which is ~ 75 – 80 $\mu\text{C cm}^{-1}$ for LiNbO_3 [77] and ~ 50 – 55 $\mu\text{C cm}^{-1}$ for LiTaO_3 [78] at room temperature. It is seen from Figures 18 and 19 that the transient currents occur as “spikes” in stoichiometric crystals. However, while the spike nature is observed in congruent LiNbO_3 as well, it is a continuous curve in congruent LiTaO_3 . These differences are directly reflected in the dynamics of domain motion as discussed in detail in Section 5. The polarization hysteresis loops for stoichiometric and congruent LiNbO_3 and LiTaO_3 crystals at room temperature are shown in Figure 20(a) and (b). The hysteresis loops are for the first cycle only, that is, the ferroelectric polarization was cycled from its initial state (virgin state), through 180° then back to State I. The first domain reversal

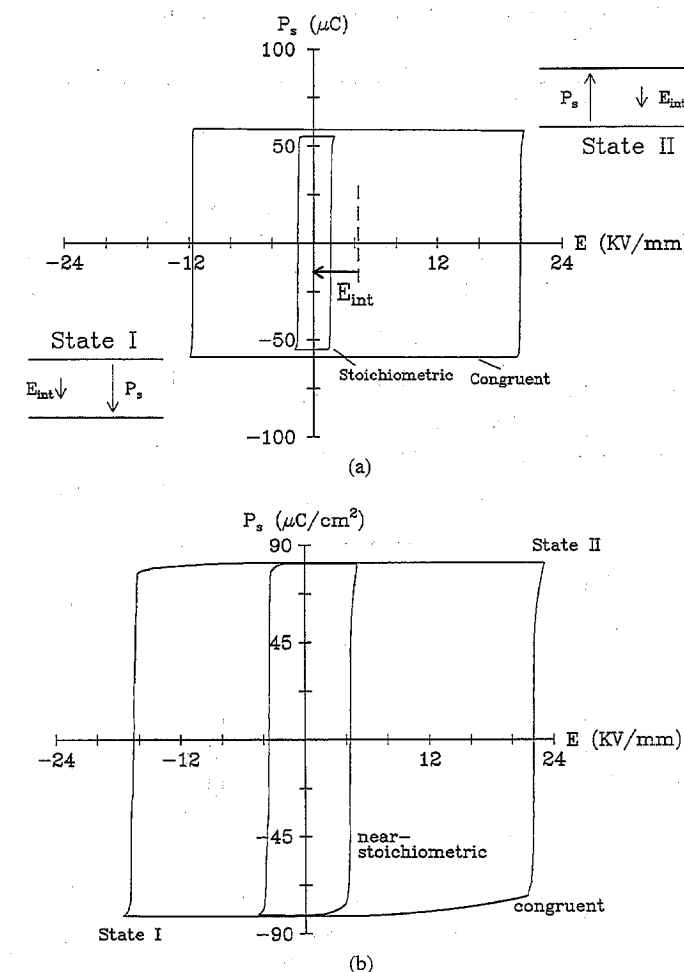


Fig. 20. Hysteresis loops for (a) stoichiometric and congruent LiTaO_3 , (b) stoichiometric and congruent LiNbO_3 .

on a virgin crystal is referred to as “forward” poling and the second reversal is referred to as “reverse” poling. The coercive field for forward domain reversal is denoted E_f and the reverse domain reversal is denoted as E_r . The large offset in the hysteresis loops of the congruent crystals along the field axis is termed internal field, given by $E_{\text{int}} = (E_f - E_r)/2$.

4.2.2. The Influence of Lithium-Nonstoichiometry on Domain Reversal

The coercive field for domain reversal is sensitive to the lithium stoichiometry. Figure 21(a) and (b) shows the dependence of the coercive field and the internal field as a function of lithium nonstoichiometry in the lithium niobate and lithium tantalate crystals, respectively. The lithium stoichiometry, $C(\%) = [\text{Li}_2\text{O}]/([\text{Li}_2\text{O}] + [\text{Nb}_2\text{O}_5 \text{ or } \text{Ta}_2\text{O}_5])$, was estimated from the Curie temperature using the equations [23, 25],

$$T_c (\text{°C}) = 9095.2 - 369.05C + 4.228C^2 \quad (\text{for } \text{LiNbO}_3) \quad (16a)$$

$$T_c (\text{°C}) = -1054.2 + 34.682C \quad (\text{for } \text{LiTaO}_3) \quad (16b)$$

The coercive fields E_f and E_r , in (kV mm $^{-1}$) and the internal field $E_{\text{int}} = (E_f - E_r)/2$ from Figure 21 can be written for LiNbO_3 as a function of Curie temperature (T_c in degrees Celsius)

$$E_f = 335.9(\pm 45.7) - 0.277(\pm 0.039)T_c \quad (17a)$$

$$E_r = 249.0(\pm 46.6) - 0.204(\pm 0.040)T_c \quad (17b)$$

$$E_{\text{int}} = 42.3(25.9) - 0.035(\pm 0.022)T_c \quad (17c)$$

For LiTaO_3 , these values are only available for the stoichiometric and the congruent compositions [78]. However, drawing analogy from the linear relationships (17a)–(17c) for LiNbO_3 , one can write the relationship between E_c (kV mm $^{-1}$) and T_c (°C) as

$$E_f \sim 149.54 - 0.2159T_c \quad (18a)$$

$$E_r \sim 84.06 - 0.1205T_c \quad (18b)$$

and $E_{\text{int}} = (E_f - E_r)/2$. The internal field, E_{int} , refers to the large offsets along the field axis in Figure 20. These fields range from $E_{\text{int}} \sim 4$ – 5 kV mm $^{-1}$ for congruent LiTaO_3 and ~ 2 – 3 kV mm $^{-1}$ for congruent LiNbO_3 crystals at room temperature and tend to disappear in the stoichiometric crystals. The origin and characteristics of internal fields is discussed next.

4.2.3. Maker Fringe Analysis of Internal Fields in Congruent LiNbO_3

The experimental studies by Aust [45] in electric-field induced domain reversal and Maker fringe analysis of congruent z-cut LiNbO_3 plates are now described. Room-temperature electric-field poling was performed on samples that were ~ 0.2 -mm thick. The poling technique involved placing the sample in a liquid electrode cell containing a LiCl aqueous electrolyte which permitted isolated electrical contact to opposing portions of the positive and negative faces of the plate. High voltage pulses were applied across the sample and produced electric fields exceeding the coercive field of (approximately 21 kV mm $^{-1}$). These pulses were effective in nucleating and driving a uniform domain through the bulk of the sample only for the regions whose surfaces were exposed to

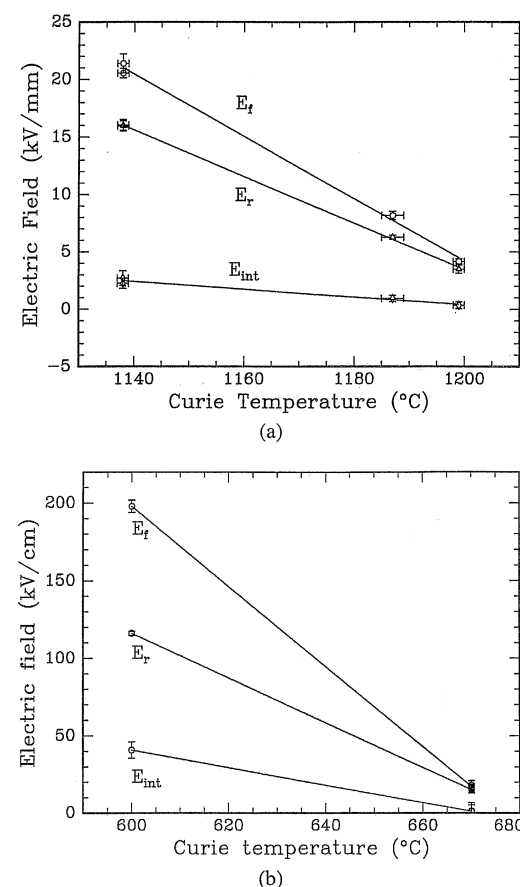


Fig. 21. Change in coercive fields for domain reversal with lithium stoichiometry for (a) lithium niobate reprinted with permission from V. Gopalan et al., *Appl. Phys. Lett.*, 72, 1981, (© American Institute of Physics); and (b) lithium tantalate. Reprinted with permission from K. Kitamura et al., *Appl. Phys. Lett.*, 73, 3073, (© 1996 American Institute of Physics).

the electrolyte. The entire procedure was carried out at room temperature. Thus, the direction of the new domain was antiparallel to the original domain orientation in the as-received (virgin) crystal and the process is typically referred to as domain reversal or electric-field poling. This basic procedure is described in detail by a number of workers [28, 45].

Preliminary work involving Maker fringe analysis on room-temperature electric-field poled sections of z-cut LiNbO₃ showed anomalous shifts between SHG fringes recorded at the same location on a sample before and after domain reversal [83]. These shifts could be simulated by apparent thickness variations of $\sim 0.1 \mu\text{m}$ between the inverted and original sections. An example of this fringe shift is illustrated in Figure 22(a) where the plate was rotated about the y-axis and both the pump and SHG were o-polarized (parallel to y). This early result suggested that the action of room-temperature electric-field poling may have completely poled through a native domain-inverted layer residing on the +z-face of the material. Indeed, domain-inverted layers on z-cut material were reported by a number of workers [84, 85]. Furthermore, high-resolution X-ray diffraction imaging (HRXDI) data suggested the existence of such an inverted layer. In HRXDI there is a contrast in the images between the +z- and -z-faces due to the different form factors. Aust et al. observed that the

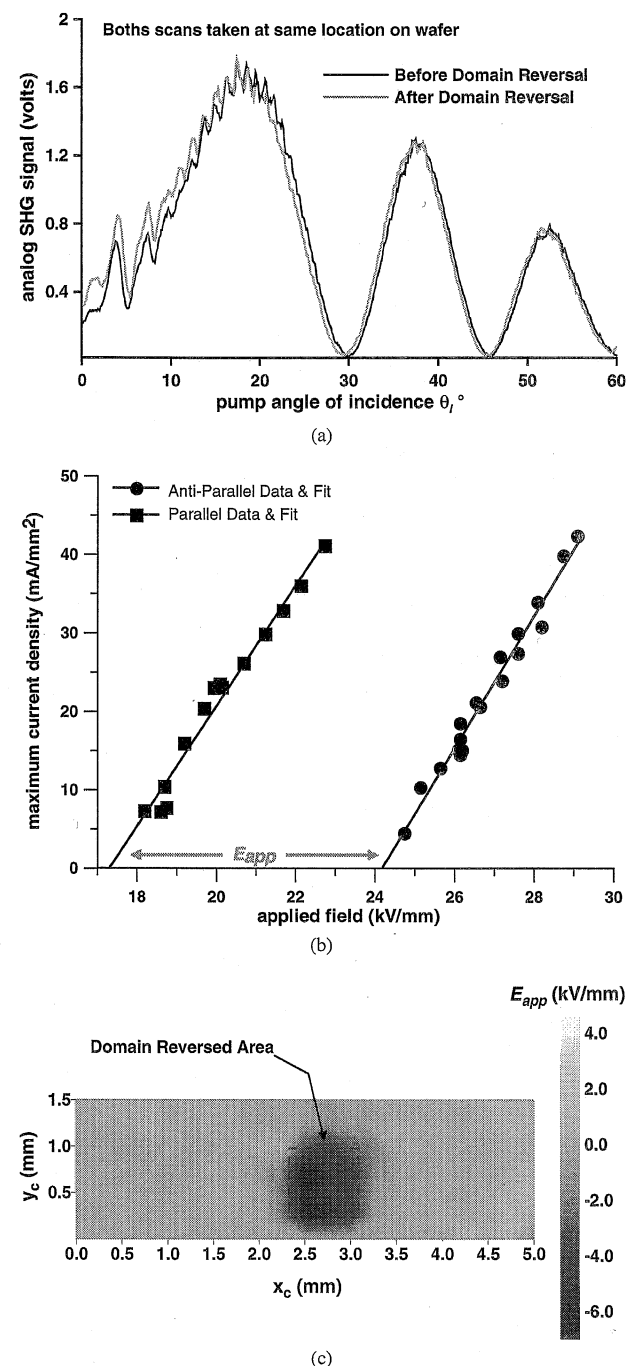


Fig. 22. (a) Maker fringes scans taken at the same location on a z-cut LiNbO₃ plate before and after room-temperature electric-field poling. The results illustrate the effect of poling in shifting the o-polarized SHG fringes. The sample was rotated about y and both the pump and SHG were polarized parallel to y. (b) The characteristic poling current features of repeated antiparallel and parallel room-temperature electric-field poling are illustrated. The z-cut sample was nominally 0.2-mm thick. (c) A map illustrating fitting o-polarized SHG fringe data collected on a rectangular array of a z-cut plate that contained a domain-inverted region. Pumping conditions are as described in (a). The fitting parameter is a static z-directed electric field E_{app} that perturbs the indices of refraction through the linear electro-optic effect. In computing this map, the corresponding thickness data at each grid location was computed from a Maker fringe data set collected prior to domain reversal. This simulation neglected piezoelectric strain perturbing the thickness of the inverted area and used values for the electro-optic coefficients taken from literature as described in the text.

HRXDI image contrast between the +z- and -z-regions on the original +z-face was lower than that on the original -z-face for a domain-reversed sample [83]. These observations support the contention that a native domain-inverted layer could be present on the +z-face. Domain-inverted layers notwithstanding, it was found that the anomalous shifts in the Maker fringes illustrated in Figure 22(a) could be annealed away by temperature cycling the sample to $\sim 200^\circ\text{C}$ as described in detail in the next section. This fact pointed toward mechanisms more akin to sublattice or defect polarization fields, internal fields associated with poling hysteresis asymmetry, or poling-induced strain leading to photoelastic shifts in the Maker fringes [80, 82, 86].

Repeated antiparallel (forward) and parallel (reverse) poling of the same section of a z-cut LiNbO₃ plate revealed an inequality in the respective poling fields and the presence of a static internal electric field aligned in the same direction as the field associated with the spontaneous polarization of the original domain orientation. These results are illustrated in Figure 22(b). The offset ($E_f - E_r$) in the electric field between the antiparallel (or forward) poling case and the parallel (reverse) poling cases in this wafer is approximately $6.9 \pm 0.2 \text{ kV mm}^{-1}$. This is labeled as E_{app} in Figure 22(b). Thus, the coercive field necessary to restore the inverted domain to its original orientation (reverse poling) is approximately 6.9 kV mm^{-1} less than the coercive field required for the initial (forward) domain reversal. There are a number of ways to represent the internal field associated with the observed offset in the parallel and antiparallel coercive fields. For example, Gopalan defined an internal field E_{int} such that $2E_{int} = E_{app}$ as described previously [64]. This definition enables viewing the data of Figure 22(b) as conforming to symmetric hysteresis. The view adopted by Aust [45] is that the as-received sample is in a quiescent state whereby the presence of static internal fields are already accounted for in the bulk optical and mechanical properties of the material. Performing domain inversion on the sample, however, places it in an electrically biased state which is optically indistinguishable from applying a static field of approximate magnitude 6.9 kV mm^{-1} across the sample. Indeed, as described in the following discussion, the shifts in the Maker fringes illustrated in Figure 22(a) were accounted for with this model. Finally, it should be noted that a sample that was forward poled and subsequently annealed at $\sim 200^\circ\text{C}$ for several minutes will display a reversal in the sense of E_{app} as described in Section 4.2.4.

Additional Maker fringe work was performed to examine a $0.75 \times 0.75\text{-mm}$ forward poled region on the sample. Two sets of scans were collected on a common grid over a $5 \text{ mm (x)} \times 1.5 \text{ mm (y)}$ area before and after electric-field poling. The domain-reversed section was imbedded within the larger area. The initial data were used to compute the sample thickness over the grid. The data collected after antiparallel poling in conjunction with the thickness data were then used to fit the second data set to an apparent applied electric field E_{app} . Here, the viewpoint was adopted that the sample is in an unclamped state of constant stress where the electro-optic matrix r_{ij} is defined by $r_{ij} = r_{ij}^s + p_{ik}d_{jk}$. The quantity r_{ij}^s is the electro-optic matrix under clamped (constant strain) conditions, p_{ik} is the photoelastic matrix, and d_{jk} is the piezoelectric matrix. Once again, the simplified matrix representation of these tensor quantities was utilized [60]. The map of E_{app} resulting from this data fitting analysis is illustrated in Figure 22(c). The figure clearly shows the poled area standing out in contrast with the surrounding background crystal. The values for r_{13} and r_{33} used in computing this map were

Table III. Electro-optic Coefficients of LiNbO₃ Expressed in $\text{mm kV}^{-1} \times 10^{-5}$ from Mendez et al. Extrapolated with the Results of Weiss and Gaylord*

Wavelength = 1064 nm		Wavelength = 532 nm	
$r_{13} = 0.8$	$r_{33} = 3.1$	$r_{13} = 1.0$	$r_{33} = 3.2$

*Source: A. Mendez et al., *Electron. Lett.*, 35, 499, (1999); R. S. Weiss and T. K. Gaylord, *Appl. Phys. A: Solids Surf.*, 37, 191, (1984).

taken from Mendez et al. and listed in Table III [87]. However, one should note that the electro-optic coefficients near 1064 given by Mendez et al. [87] appear somewhat anomalous so the values listed in Table I were extrapolated with the aid of data given by Weiss and Gaylord [60, 87].

In preparing the samples for Maker fringe analysis, great care was taken to insure the minimum amount of pyroelectrically induced static charge remained on the surface of the plate. Electrostatic discharging of the samples was performed by rinsing in room-temperature water. This precaution was necessary since pyroelectric charging would easily produce electric fields of several kilovolts per millimeter which would in turn be revealed in the Maker fringes [45]. Accordingly, one should note that the background area (not subjected to domain reversal) of the sample illustrated in Figure 22(c) solved to an average value of $E_{app} = 0.3 \text{ kV mm}^{-1}$ with a standard deviation of 0.2 kV mm^{-1} where these statistics were computed over the 147 points making up the grid. It was quite possible that remnant static charge contributed to this residual E_{app} . The average value of E_{app} over the six grid points comprising the poled area was -5.1 kV mm^{-1} with a standard deviation of 1.1 kV mm^{-1} . The Maker fringe data sets collected where the pump swept through the domain wall defining the boundary between the reversed and background regions were discarded since these fringe patterns would suffer spurious phase reversals and extra fringes. Subtracting all values for E_{app} within the poled region from all values of the E_{app} within the background area yielded an average value of -5.4 kV mm^{-1} with a standard deviation of 1.1 kV mm^{-1} . This result is close to the figure of $-6.9 \pm 0.2 \text{ kV mm}^{-1}$ measured from the asymmetric coercive field associated with the electric-field nevertheless falls outside the estimated overall uncertainty by roughly 0.5 kV mm^{-1} . The negative sense of E_{app} was consistent with the sense of the crystallographic axes and the sign of the electro-optic coefficients.

In an effort to reconcile this discrepancy between the magnitudes of the direct measurement of E_{app} via the asymmetry of the coercive field and value computed from the SHG data, a set of experiments were performed to measure the dc unclamped values for r_{13} and r_{33} using Maker fringe data. These results were then used to recompute the map of E_{app} . Since the Maker fringes depend critically on the differences between indices of refraction at the pump and SHG wavelengths, errors introduced by the necessary extrapolation of the 1064-nm values for r_{13} and r_{33} , as mentioned in the preceding text, could have introduced associated errors in the computation of E_{app} . For these Maker fringe measurements, liquid electrodes gated with thin glass cover slips were applied to the $\pm z$ -faces of the sample. This permitted application of a dc bias field along the z-axis while Maker fringe scans were simultaneously performed [45]. Three sets of data were collected on the sample. The first baseline set was recorded

Table IV. Electro-optic Coefficients of LiNbO₃ Expressed in mm⁻¹ kV × 10⁻⁵ Computed using Maker Fringe Analysis*

Wavelength = 1064 nm		Wavelength = 532 nm	
$r_{13} = 1.16 \pm 0.11$	$r_{33} = 3.28 \pm 0.16$	$r_{13} = 1.27 \pm 0.13$	$r_{33} = 3.43 \pm 0.07$

*The results given represent the average over the several nearly degenerate simulations for the ± 5 kV mm⁻¹ applied fields. The uncertainty listed is \pm the standard deviation for each case.

with the electrodes shorted together, the second set was recorded with $+5$ kV mm⁻¹ applied across the sample, and the third was recorded with -5 kV mm⁻¹ applied across the sample. Thickness data were computed using the baseline set. The thickness data were then used as input to compute values for r_{13} and r_{33} and the results were averaged. Checking the fringe shift at intermediate voltages at steps of 1 kV mm⁻¹ insured that the sample remained in the linear, and not quadratic, electro-optic regime. The computed results are given in Table IV and are noticeably larger than the values of Mendez et al. listed in Table III.

With these new values for r_{13} and r_{33} , the average value of E_{app} calculated for the background region was 0.0 ± 1.0 kV mm⁻¹ and the average value calculated for the poled region was -5.4 ± 1.3 kV mm⁻¹. The average value of the difference of E_{app} between the poled region and the background region was -5.4 ± 1.3 kV mm⁻¹. Here again, the uncertainty on these quantities is \pm the standard deviation for each case. The results show that whether or not one considers the tabulated or directly measured r coefficients, it is not possible to completely reconcile the asymmetry in the coercive field under room-temperature poling conditions. This discrepancy is not altogether unexpected since Wang et al. have shown that the parallel and antiparallel coercive fields change with respect to the time between domain reversals [88]. This change is rapid on a time scale of a few minutes. Therefore, since several hours were typically required to prepare the various samples for poling studies and Maker fringe analysis, a probable explanation for the observed discrepancy of roughly 0.5 kV mm⁻¹ in this inherent time evolution of the coercive fields. Additionally, a residual depolarizing field due to the presence of surface layers may also contribute to this uncertainty [88].

4.2.4. The Origin and Characteristics of Internal Fields

As evident from Figure 21, the large internal fields inside the LiNbO₃ and LiTaO₃ crystals tend to disappear as the lithium stoichiometry changes from congruent to stoichiometric crystal compositions, suggesting that the origin of internal fields lies in lithium deficiency.

For visualization, one can think of E_{int} as a built-in field which in the virgin crystal tends to point along the direction of spontaneous polarization, P_s . When the polarization is reversed using forward poling at room temperature, the internal field continues to point in the original direction. However, this is a frustrated state which continues to exist for many months, and perhaps longer. However, a high temperature anneal of this frustrated crystal state results in the reorientation of the internal field parallel to the new polarization direction. The time-temperature dependence of this reorientation process is shown in Figure 23 as a function of anneal time, and in Figure 24(a) as a function of anneal temperature for

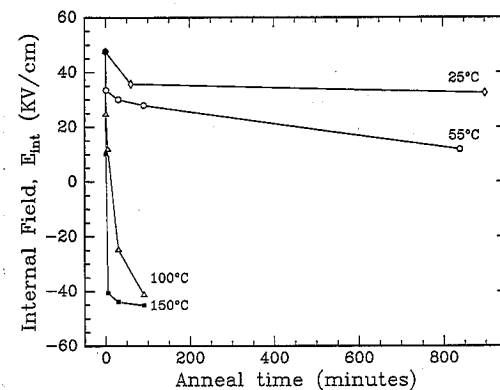


Fig. 23. The reorientation of the internal field as a function of anneal time in congruent LiTaO₃ in frustrated state (state II in Fig. 20). Reprinted with permission from V. Gopalan and M. Gupta, *Appl. Phys. Lett.*, 68, 888, (© 1996 American Institute of Physics).

congruent LiTaO₃. The temperature dependence for congruent LiNbO₃ is shown in Figure 24(b). It must be noted that these plots show the measurement of internal field at room temperature after an anneal at a high temperature followed by cooling down to room temperature. While the reorientation process is incomplete over many months at room temperature, this process takes less than 30 s above 200°C. In particular, the temperature regime of 150–200°C in LiTaO₃ and 100–150°C in LiNbO₃ are of interest because of a rapid acceleration of the reorientation of internal field in this regime as seen in Figure 24. It is interesting to note that many properties of LiNbO₃ show an anomalous behavior in the temperature range of 100–200°C, since many crystal properties such as crystal conductivity [89] the lattice parameters in close-packed oxygen planes [90] thermal expansion coefficient [91, 92] scattering efficiencies and linewidths of Raman modes [93] and the frequency of nuclear quadrupole moment of the transition atom [94] show an anomalous change in this temperature range indicating structural changes. In holographic data storage, annealing in this temperature range is done to thermally fix holograms [95]. This was shown to arise from the movement of hydrogen in the crystal with an activation energy of ~ 1.08 eV [96]. It is also known that the ionic conductivity increases exponentially above 200°C with an activation energy of ~ 0.7 eV [97]. This fact is used in forming waveguides at temperatures above 200°C by diffusing hydrogen inside the crystal by replacing lithium ions, in a process called the proton exchange [98].

These observations lead to the idea that a combination of lithium deficiency and the presence of hydrogen in the crystal may be responsible for the origin of internal fields. Hydrogen typically

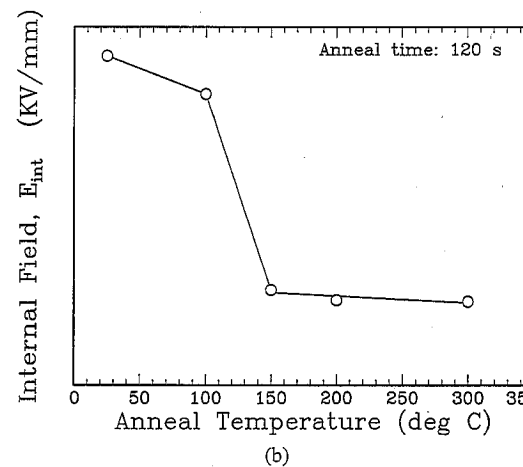
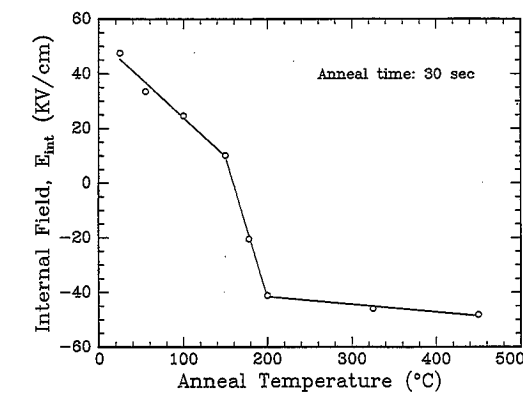


Fig. 24. The reorientation of internal field as a function of anneal temperature in (a) congruent LiTaO₃ reprinted with permission from V. Gopalan and M. C. Gupta, *Appl. Phys. Lett.*, 68, 888, (© 1996 American Institute of Physics) and (b) LiNbO₃, both in frustrated state (state II in Fig. 20). Reprinted with permission from V. Gopalan and M. Gupta, *Ferroelectrics*, 198, 49, (© 1997 Overseas Publishers Association).

gets incorporated into these crystals from atmosphere during crystal growth at higher temperatures, and gives rise to a characteristic OH⁻ absorption band in the infrared. A very strong correlation between changes in the shape of this absorption band and that of internal field with time and temperature was shown. Figure 25 shows the absorption spectrum of OH⁻ at room temperature in a virgin LiTaO₃ crystal of congruent composition before and after forward domain reversal. The spectrum can be deconvoluted into three main components, labeled A, B, and C as shown by the solid lines in the figure. Domain reversal interchanges the relative peak intensities of peaks A and C, while keeping the intensity of peak B the same. These three bands were suggested to correspond to three different O—O bond lengths in the crystal structure of LiNbO₃ and LiTaO₃ crystals [80]. The spectrum in Figure 25(b) corresponds to the frustrated internal field state of the crystal. Annealing this crystal at higher temperature restores the original spectrum shape as shown in Figure 26. The time for this recovery at 100°C is ~ 1.5 h, which is the same as that for internal field reorientation shown in Figure 23. A similar correlation is seen in congruent LiNbO₃ as shown in Figure 27.

Despite this strong correlation between hydrogen and internal fields, it is shown that hydrogen is not directly responsible for

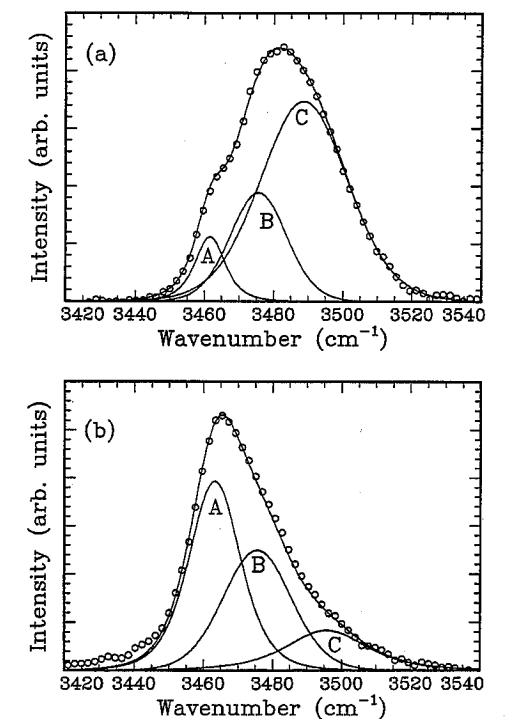


Fig. 25. The infrared absorption spectrum for OH⁻ in z-cut LiTaO₃ at room temperature for (a) virgin crystal, and (b) domain-reversed crystal at room temperature. The circles are experimental points and the solid lines are fits based on the three-band model. Reprinted with permission from V. Gopalan and M. C. Gupta, *J. Appl. Phys.*, 80, 6099, (© 1996 American Institute of Physics).

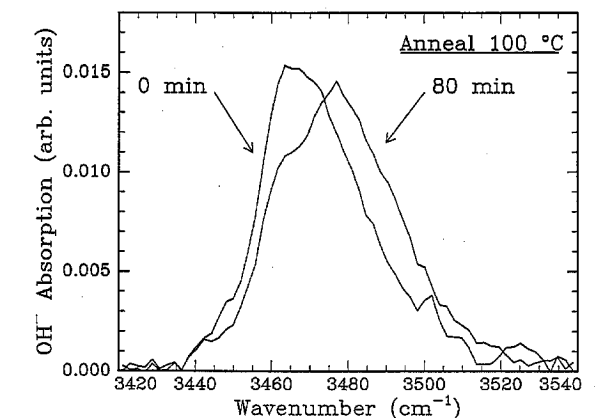


Fig. 26. The time evolution of infrared spectrum of OH⁻ in a z-cut LiTaO₃ crystal after domain reversal at room temperature followed by annealing at 100°C. The spectrum reaches a steady-state value after ~ 80 min.

the internal fields in LiNbO₃. Gopalan et al. [77] studied the effect of hydrogen content on the coercive and internal fields in LiNbO₃ crystals as a function of lithium stoichiometry, and found that changing the hydrogen content incorporated during crystal growth does not influence the domain reversal fields or the internal fields. In essence, Figure 21(a) was found to be insensitive to the integrated intensity of OH⁻ absorption peak in the LiNbO₃ crystals. Therefore, the origin of internal fields in LiNbO₃ is entirely due to the lithium deficiency in the crystal. Though a similar study on the influence of hydrogen content on domain reversal

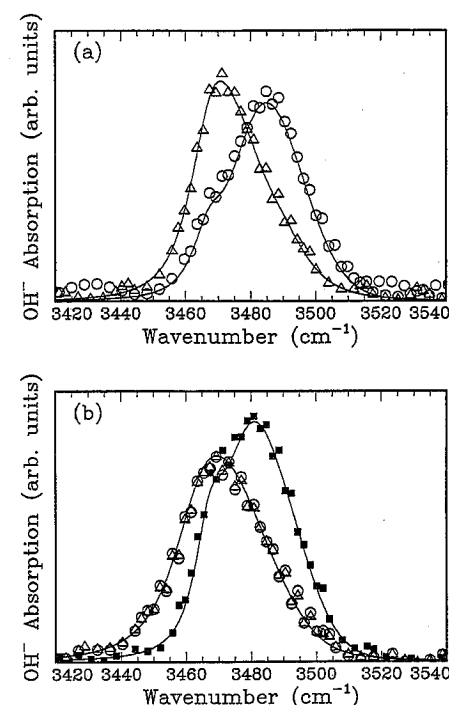


Fig. 27. (a) Infrared absorption spectrum of OH^- in virgin (circles) and domain reversed (triangles) LiNbO_3 crystal at room temperature. (b) Infrared absorption spectrum of OH^- ions of virgin (open circles) and domain-reversed (triangles) LiNbO_3 crystals at 250°C. Also shown is the spectra of domain-reversed crystal after cool down to room temperature (filled squares). Reprinted with permission from V. Gopalan and M. Gupta, *Ferroelectrics*, 198, 49, (© 1997 Overseas Publisher Association).

in congruent LiTaO_3 was not carried out, by analogy, it would appear that a similar trend would be expected. In this light, it appears that the changes in the absorption spectra may be due to the fact that hydrogen preferentially associates with the nonstoichiometric point defects or complexes responsible for the internal fields. It is known that the shape of the OH^- spectrum also changes with nonstoichiometry (Li/Nb ratio) in LiNbO_3 [99]. Specifically, as Li/Nb approaches 1 in LiNbO_3 crystals, the lowest wave-number band ($\sim 3470 \text{ cm}^{-1}$) of the OH^- spectra increases in intensity. For nearly stoichiometric crystals of LiNbO_3 , only one sharp peak at the lowest wave number (3466 cm^{-1}) remains [100]. This suggests that, as the point defects due to nonstoichiometry increase, the OH^- occupancy of two additional bands at higher wave numbers increases, and are therefore specifically associated with nonstoichiometric point defects in the crystal. The changes in the OH^- spectra simply reflect the changes in the environment around the nonstoichiometric point defects which are primarily responsible for internal fields. Nuclear magnetic resonance (NMR) studies on congruent LiNbO_3 [101] established that the hydrogen occupies only the longest O—O bond (of 3.36 \AA) in the oxygen triangle closest to the lithium site, and replaces the corresponding lithium ion. The presence of multiple bands in the OH^- spectrum appears to be related to lithium nonstoichiometry and therefore to different environments surrounding the lithium site.

The foregoing discussion raises the question as to what the exact nature of nonstoichiometric point defects or defect complexes are that give rise to internal fields? In congruent composition of LiNbO_3 , Prokhorov and Kuzminov [8] concluded that

lithium vacancies (V_{Li}^+) and oxygen vacancies (V_{O}^{2+}) dominate at room temperature, corresponding to a congruent defect structure of $[\text{Li}_{0.944}\square_{0.056}\text{Nb}[\text{O}_{2.972}\square_{0.028}]]$ for model I. However, the density of LiNbO_3 increases with increasing lithium deficiency which is incompatible with the oxygen vacancy model [102]. Schirmer et al. concluded that niobium antisites ($\text{Nb}_{\text{Li}}^{4+}$) and niobium vacancies (V_{Nb}^{5-}) are the dominant point defects and that oxygen vacancy is present at most in negligible concentrations, except when brute force treatments such as high energy electron irradiation are applied [103]. The chemical formula for this defect model suggested by Abrahams and Marsh [20] is $[\text{Li}_{0.947}\text{Nb}_{0.053}][\text{Nb}_{0.9528}\square_{0.047}\text{O}_3]$, to be referred as model II. However, Donnerberg et al. [104] showed that the formation of a niobium vacancy was found to be energetically unfavorable as compared to the formation of a lithium vacancy. The third proposed defect model (model III) is the presence of niobium antisites ($\text{Nb}_{\text{Li}}^{4+}$) and lithium vacancies (V_{Li}^-) [105]. The neutron diffraction studies by Iyi et al. [106] and Zotov et al. [107] supports this defect model with a chemical formula of $[\text{Li}_{0.95}\square_{0.04}\text{Nb}_{0.01}]\text{NbO}_3$. Schirmer et al. [103] point out that the niobium vacancy model and the lithium vacancy model can be reconciled if it is assumed that there are ilmenite type stacking faults in the regular LiNbO_3 crystal structure. For example, Figure 28 depicts the cation order in a stoichiometric, congruent, and ilmenite type structure. On comparison, one notes that a lithium vacancy in an ilmenite structure is equivalent to a niobium vacancy in the antisite defect model. Donnerberg et al. [104] show that the energetics of an ilmenite structure is only slightly less stable than the LiNbO_3 structure, and is therefore quite likely. Figure 28 also schematically depicts a plausible defect model based on model II, and the probable domain-inversion process following from this model. Using the original LiNbO_3 stacking sequence as the reference, and starting from a $(V_{\text{Nb}} - \text{Nb}_{\text{Li}})$ defect dipole, a domain-inversion process results in the movement of the lithium ions to the neighboring vacant octahedra. However, assuming that upon domain inversion at room temperature, the niobium at the Nb_{Li} does not move into the neighboring octahedra, the domain reversal results in the conversion of $\text{Nb}_{\text{Li}} \Rightarrow \text{Nb}\square$ and the creation of a V_{Li} . This would correspond to the frustrated state of the internal field. However, upon thermal activation, the $\text{Nb}\square$ and the adjacent V_{Nb} can annihilate each other. Upon cooling down, the V_{Li} and the adjoining Nb interchange to give rise to a $(\text{Nb}_{\text{Li}} - V_{\text{Nb}})$ dipole. The process of domain reversal at room temperature followed by a high temperature anneal, and cooling down to room temperature, therefore results in the reorientation of a defect dipole from $(V_{\text{Nb}} - \text{Nb}_{\text{Li}})$ to a $(\text{Nb}_{\text{Li}} - V_{\text{Nb}})$, and a corresponding reorientation of the internal field parallel to the new polarization direction.

However, a very different suggestion has come from Ivanova and Yatsenko et al. [108, 109] who interpreted the nuclear magnetic resonance (NMR) spectra in congruent LiNbO_3 . They conclude that at room temperature, a combination of models I and III in a ratio of 1.1:1.0 would provide a "rather good qualitative and quantitative agreement with the NMR ^7Li spectra." However, the authors assert that only the model III (with allowance for mobility of Li^+ ions in LiO_6 octahedra) can explain the temperature dependence of the experimental NMR ^7Li and ^{93}Nb spectra from 77 to 4.2 K. Accordingly, the authors propose the structure of defect complex as comprising of a niobium antisite surrounded by three Li^+ vacancies in the nearest neighborhood, plus one independent Li^+ vacancy along the polar z-direction. Yatsenko [110]

(a)	(b)	(c)	(d)	(e)	(f)	(g)	(h)
Nb	Nb	Nb	Nb	Nb	Nb	Nb	Li
Li	Li	Li					
Li	Nb	Nb	Li	Li	Li	Li	Li
Nb	Li	Li	Nb	Nb	Nb	Nb	Nb
Nb	Nb	Nb	Li	Li	Li	Li	Nb
Li	Li	Li	Nb	Nb	Nb	Nb	Li
Li	Nb	Nb	Li	Li	Li	Li	Li
Nb	Li	Li	Nb	Nb	Nb	Nb	Nb
Nb	Nb	Nb	Li	Li	Li	Li	Nb
Li	Li	Li	Nb	Nb	Nb	Nb	Li
Li	Nb	Nb	Li	Li	Li	Li	Li
Nb	Li	Li	Nb	Nb	Nb	Nb	Nb

Fig. 28. Schematics of a $V_{\text{Nb}} - \text{Nb}_{\text{Li}}$ based point defect complex model in congruent LiNbO_3 .

also reported that the preliminary analysis of the structural distortions caused by a Nb_{Li} antisite defect reveal a contraction of the nearest three oxygen atoms, and a displacement from the c-axis of the nearest three ^{93}Nb nuclei. This defect complex comprising of one Nb_{Li} with four V_{Li} certainly possesses an electrical dipole moment (arising primarily along the z-axis from the independent V_{Li} and Nb_{Li}), and could be the source of internal field. This defect model is also supported by X-ray and neutron diffuse scattering of congruent LiNbO_3 by Zhdanov et al. [111], Ivanov et al. [112] and by Zotov et al. [113]. These studies conclude that the diffuse lines in scattering arise from a one-dimensional displacive and substitutional disorder in the three pseudo-cubic directions along the Li—O—Li... chains. These directions correspond to pseudo-cubic directions $[2\bar{4}.1]$, $[2\bar{2}.1]$, and $[4\bar{2}.1]$ (in orthohexagonal notation) which are related to each other by the threefold symmetry axis (polarization c-axis) and are inclined at 52° to the c-axis. Diffuse maxima around the Bragg positions reflect some three-dimensional short-range order of the defect elements and the homogeneous part of the diffuse planes reflect random distribution of the defect clusters. Since each niobium antisite requires four lithium vacancies in the neighborhood, Zotov et al. [113] suggest possible chains such as $\text{Li-Nb}_{\text{Li}}-\square-\text{Li}$, $\text{Li}-\square-\text{Nb}_{\text{Li}}-\square$, $\text{Li}-\square-\square-\text{Nb}_{\text{Li}}$, etc. as possible combinations. Since these three-dimension defect clusters also should possess a dipole moment, Figure 29 shows a possible schematic of the equilibrium states of defect complex for an up and a down domain. Upon domain reversal, one can see that lithium ions needs to rearrange to reach stable defect equilibrium states from (a) to (b). At room temperature, lack of lithium mobility can result in the frustrated state of defect complex in (a), which can be relieved into state (b) after a high temperature anneal. However, as pointed out by Nassau and Lines [114] the presence of two niobium ions in adjacent oxygen octahedra can be energetically unfavorable due to dense positive charge around the cluster. They propose extended stacking fault defects in the structure. Zotov et al. [113] however restrict restrict the size of such clusters to $\sim 11.4 \text{ \AA}$, (about four cation sites) to match the correlation length $L_c \sim 13 \text{ \AA}$ along the chains calculated from the FWHM of the diffuse streaks in X-ray. The average spacing between defect clusters along the chains is estimated to be $\sim 76 \text{ \AA}$. The temperature dependence of diffuse X-ray streaks [113] suggest that at low temperatures, the lateral correlations between defect clus-

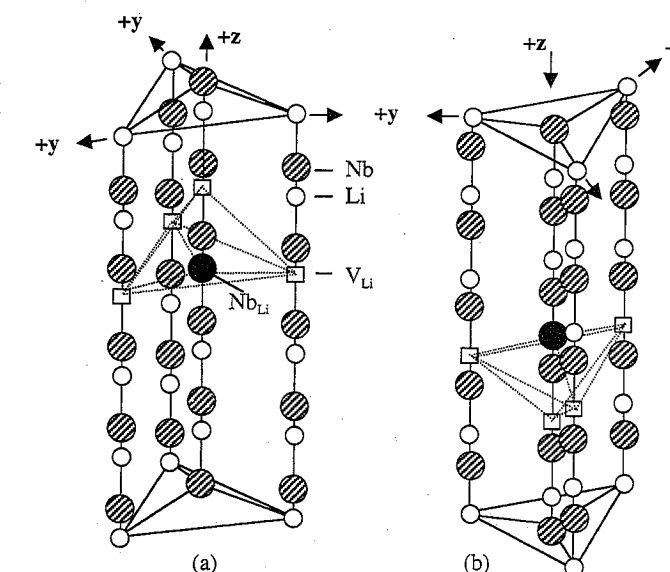


Fig. 29. Schematic of a possible defect complex involving Nb_{Li} and V_{Li} in (a) an up domain and (b) a down domain.

ters become quite substantial. With increasing temperature, these correlations decrease, resulting in more random one-dimensional disorder. The changes in the coercive and internal fields with temperature as discussed next also suggests the breaking up of the three-dimensional clusters with heating.

4.2.5. The Temperature Dependence of Domain Switching

Electric-field poling of as-grown crystals is performed near the Curie temperature ($\sim 610^\circ\text{C}$ for congruent LiTaO_3) [115]. Domain-reversal studies in LiTaO_3 in the range of $200\text{--}600^\circ$ was performed by Ballman and Brown [116]. Figure 30 shows the coercive field measurements versus temperature for congruent LiTaO_3 from the study of Ballman [116]. The study predicted an extrapolated domain reversal field of 5 MV mm^{-1} in congruent LiTaO_3 at room temperature which is 2 orders of magnitude higher than the actual value ($\sim 21 \text{ kV mm}^{-1}$). The temperature range of $150\text{--}200^\circ\text{C}$ is therefore particularly interesting, as also seen from Figure 24.

Battle et al. [117] measured the switching fields and internal fields in the temperature range of 25–250°C in congruent LiTaO₃. Their results are discussed in detail here.

The starting material was a single crystal single domain z-cut congruent LiTaO₃ referred to as virgin crystals. Metal films of ~3000 Å tantalum were deposited on the z-- and z+-surfaces of the crystal using dc magnetron sputtering. The sample was clamped between two brass fixtures used as electrodes. Starting from the virgin crystal, the first domain reversal is referred to as forward poling (subscript f) and the second reversal back to original state as reverse poling (subscript r). The transient currents measured in the external circuit are shown in Figure 31 for forward and reverse poling as a function of temperature. All the studies were performed on 0.48-mm-thick z-cut crystal pieces cut from the same wafer. A new piece of virgin crystal from the same wafer was used for each independent temperature study, and then cycled through one forward and one reverse poling as shown in Figure 31(a) and (b), respectively. The applied voltage was ramped at 50 V s⁻¹, with a delay of ~10 s between forward and reverse poling sequences. The following observations were made:

(a) The "peak" electric fields, E_f -peak and E_r -peak are defined as the field values corresponding to the main (higher current) peak of the transient current in the forward and reverse poling, respectively, as shown in Figure 31. Figure 32 shows that the E_f -peak decreases monotonically by a factor of ~2.4 from room temperature (RT=22.2°C) to 250°C, with accelerated decrease above 150°C. The E_r -peak however shows a slight increase of ~15% from RT to 150°C, followed by a decrease to approximately the same value as the E_f -peak at 250°C. Using these peak values, if the internal field E_{int} is defined as $E_{int} = (E_f - E_r)/2$, then the internal field decreases from 5.4 kV mm⁻¹ at RT to ~0 kV mm⁻¹ at 250°C.

(b) Figure 32 also shows the variation of the "start" and "end" electric-field values for the transient currents observed in Figure 31 during forward (E_f) and reverse (E_r) poling. The start field value for domain reversal is defined as the field at which the transient current shows a deviation from the initial linear slope of the current-voltage curve. Crystal conductivity increases with temperature as reflected in the increasing slope of the baseline for the

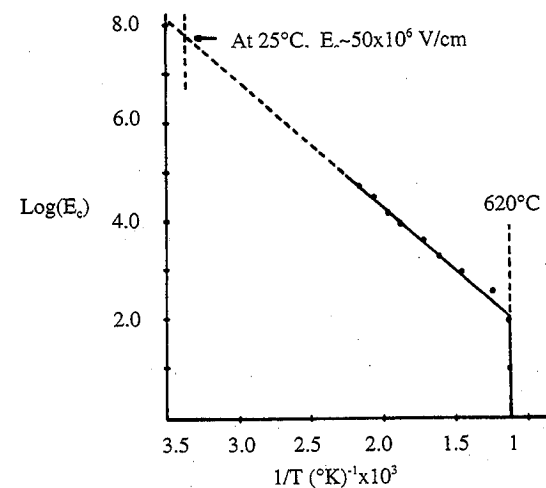


Fig. 30. Coercive field versus temperature for congruent LiTaO₃. Reprinted with permission from A. A. Ballman and H. Brown, *Ferroelectrics*, 4, 189, (© 1978 Overseas Publisher Association).

transient currents versus voltage. The initial slope of the current (i)-voltage (V) plot in Figure 31 is directly proportional to the dc-crystal conductivity, σ , given by $\sigma = id/AV$, where d is the crystal thickness and A is the area of the electrode. The crystal conductivity increases exponentially with temperature as shown in Figure 32, with an activation energy of 0.66 ± 0.14 eV as indicated by the solid line fit which is similar to previous reports [118] of activation energy of 0.72 eV for conductivity in LiNbO₃. The end of the transient peak is defined as the voltage where the falling edge of the transient current peak starts increasing again with voltage. These definitions, though somewhat arbitrary (possible errors of up to $\pm 10\%$), nonetheless give the approximate range of electric fields over which the transient current peak is observed. This shoulder peak width information is also included in the overall width as defined by the difference between the end and the start field values. The overall peak width increases monotonically for forward do-

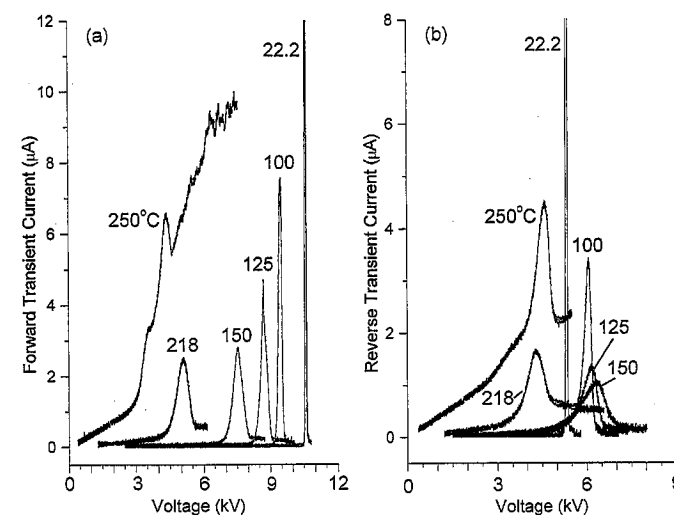


Fig. 31. Transient current during domain reversal as a function of temperature for congruent LiTaO₃. Reprinted with permission from C. C. Battle et al., *Appl. Phys. Lett.*, (© American Institute of Physics, submitted for publication).

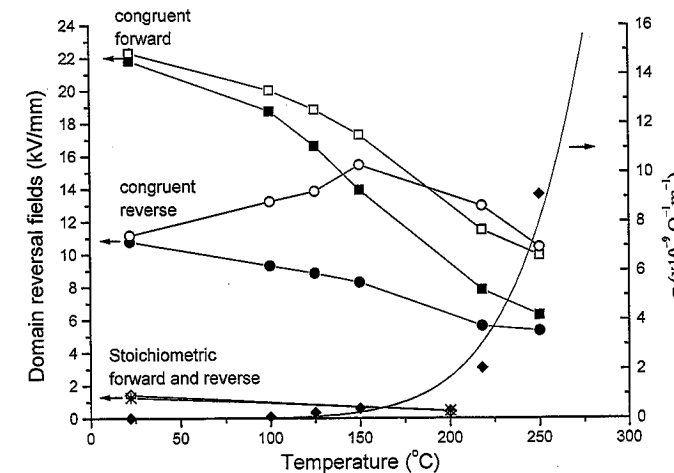


Fig. 32. The plot of coercive field and dc conductivity as a function of temperature for congruent and stoichiometric LiTaO₃. Reprinted with permission from C. C. Battle et al., *Appl. Phys. Lett.*, (© American Institute of Physics, submitted for publication).

main reversal from ~0.5 kV mm⁻¹ at RT to ~3.8 kV mm⁻¹ at 250°C. In the reverse domain reversal, this width increases from ~0.5 kV mm⁻¹ at RT to a maximum of ~7.2 kV mm⁻¹ at 150°C, followed by a decrease to ~5 kV mm⁻¹. Within error bars (of $\pm 10\%$), the range of electric fields over which domain inversion takes place is approximately the same for forward and reverse poling at 250°C. Figure 33 shows a series of optical micrographs of domain nucleation with partial reversal of domains at various temperatures. The domain nucleation rate increases and the growth rate shows a decrease with temperature. With increasing temperature, the domain switching process changes from growth dominated to nucleation dominated regimes. Evlanova reports [119] the temperature dependence of domain switching in LiNbO₃ that suggests that a similar influence of the temperature on domain reversal in congruent LiNbO₃ is to be expected. While the coercive field for domain reversal in congruent LiNbO₃ is ~21 kV mm⁻¹ it is reported to be 8 kV mm⁻¹ at 130°C, and only 6 kV mm⁻¹ at 170°C [119].

Considering a single domain, a single crystal of congruent LiTaO₃ is cooled from high temperatures. At 250°C, the domain-reversal field required to reverse this domain once (forward) and then back (reverse) are similar as seen in Figure 32. As the crystal is cooled further, the threshold field for the forward reversal of this single domain crystal shows a marked increase between 150–200°C. This is the same regime where the crystal conductivity shows an exponential change. It is known that the mobility of lithium site ions (such as hydrogen doping) and vacancies in the crystal shows a sharp increase when heated above 150°C, [120] and that reorientation of frustrated internal fields at room temperature is achieved by heating the crystal above 150°C as seen in Figure 23. It is also known that internal fields in congruent crystals arise directly from lithium nonstoichiometric point defect complexes [78]. Therefore, it seems plausible that the sharp rise upon

cooling in the threshold field for domain reversal in the 150–200°C regime in Figure 32 is due to the point defect complexes resulting from lithium nonstoichiometry; these point defects increasingly lack mobility in the crystal lattice below 150°C, and form frozen polar defect complexes which are preferentially oriented to stabilize the lattice polarization P_s , thus increasing the threshold field for domain reversal. Possible defect complexes can comprise of ($V_{Li} - Ta_{Li}^{4+}$) or ($V_{Ta}^{5+} - Ta_{Li}^{4+}$) as discussed previously. This argument therefore suggests that in stoichiometric crystals of LiTaO₃ with no lithium deficiency, such an anomalous increase in domain-reversal fields will not take place upon cooling from 250°C to RT. This is confirmed by the second set of data shown in Figure 32 for stoichiometric LiTaO₃. The second observation is that the range of electric fields over which domain inversion takes place decreases by an order of magnitude with cooling from 250°C to room temperature. This also appears to be closely connected to the issue of mobility of ionic defects related to lithium nonstoichiometry. The appearance of a shoulder peak in the transient current at 250°C is suggestive of a possible field driven modification of the polar defect complexes, which appears to inject extra charge in the transient current peaks. This is deduced by integrating the charge under the curve (excluding baseline) which yields a charge q^* that is 50–500% greater than the expected value of $q = 2P_s A$ where A is the electrode area [117]. With a decrease in temperature, and a decrease in the mobility and consequently the reorientation ability of these polar defects under electric fields, this extra peak in the transient current diminishes, and the range of electric fields over which transient currents are seen, also decreases with temperature. The foregoing arguments emphasize the critical role of lithium nonstoichiometry related point defects in domain reversal in LiTaO₃.

4.3. Domain Wall Structure

The visualization of 180° domains in LiNbO₃ and LiTaO₃ was predominantly done using chemical etching of the crystal surfaces [121]. For a detailed review of the etching studies, see Prokhorov and Kuzminov [8]. The most commonly used etchant is a mixture of HF:HNO₃:1:2 and heated to temperatures up to ~90°C. The etching of a z-cut single crystal results in a more pronounced etching of the z-surface of a domain as compared to the z+-surface. The y+- and the y--faces also etch differently, allowing domains to be observed in the crystal cross-section. Nondestructive observation of domains in these materials was not used extensively. In uniaxial ferroelectric crystals, the optical indicatrix is invariant under domain reversal, and hence antiparallel 180° domains cannot be normally imaged. However, in real materials with defects, these domains often show optical contrast.

4.3.1. Optical Contrast and Electric Fields at a Domain Wall in Congruent Crystals

Evlanova [119] reported the presence of optical birefringence near 180° domain walls in LiNbO₃. Gopalan et al. [80] reported that domain walls in LiTaO₃ show both scattering and optical birefringence, and can be viewed by an optical microscope in both polarized and unpolarized light. Figure 34 shows 180° domains in z-cut LiTaO₃ crystals of congruent composition at room temperature. The domains were created by applying electric field at room temperature. The pictures were taken in unpolarized transmitted light through the crystal (Fig. 34(b)) and between cross-polarizers (Fig. 34(a)). The dark contrast at the domain walls is due to the

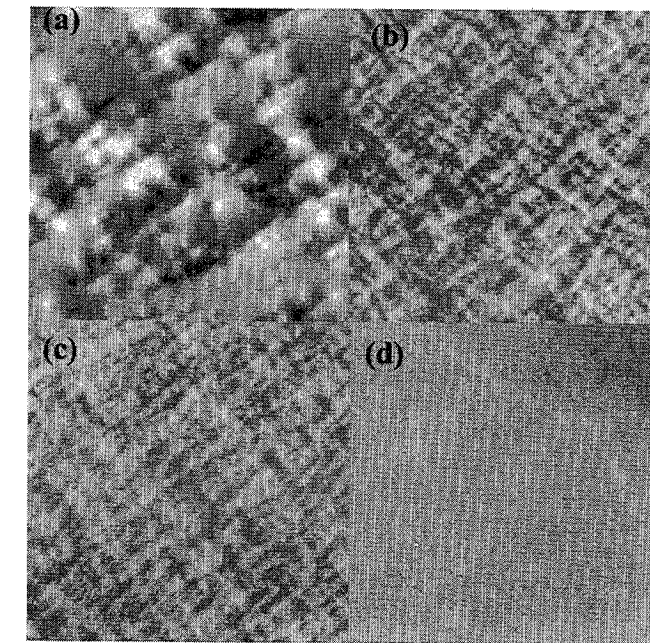


Fig. 33. Optical micrographs showing the nucleation and growth of ferroelectric domains in congruent LiTaO₃ at different temperatures. Reprinted with permission from C. C. Battle et al., *Appl. Phys. Lett.*, (© American Institute of Physics, 76, 2436 (2008)).

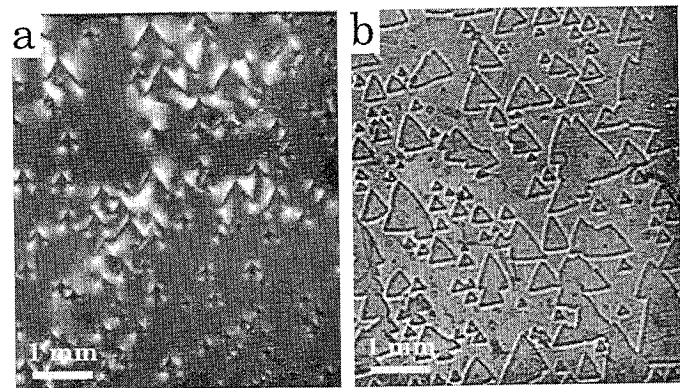


Fig. 34. Antiparallel domains in congruent LiTaO₃ at room temperature imaged (a) between cross-polarizers, and (b) in unpolarized transmitted light in an optical microscope.

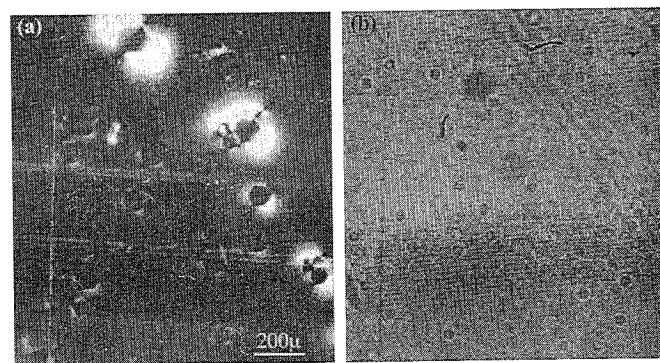


Fig. 35. Antiparallel domains in congruent LiNbO₃ and LiTaO₃ at room temperature imaged (a) between cross-polarizers, and (b) in unpolarized transmitted light in an optical microscope.

Fresnel fringe contrast arising from the scattering of light at the walls. This indicates a change in the refractive index at the walls, as compared to the bulk of the crystal. Figure 34(a) shows the same domains between cross-polarizers in an optical microscope. Light appears to leak through only near the domain walls. By relative rotation of the crystals with respect to the polarizer and analyzer, one can determine that when a domain wall is parallel to either the polarizer or the analyzer, its contrast disappears. This suggests that there is an optical birefringence at the domain walls, where the refractive index in the z -plane along a domain wall is different from the index perpendicular to the wall. The same results are observed in domains created at room temperature in congruent LiNbO₃ crystals as shown in Figure 35(a) and (b). However, the domain shape is six-sided in congruent LiNbO₃. This is schematically shown in Figure 36. In congruent LiTaO₃, the domain walls are perpendicular to the crystallographic y -axis ($y \equiv [01\bar{1}0]$ in hexagonal coordinates) and intersect to form triangular domains. However, when the domain growth is driven at very high electric fields in congruent LiTaO₃, the domain shape evolves into hexagonal domains, with walls still perpendicular to the y -axes. In congruent LiNbO₃, the domain walls are perpendicular to the x -axes ($\langle 11\bar{2}0 \rangle$ directions). These six domain walls intersect to form six-sided polygonal domains. The birefringence, Δn , next to the domain wall is therefore, $|\Delta n| = |n_x - n_y|$. The difference in domain shapes between congruent LiNbO₃ and LiTaO₃ is discussed in detail further on.

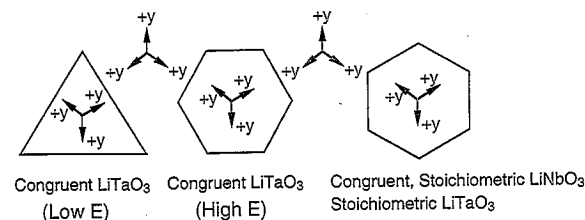


Fig. 36. Schematic of domains in LiNbO₃ and LiTaO₃.

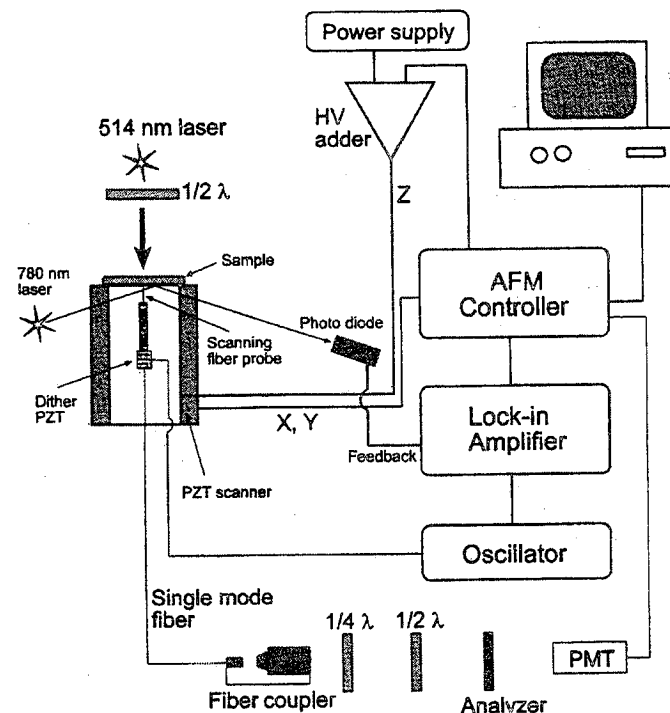


Fig. 37. Schematic of the collection mode near-field scanning optical microscopy (CMNSOM). Reprinted from T. J. Yang et al., *Ferroelectrics*, 772, 609, (© 1999 Gordon & Breach); T. J. Yang et al., *Phys. Rev. Lett.*, 82, 4106, (© 1999 American Physical Society).

Yang and Mohideen et al. [81] measured the optical birefringence at the domain walls using collection mode near-field scanning optical microscopy (CMNSOM). In the CMNSOM, polarized light transmitted through the crystal is collected using an adiabatically tapered optical fiber probe with a 50- to 60-nm aperture. This is shown schematically in Figure 37. The fiber is maintained less than 5 nm from the sample surface using a low-frequency lateral dithering coupled to a shear force feedback loop. Thus, the CMNSOM simultaneously yields nanometer scale topographic information and optical birefringence information. Figure 38(a) shows the topographic and optical birefringence image of a corner of a triangular domain in a congruent LiTaO₃ crystal. A 10-nm lateral resolution and a 0.5-nm depth resolution in the topographical image is reported. A typical maximum height change of 0.5 nm at the domain wall with the strain region extends on the average for about 500 nm. Additional scratches from the polishing step of width around 100 nm are also observed as lines in the topographic image. Figure 38(b) is the optical signal collected through the probe with the incident polarization of light at 70° to the domain wall on the top and 50° to the domain wall at the bottom.

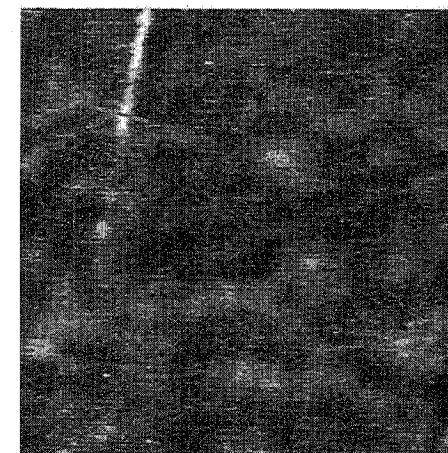


Fig. 38. A 4×4-μm CMNSOM topographic image of a vertex of triangular domains in congruent LiTaO₃. (b) The corresponding optical image, with a sample between cross-polarizers. Reprinted from *Phys. Lett. A*, 250, T. J. Yang and U. Mohideen, 205, (©1998), with permission from Elsevier Science.

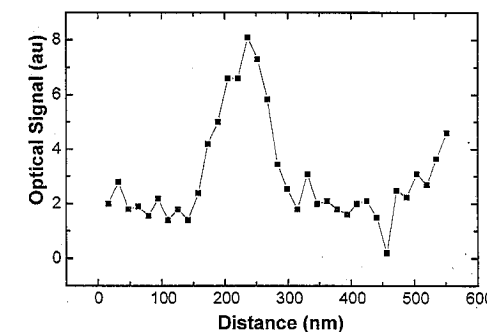


Fig. 39. The optical signal across a domain wall in Figure 38(b). Reprinted from *Phys. Lett. A*, 250, T. J. Yang and U. Mohideen, 205, (©1998), with permission from Elsevier Science.

Figure 39 shows the optical signal at the domain wall along the blue line across the top domain wall as shown. The width of the birefringent region is ~200 nm for the top wall, and ~600 nm in width for the bottom wall. The size of the smallest reproducible optical feature on repeated scans of the same region yields an estimated spatial resolution of ~80–100 nm. The measured average optical birefringence was $\Delta n = (2 - 10) \times 10^{-5}$. Similar values of birefringence were also measured for congruent LiNbO₃ crystals [122]. Other reports by the same authors also reported birefringence widths of up to 3 μm and birefringence of 1.2×10^{-4} .

The presence of optical birefringence at domain walls also indicate the presence of local strains and electric fields as well. The electro-optic effects connect the electric fields with the optical birefringence, while the elasto-optic effect relates the optical birefringence to the strains. Then

$$B_i - B_i^0 = p_{ij}\epsilon_j + r_{ik}E_k \quad (19)$$

where $B_i = \Delta(1/n_i^2)$, p_{ij} are the photoelastic constants, r_{ij} are the electro-optic constants, ϵ_i are the strains, and E_k are the electric fields. The strains are related to electric fields through the piezoelectric effect, where $\epsilon_j = d_{kj}E_k$. One can then readily show that the optical birefringence Δn in LiNbO₃ or LiTaO₃ is given by

$$\frac{\Delta n}{n^3} = \left[\left(\frac{p_{11} - p_{12}}{2} \right) + \frac{r_{22}}{2d_{22}} - p_{14} \frac{d_{24}}{2d_{22}} \right] (\epsilon_1 - \epsilon_2) \quad (20)$$

where axis 1 is parallel to the crystallographic x -axis, axis 2 is parallel to the y -axis, and 3 is along the polarization direction, z . In the triangular domains in congruent LiTaO₃, the domain wall is parallel to the axis 1. Taking bulk coefficients for the photoelastic, electro-optic, and piezoelectric coefficients, and an average measured value of $\Delta n = 6 \times 10^{-5}$, the corresponding strain $\epsilon_1 - \epsilon_2 \sim \pm 1.4 \times 10^{-4}$ which is the difference in the strains along the domain wall and normal to it. The internal electric field perpendicular to the domain wall, $E_2 = -(\epsilon_1 - \epsilon_2)/2d_{22}$ is $\pm 10 \text{ kV mm}^{-1}$. An additional shear strain $\epsilon_4 = d_{24}E_2$ exists which is $\pm 2 \times 10^{-4}$. From the topographic step change of ~0.5 nm at the domain wall over a ~0.5 mm-thick crystal, the strain ϵ_3 can be estimated as $\sim 1 \times 10^{-6}$. Using $\epsilon_3 = d_{33}E_3$, the internal electric field is estimated as $E_3 = 0.15 \text{ kV mm}^{-1}$. This value, when multiplied by the relative dielectric constant ($\kappa \sim 45$) [123] yields $\kappa E_3 \sim 6.75 \text{ kV mm}^{-1}$ which is the order of E_{int} . One would expect the value for κE_3 to equal $E_{\text{app}} \sim 2E_{\text{int}}$ as argued by Aust [45] in the case of congruent LiNbO₃ and detailed in Section 4.2.3. In congruent LiTaO₃, $2E_{\text{int}} \sim 10 \text{ kV mm}^{-1}$. The discrepancy, we believe, may arise from errors in the approximate measurement of strain ϵ_3 by CMNSOM. The other possible reason is that E_3 measured by Yang et al. [82] is at a domain wall, while the $E_{\text{app}} = 2E_{\text{int}}$ measured by Aust [45] that gives rise to Maker fringe shift reflects a homogeneous strain in the bulk of the region (away from a domain wall) where domain reversal has taken place in a virgin crystal at room temperature. Yang and Mohideen [81] also argue that at a domain wall, the $E_1 \ll E_2, E_3$ from a lack of large changes at the vertex of the triangle, since a significant E_1 would imply a large charge accumulation at the vertex proportional to $\partial E_1/\partial x_1$. If $E_1 \sim 0$, then $\epsilon_5 \sim \epsilon_6 \sim 0$. (However, it can be shown from free energy theory of domain walls in LiNbO₃ and LiTaO₃ (see Section 4.3.5), that this condition is true only for the hexagonal domains as seen in Figure 35. For the walls of the triangular domains in Figure 34, ϵ_5 is not zero, though ϵ_6 is still zero). The total

domain wall energy can therefore be estimated as

$$U = \frac{1}{2} \sum_i w^* k_i \epsilon_0 E_i^2 + \frac{1}{2} \sum_i w^* c_{ii} \epsilon_i^2 \quad (21)$$

where the first term is the electrostatic energy, and the second term is the elastic free energy. Using an average domain wall width $w^* \sim 400$ nm, the total domain wall energy estimated in congruent LiTaO_3 is $\sim 10^{-2} \text{ J m}^{-2}$.

The previous analysis (Eq. (20)) ignores the quadratic electro-optic effect and the electrostrictive effects. Taking these into consideration as well, optical birefringence $\Delta n = n_x - n_y$ is given by [82]

$$\frac{2\Delta n}{n_1^3} = \{2p_{14}d_{15} - 2d_{22}(p_{11} - p_{12}) - 2r_{22}\}E_2 + \{(p_{11} - p_{12})(\gamma_{12} - \gamma_{11}) - 2\gamma_{14}p_{14} + (K_{12} - K_{11})(E_2^2 - E_1^2) + \{4(p_{11} - p_{12})\gamma_{41} + 4p_{14}\gamma_{44} + 4K_{14}\}E_2E_3\} \quad (22)$$

where all three built-in electric-field components E_1 , E_2 , and E_3 are considered, and the relation was derived for the 3 m symmetry. The p_{ij} are the photoelastic constants, r_{ij} are linear electro-optic constants, E_k are electric fields, K_{ilm} are the quadratic electro-optic constants, and γ_{ij} are the electrostrictive constants and the strain $\epsilon_j = d_{mj}E_m + \gamma_{ij}E_iE_j$. One can verify that ignoring the K_{ilm} and γ_{ij} yields the same relation as Eq. (20). Therefore, the optical birefringence depends on both E_2 and E_3 . This relationship can be seen if in addition to the in-built electric fields, one also applies an external electric field E_3 such as that during domain reversal. Figure 40 shows the variation in the optical birefringence measured using CMNSOM as a function of externally applied electric field E_3^{applied} , where E_3 in Eq. (22) becomes $E_3 = E_3^{\text{internal}} + E_3^{\text{applied}}$, where E_3^{internal} corresponds to an ap-

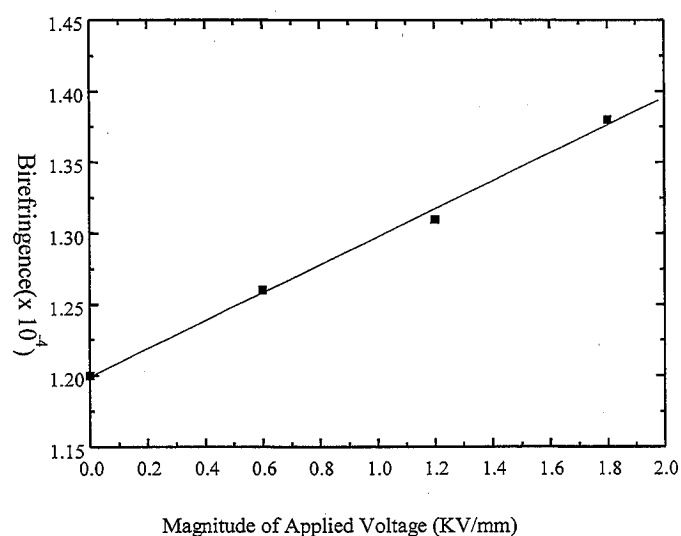


Fig. 40. Optical birefringence at a domain wall as a function of electric field. Reprinted from T. J. Yang et al., *Ferroelectrics*, 222, 609, (© 1999 Gordon & Breach); T. J. Yang et al., *Phys. Rev. Lett.*, 82, 4106 (© 1999 American Physical Society).

parent external field of $\sim 2E_{\text{int}}$. The slope of the line is given by

$$\frac{d\Delta n}{dE_3} = \frac{n_1^3 E_2}{2} \{4(p_{11} - p_{12})\gamma_{41} + 4p_{14}\gamma_{44} + 4K_{14}\}E_2 \quad (23)$$

Here the “+” sign is used as the applied field leads to an increase in birefringence (applied field in same direction as internal field) and E_2 is assumed constant as the domain wall remains fixed and $E_2 \gg E_3$ [8]. The slope in Eq. (23) was measured by Yang et al. [82] for congruent LiTaO_3 to be $\sim 10^{-11}$. The only unknown coefficient is K_{14} , which can be calculated from the slope to be $K_{14} = 2 \times 10^{-20} \text{ m}^2 \text{ V}^2$. This is in the correct range between $0.2\text{--}2 \times 10^{-20}$ for quadratic electro-optic coefficients in LiTaO_3 [122].

4.3.2. The Influence of Lithium Stoichiometry on Optical Birefringence

Figure 41(a) shows the optical microscopy image of the domains created in near-stoichiometric LiTaO_3 crystals. The optical birefringence is extremely low, and the domain walls are very hard to distinguish. Close examination of the crystal reveals a faint contrast at the domain walls. However, application of an electric field of $\sim 1.6 \text{ kV mm}^{-1}$ reveals the domain walls due to an index change Δn_{22} created at the walls through the electro-optic coefficient r_{23} as shown in Figure 41(b). A similar situation exists for near-stoichiometric LiNbO_3 crystals where the domain walls are extremely difficult to distinguish. Attempts to measure this birefringence using CMNSOM were unsuccessful, thus suggesting that the birefringence values are $< 1 \times 10^{-6}$. Thus, there is a clear correlation between the optical birefringence and lithium stoichiometry in the crystal, suggesting that the local relaxation of point-defects related to lithium nonstoichiometry near domain walls results in the creation of optical birefringence. This birefringence can be related to the presence of strains and local electric fields as discussed later.

Figure 41(c) shows domains created in stoichiometric LiTaO_3 and etched in HF acid to reveal the domains. It is clearly noted that the domain shape in stoichiometric LiTaO_3 are six-sided hexagons. In contrast, as seen in Figure 34, the domain shape is triangular in congruent LiTaO_3 . The issue of domain shape is discussed in Section 4.3.5.

4.3.3. The Influence of Temperature on Domain Wall Contrast

The optical birefringence created at room-temperature domain reversal strongly diminishes after annealing at temperatures above 200°C for a few minutes. This is shown in Figure 42 where the domain structure in LiTaO_3 is shown after annealing at 350°C for 12 h. After annealing, the sample is furnace cooled slowly and washed in water at room temperature to remove pyroelectric charges. (The case of pyroelectric charge imaging is described further on.) This directly correlates the optical birefringence with the presence of internal fields which show similar reorientation with time and temperature, and which in turn directly arise from non-stoichiometric point defects.

The contrast can be recovered by applying a sudden heat pulse to the sample (such as heating to $100\text{--}150^\circ\text{C}$ and cooling fast on a metal block in air), which creates pyroelectric charges on the surface. Figure 43 shows the recovery of the domain image upon creating pyroelectric charges. The higher the temperature gradient for heating, the larger the pyroelectric field upon cooling, and stronger the contrast of the domain wall at room temperature.

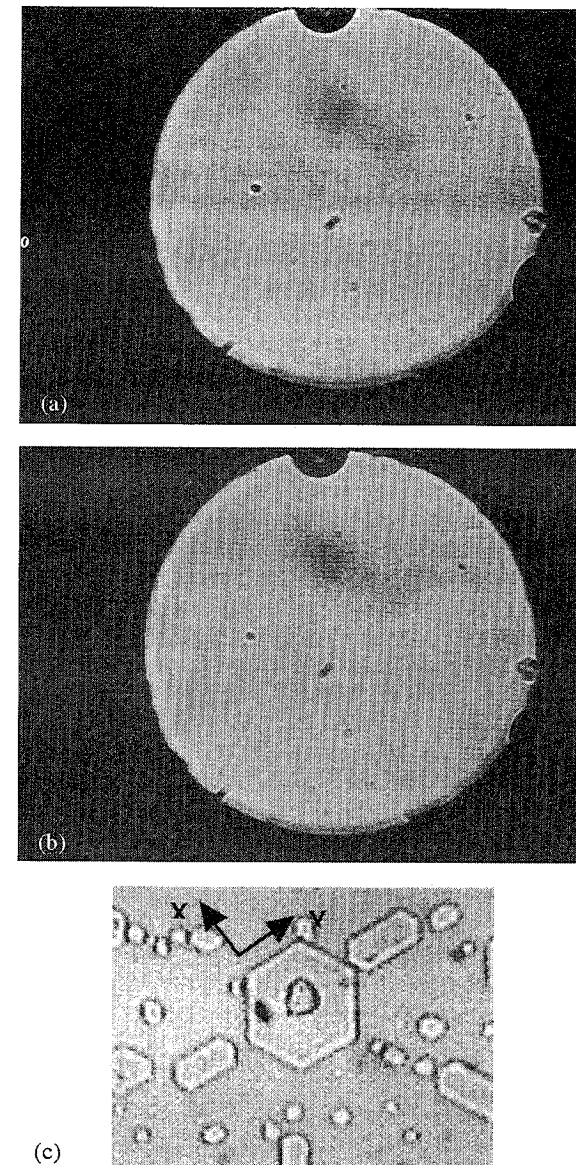


Fig. 41. The optical contrast at a domain wall in stoichiometric LiTaO_3 (a) with no-field, and (b) under an electric field of 1.6 kV mm^{-1} . (c) Domains revealed by etching in a mixture of 1:HF+2:HNO₃.

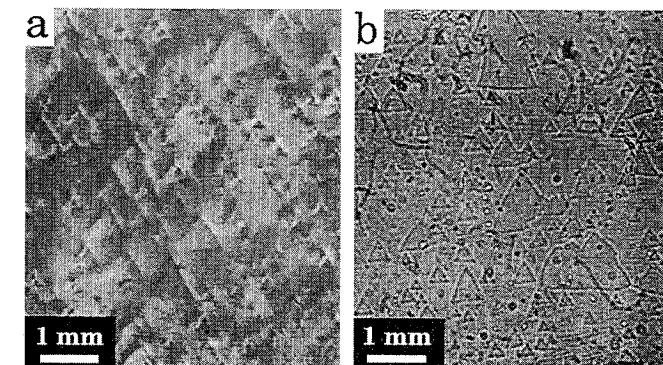


Fig. 42. Optical contrast at a domain wall after domain reversal at room temperature followed by annealing at 350°C (a) between cross-polarizers, and (b) in unpolarized transmitted light. Reprinted with permission from V. Gopalan and M. C. Gupta, *J. Appl. Phys.*, 80, 6099, (© 1996 American Institute of Physics).

However, this contrast is different from the optical birefringence shown in Figure 34(a). When observed under cross-polarizers in an optical microscope, the contrast at all the domain walls are equally strong, irrespective of their relative orientation with the input and output polarizers, indicating that scattering of light at domain walls is the origin of the contrast rather than a coherent rotation of the polarization of light by optical birefringence. When the sample is washed with water again, the pyroelectric contrast disappears as the charges are washed away.

Figure 44 shows a schematic which attempts to explain the annealing and pyroelectric imaging contrasts. Figure 44(a) shows the case of an unannealed domain-reversed crystal at room temperature. The change in the ordinary refractive index Δn_o across a domain wall is $\Delta n_o = n_o^3 r_{13} (2E)_{\text{int}} = 8.7 \times 10^{-4}$ where $E_{\text{int}} \sim 5 \text{ kV mm}^{-1}$ and $r_{13} \sim 8.4 \text{ pm V}^{-1}$ in LiTaO_3 . This would give rise to a scattering of light at the wall, thus making it visible in transmitted light. The optical birefringence, $\Delta n = n_x - n_y$ however arises from a combination of E_2 and E_3^{internal} as predicted by Eq. (22).

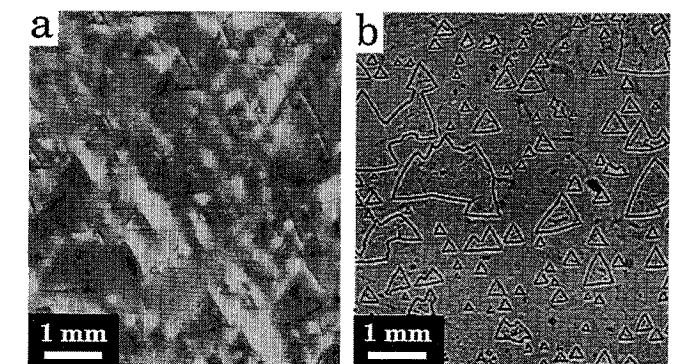


Fig. 43. Optical imaging of ferroelectric domains by the creation of a pyroelectric charge (a) between cross-polarizers, and (b) in unpolarized transmitted light. Reprinted with permission from V. Gopalan and M. C. Gupta, *J. Appl. Phys.*, 80, 6099, (© 1996 American Institute of Physics).

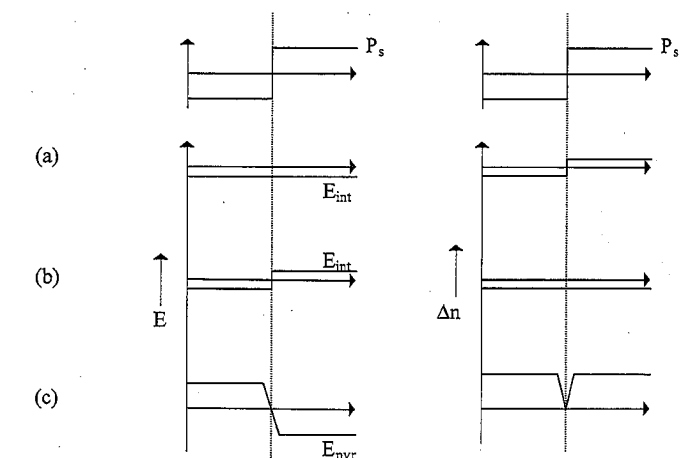


Fig. 44. A schematic explaining the electric fields, and the origin of optical contrasts at a domain wall. (a) Crystal at room temperature, (b) crystal after a high temperature anneal, (c) crystal after creating pyroelectric fields on the surface. Region left of the broken line: virgin crystal, region right of the broken line: room-temperature domain-reversed crystal. Reprinted with permission from V. Gopalan and M. C. Gupta, *J. Appl. Phys.*, 80, 6099, (© 1996 American Institute of Physics).

During the annealing process, the internal field E_3^{internal} realigns parallel to the new polarization direction, and therefore the Δn_o and the scattering at the domain wall disappears. The E_2 disappears as well, resulting in a loss of optical birefringence. When the crystal is rapidly heated and cooled down, pyroelectric fields are created as shown in Figure 44. The magnitude of the pyroelectric field E_p across the crystal for a ΔT change in temperature is $E_p \sim p \Delta T / \epsilon$, where p is the pyroelectric coefficient, ($p_3 = 2.3 \times 10^{-4} \text{ C K}^{-1} \text{ m}^{-2}$ for LiTaO_3 and ϵ is the dielectric constant ($\epsilon_{33} = 44$ for LiTaO_3). For a $\Delta T \sim 25^\circ\text{C}$, the pyroelectric field is 15 kV mm^{-1} . Due to surface mobility, some pyroelectric charges across the domain walls will compensate each other resulting in a field distribution passing through zero at the domain wall, as shown. This provides a net index increase away from the walls, and a net index decrease close to the walls, giving rise to scattering and hence wall contrast.

4.3.4. X-Ray Synchrotron Studies of Domains

High-resolution monochromatic synchrotron X-ray diffraction imaging [125–128] is a powerful probe defect and strain in crystal lattices. Gopalan et al. [129] studied congruent LiNbO_3 and LiTaO_3 in detail using this technique using an 8-keV beamline at the National Synchrotron Light source, Brookhaven National Labs, NY. The experimental geometry is shown in Figure 45. The beamline produces a monochromatic X-ray beam with a divergence of less than 10^{-6} . As a result, small regions in the crystal under examination that deviate from the surrounding area either in lattice parameter or in lattice orientation by more than a part per million in the direction of diffraction, do not fulfill the Bragg condition locally, when oriented in the vicinity of the edge of a Bragg diffraction peak from the crystal as a whole. This local nonfulfillment of the Bragg condition in otherwise highly regular crystals produces decipherable features in the diffraction images. From the particular changes in the visibility of individual features with specific changes in orientation of the crystal with respect to the beam, the precise nature of the associated structural irregularity can be determined. In addition, form factor for diffraction in the $+z$ -direction differs from that in the $-z$ -direction, introducing contrast between domains in the two orientations in images formed by diffraction with a component in the z -direction.

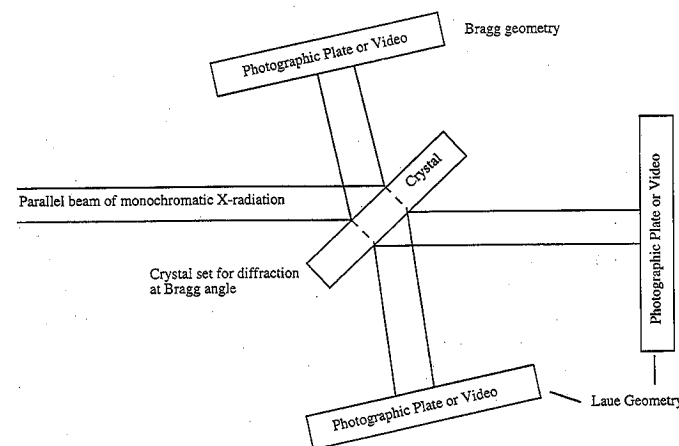


Fig. 45. A schematic of experimental setup for the diffraction images using an X-ray synchrotron source.

Figure 46 shows the X-ray Bragg image (a), and the corresponding optical image (b) of the ferroelectric domains formed in a z -cut congruent LiTaO_3 crystal by external electric field at room temperature. In this state, the triangular domains are in the frustrated state of internal field (State II in Fig. 20), giving rise to internal fields, strains, and optical birefringence at a domain wall, as shown in Figure 46(b). One clearly observes the one-to-one correspondence between optical and X-ray images in (a) and (b). However, the X-ray images reveal details that are not obvious in the optical image. The X-ray image was taken with the crystal matrix at a Bragg angle of 19.725° corresponding to $[0006]$ reflection of LiTaO_3 . The plane of incidence was parallel to the crystallographic y -direction (vertical direction in the image). The triangular domain regions in the X-ray picture are predominantly dark, indicating a destruction of the Bragg condition in those regions. This indicates that the lattice parameter along the c -direction changed within the triangular domain regions as compared to the matrix value. A very rough estimate of the upper limit for the observed strain in the domains can be estimated as follows. The deviation from Bragg angle of 1 arcs ($\sim 5 \mu\text{rad}$) results in a change in image contrast from a completely white to a completely black region. For the current Bragg angle, this translates into a lattice strain $\Delta d/d \sim 1.4 \times 10^{-5}$ where d is the lattice parameter in the polarization direction. In comparison, the strain ϵ_3 measured in the polarization direction by CMNSOM was $\sim 10^{-6}$ as described in Section 4.3.1. The discrepancy is believed to arise from the fact that the change in contrast across the domain wall in Figure 46(a) may correspond to a change in Bragg angle of less than 1 arcs, because the image contrast appears to be in shades of gray, rather than being clearly white or black. Further, details within the triangles reveal regions with varying contrast as well indicating internal structure, which is not seen in the optical image. In Section 5.2.6, one observes such defects regions within growing domains which were found to be regions where domain reversal does not occur. This would be consistent with the brighter contrast of these regions observed in the X-ray images here. The actual width of the image contrast at the domain wall triangles appears to be of the order of

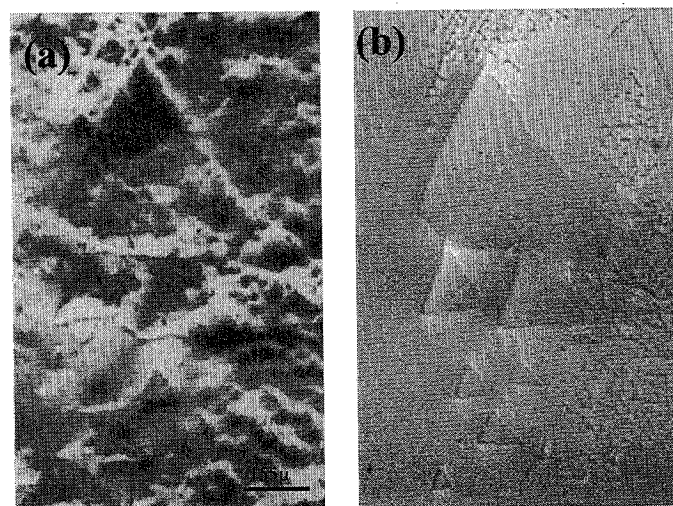


Fig. 46. (a) The X-ray synchrotron image of 180° domains in the z -plane of congruent LiTaO_3 . (b) The corresponding optical image of the same area in unpolarized light. Reprinted with permission from V. Gopalan, S. Kim, and B. Steiner, *Appl. Phys. Lett.*, 71, 1774, 2000. © American Institute of Physics, 2000.

many microns, perhaps as large as $1\text{--}20 \mu\text{m}$. These values are again consistent with the wide regions of optical birefringence seen by CMNSOM [82]. However, the X-ray images are more sensitive to small strains, while CMNSOM may lack the signal sensitivity to detect optical birefringence of $<10^{-6}$. Therefore, the wider regions of strain contrast seen in Figure 46 may be more representative.

Figure 47(a) and (b) shows the X-ray and optical images of a domain formed in congruent LiNbO_3 at room temperature. The X-ray image was again taken in the $[0006]$ Bragg reflection geometry. The preferred domain wall orientation in LiNbO_3 are walls parallel to the crystallographic y -axes. However, one notices significant deviations from the y -axis directions, in the vertical wall to the right. This wall was created at the edge of the liquid electrode used to apply the electric field. The domain walls adjoining the electrode edges show significant optical birefringence and strain. This can also be confirmed from the optical image of Figure 35(a) where the brightest contrast is shown by domains along an arc on the upper right-hand corner, which followed the electrode edge. The overall contrast inside and outside the domain are similar in the X-ray image of Figure 47(a), suggesting that the lattice strain is much smaller in this case as compared to domains in congruent LiTaO_3 . The vertical domain wall on the left (which is also the farthest from the electrode edge in this domain), shows the least contrast. Domains which are well inside the electrode interior, show wall contrast similar to this wall. However, the thick dark bands adjacent to the other domain walls in Figure 47(a) indicates a considerably larger strain. Itagi et al. performed Ginzburg–Landau free energy calculations for domain walls in LiNbO_3 and LiTaO_3 as a function of wall orientation in the z -plane. They show that while domain walls parallel to x -planes (such as in congruent LiTaO_3) should have shear strains in the x - y - and the y - z -planes in the wall, these strains disappear for walls along the y -axes. This appears to be consistent with the X-ray observations which show lower strain contrast for domains in congruent LiNbO_3 than for congruent LiTaO_3 . These results are discussed in detail in the next section.

4.3.5. Ginzburg–Landau Free Energy Theory of Domains Shapes

There are three main types of domain shapes observed in LiNbO_3 and LiTaO_3 as shown in Figure 36. The triangular domains with

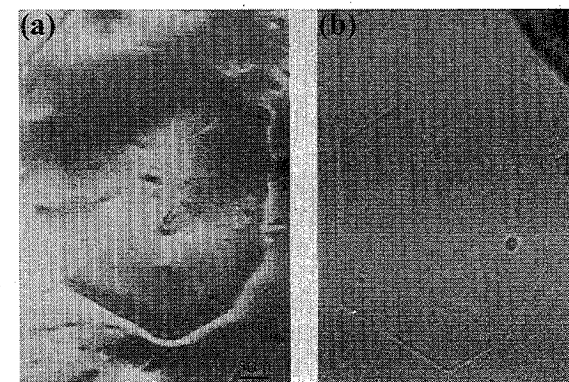


Fig. 47. (a) The X-ray synchrotron image of 180° domains in the z -plane of congruent LiNbO_3 . (b) The corresponding optical image of the same area in unpolarized light. Reprinted with permission from V. Gopalan, S. Kim, and B. Steiner, *Appl. Phys. Lett.*, 71, 1774, 2000. © American Institute of Physics, 2000.

domain walls parallel to the crystallographic x -axes are seen in congruent LiTaO_3 when domains are created at low driving fields. This shape was also reported in congruent crystals of LiNbO_3 doped with LiVO_3 [130]. At large electric fields, the triangular domains in congruent LiTaO_3 evolve into six-sided domains, with walls still parallel to the crystallographic x -axes. The third shape, namely, the hexagons with domain walls parallel to the crystallographic y -axes are seen in stoichiometric composition of both materials, as well as in congruent crystals of LiNbO_3 . It is therefore clear that the shape of domains in these materials is a sensitive function of lithium stoichiometry, and driving fields for domain creation.

Itagi et al. [131] attempted to understand these phenomena of domain shape changes by performing the Ginzburg–Landau free energy theory [62] analysis of infinite domain walls in LiNbO_3 and LiTaO_3 . Their analysis is briefly detailed in the following text. Consider a single 180° domain wall in LiNbO_3 or LiTaO_3 which is at an angle of θ to the crystallographic x -axis in the x - y -plane as shown in Figure 48. The crystallographic x -, y -, and z -axes correspond to notation 1, 2, and 3, respectively. Defining the wall coordinates x_n and x_t to be parallel and normal to the domain wall such that (x_n, x_t, x_3) form a right-handed Cartesian coordinate, and assuming an infinite extent of the wall in the x_t and x_3 directions, the strain and polarization will only vary as a function of coordinate x_n . The invariant free energy for the system can be written as

$$F = \frac{\alpha_2}{2} P^2 + \frac{\alpha_4}{2} P^4 + \beta_2 (\epsilon_n + \epsilon_t)^2 + \beta_3 [(\epsilon_n - \epsilon_t)^2 + \tilde{\epsilon}_6^2] + \beta_4 \epsilon_3 (\epsilon_n + \epsilon_t) + \beta_5 (\epsilon_4 + \epsilon_5)^2 + \beta_6 [(\epsilon_n - \epsilon_t) \tilde{\epsilon}_4 \cos(3\theta) + \tilde{\epsilon}_5 \tilde{\epsilon}_6 \cos(3\theta)] + (\epsilon_n - \epsilon_t) \tilde{\epsilon}_5 \sin(3\theta) - \tilde{\epsilon}_4 \tilde{\epsilon}_6 \sin(3\theta) + \gamma_1 (\epsilon_n + \epsilon_t) P^2 + \gamma_2 \epsilon_3 P^2 + g_1 \left(\frac{dP}{dx_n} \right)^2 + g_2 P \left(\frac{d^2 P}{dx_n^2} \right) \quad (24)$$

where the strains ϵ_{ij} are defined as

$$\begin{aligned} \epsilon_n &= \partial u_n / \partial x_n = u_{n,n} \\ \epsilon_t &= u_{t,t} \\ \epsilon_3 &= u_{3,3} \\ \tilde{\epsilon}_4 &= u_{t,3} + u_{3,t} \\ \tilde{\epsilon}_5 &= u_{n,3} + u_{3,n} \\ \tilde{\epsilon}_6 &= u_{t,n} + u_{n,t} \end{aligned} \quad (25)$$

The ϵ_n is the dilational strain normal to the wall, ϵ_t and ϵ_3 are the dilational strains in the plane of the wall, $\tilde{\epsilon}_4$ is the shear strain in the wall (x_t, x_3 plane), $\tilde{\epsilon}_5$ is the shear strain in the plane perpendicular to the domain wall (in the x_n, x_3 plane), and $\tilde{\epsilon}_6$ is the shear strain in the z -plane of the crystal. The polarization P along direction 3 is the primary order parameter, and the β and the γ are given by

$$\begin{aligned} \beta_1 &= c_{33}/2 \\ \beta_2 &= (c_{11} + c_{12})/4 \\ \beta_3 &= (c_{11} - c_{12})/4 \\ \beta_4 &= c_{13} \\ \beta_5 &= c_{44}/2 \\ \beta_6 &= c_{14} \end{aligned} \quad (26)$$

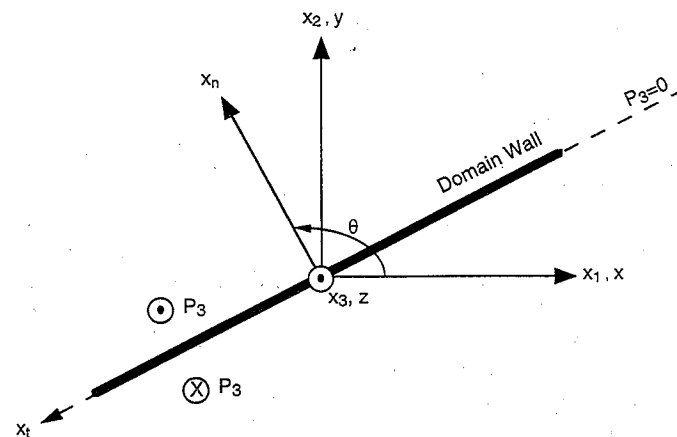


Fig. 48. A schematic depicting the coordinate axes choice for the calculation of free energy of a domain wall in LiNbO₃ or LiTaO₃. The (x, y) [or (x_1, y_1)] are the crystallographic axes while (x_1, x_2) are the domain wall axes. A. Itagi, V. Gopalan, A. Saxena, P. Swart, T. E. Schlesinger, and D. Stancil, unpublished.

and

$$\begin{aligned} 2\gamma_1 &= c_{13}q_{33} + (c_{11} + c_{12})q_{13} \\ 2\gamma_2 &= c_{33}q_{33} + c_{13}q_{13} \end{aligned} \quad (27)$$

where c_{ij} are the elastic constants and q_{ij} are the electrostrictive coefficients. When the gradient terms of g_1 and g_2 are set to zero, the free energy in Eq. (24) goes to that of homogeneous value corresponding to no domain wall, and a single domain region. In the absence of any domain wall, one can show that a homogeneous polarization P_{hom} develops in the crystal structure at room temperature, and homogeneous strains ϵ_1 , ϵ_2 , and ϵ_3 proportional to the P_{hom}^2 through electrostriction. In LiTaO₃, for example, homogeneous values of ϵ_1 , $\epsilon_2 \sim 1.4 \times 10^{-3}$ and $\epsilon_3 \sim -2.7 \times 10^{-3}$ use tabulated values of elastic and electrostrictive constants [124]. These values are then used as the boundary conditions for polarization and strain in the inhomogeneous case for regions far away from the infinite domain wall on either sides.

Minimizing the free energy in Eq. (24) with nonzero gradient terms leads to kink-like solutions for the polarization variation across the walls. The minimum free energies were found to correspond to the domain walls parallel to the six crystallographic x -axes as shown in Figure 49. While all the six walls with minimum energy are degenerate, they differ in the sign of the shear strain $\bar{\epsilon}_5$ as shown in Figure 50. Two sets of minimum energy walls can be recognized: the set A with positive shear strain, and set B with negative shear strain. The polarization, P , and the shear strain $\bar{\epsilon}_5$ across the wall are shown for these two sets of walls in Figure 51. The shear strains $\bar{\epsilon}_4$ and $\bar{\epsilon}_6$ are zero for the minimum energy domain walls.

To interpret the previous results, one needs to take a closer look at the assumptions of the model itself. First, the model did not consider the influence of any defects in the crystal structure. Therefore, the effect of lithium nonstoichiometry in LiNbO₃ or LiTaO₃ cannot be predicted by the preceding model, and comparisons can only be made between the predictions and the domain shapes seen in stoichiometric crystals. Second, the free energy in Eq. (24) only considers a single infinite domain wall. There are no energy terms for incorporating intersections of domain walls.

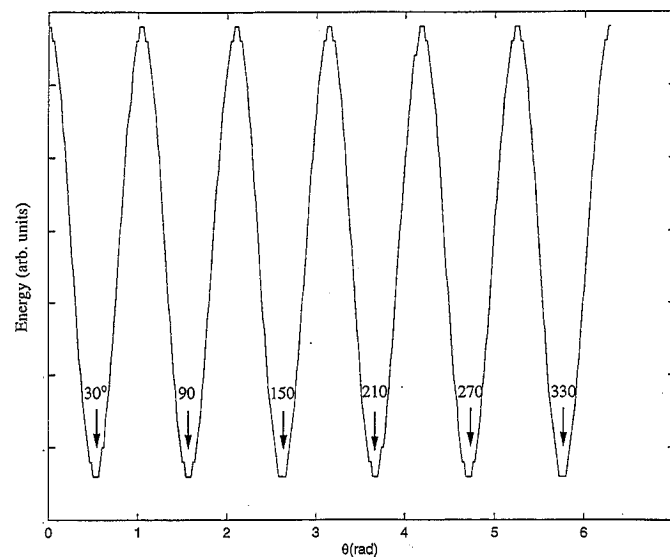


Fig. 49. The free energy as a function of orientation of domain wall, θ in the z -plane of LiTaO₃ (see Fig. 48 for coordinate definition). The set of domain walls corresponding to $\theta = 30^\circ, 150^\circ$, and 270° are labeled as walls B, and the set of domain walls corresponding to $\theta = 90^\circ, 210^\circ$, and 330° are labeled as walls A in the text. A. Itagi, V. Gopalan, A. Saxena, P. Swart, T. E. Schlesinger, and D. Stancil, unpublished.

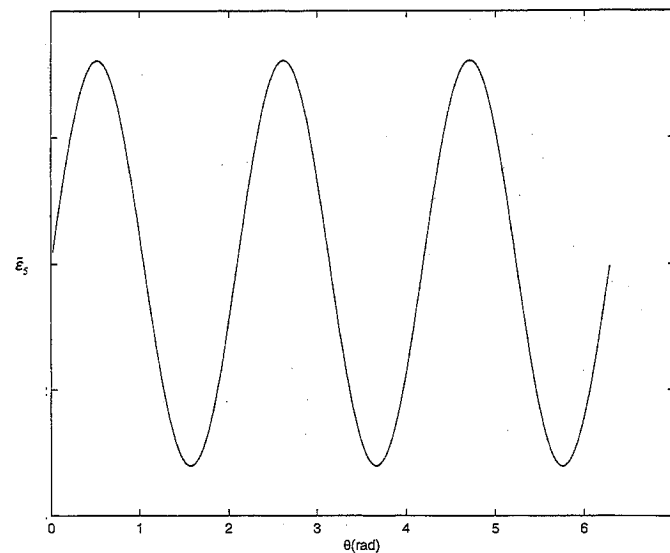


Fig. 50. The shear strain $\bar{\epsilon}_5$ at a domain wall in the $x_1 - x_3$ plane (see Fig. 48 for coordinate definition) as a function of domain wall orientation in the z -plane of LiTaO₃. A. Itagi, V. Gopalan, A. Saxena, P. Swart, T. E. Schlesinger, and D. Stancil, unpublished.

With these considerations in mind, if one compares the domain shapes predicted here with the actual observed shapes of domains in stoichiometric crystals, one finds that they are rotated by 60° . While the predicted minimum energy domain walls are parallel to the x -axes, the observed domain walls are parallel to the y -axes. The presence of a nonzero shear strain $\bar{\epsilon}_5$ in the predicted domain walls implies that the surface of a z -cut crystal will exhibit a step in going across a domain wall. A change in sign of the strain $\bar{\epsilon}_5$ therefore implies a step up or a step down in going from one domain to another across the wall. Therefore, intersections of walls

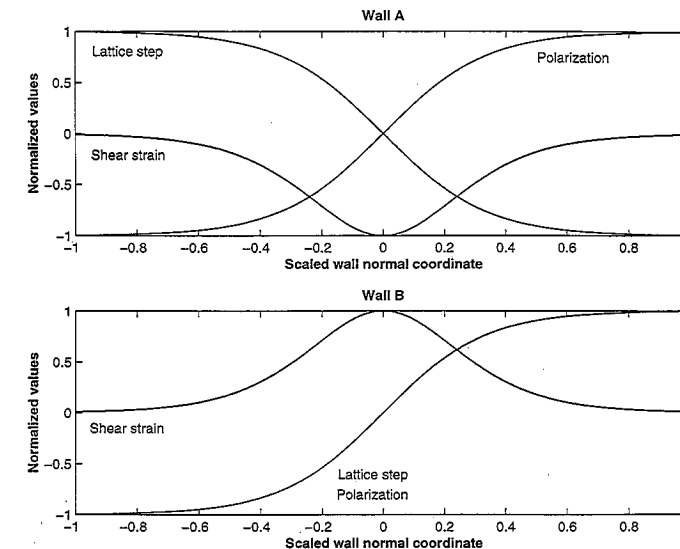


Fig. 51. The variation of polarization, strain, and domain wall step across 180° domain walls in congruent LiTaO₃ (and LiNbO₃) given by the minima in free energy. A. Itagi, V. Gopalan, A. Saxena, P. Swart, T. E. Schlesinger, and D. Stancil, unpublished.

A and B (six vertices of the hexagon) should be high energy locations, where strains can only be accommodated by the presence of a screw dislocation. This implies that within the framework of the present model, for a hexagonal domain with walls parallel to the x -axis to be possible, one would require alternately right-handed and left-handed screw dislocations at the vertices of the predicted hexagon. On the other hand, the shear strains $\bar{\epsilon}_5$ are zero for the domain walls parallel to the crystallographic y -axes as seen from Figure 50.

It therefore appears that the domain walls parallel to the y -axes are preferred by stoichiometric crystals since it leads to a zero shear strain $\bar{\epsilon}_5$, and therefore to lower energies of vertices formed by domain wall intersections. One can further ask what influence the creation of lithium nonstoichiometry has on domain shapes. In congruent LiNbO₃, the domain walls remain parallel to the y -axes. In congruent LiTaO₃, the domain walls become parallel to the x -axes. This transformation is clearly defect-mediated, and can only be understood by including extra energy terms in Eq. (9) which represent the symmetry and physical properties of the defects themselves. At present, the precise of nature and structure of these defects is not known.

At low driving fields, however, only the set A of planes in Figure 50 is preferred. However, at large driving fields, all the six domain walls parallel to the x -axes are created. These facts suggest that the nonstoichiometric defects lift the degeneracy between the set of walls A and B, making A slightly more preferred to the walls B. At low driving fields, the domain growth is slow and closer to steady state, and the difference in energy between the two sets of walls is manifested resulting in triangular domains. At higher driving forces, the energy difference between these sets of walls may be overcome by the fact that a hexagonal domain covers more area than a triangular domain (for the same radius of an imaginary circle that would circumscribe them). Therefore, a decrease in electrostatic energy by domain reversal under large driving fields may more than overcome the increase in energy in creating the set of domain walls B as well.

5. THE DYNAMICS OF DOMAIN NUCLEATION AND GROWTH

5.1. Introduction

The dynamics of antiparallel ferroelectric domains in lithium niobate and lithium tantalate has received considerable attention. A few studies existed in the past which reported switching times at higher temperature [119]. However, no such studies existed at room temperature, where most of the device processing takes place today. Studies of domain dynamics using real-time optical imaging [132, 133] opened up this field and revealed many interesting phenomena which often escape notice in ex situ studies such as domain merger, wall stabilization, and large differences in the magnitude of wall mobilities measured ex situ and in situ. Further, studies on submicroscopic length scales of the bending movement of a domain wall well below the threshold field for domain reversal suggests that the coercive fields for domain reversal may well correspond to pinning-depinning transitions [82]. This section reviews these advances in our knowledge of how domains move under external fields in LiNbO₃ and LiTaO₃.

5.2. Congruent Lithium Tantalate

In this section, we present switching times, sideways wall velocity measurements, and nucleation and stabilization mechanisms of 180° domains as a function of external electric fields in congruent z -cut LiTaO₃ crystals at room temperature. This section closely follows the work of Gopalan et al. [132–134].

5.2.1. Domain Switching Times

The switching times and maximum transient current, as a function of applied electric field is shown for forward poling (t_f and $i_{f, \text{max}}$, respectively) and for reverse poling (t_r and $i_{r, \text{max}}$, respectively) in Figure 52 for two wafers A and B [134]. The width of the transient current pulse was measured to obtain the polarization switching times, t_f and t_r for the forward and reverse poling cycles, respectively. Every new pair of measurements of (t_f , t_r) at a different set of fields was made on a new piece of crystal, thus avoiding the effects of polarization cycling history on coercive fields of the crystal [135]. To study the effect of differences from one wafer to the other, two wafers (denoted as wafer A and wafer B) were studied and compared. Step voltages of various magnitudes were applied and the transient current response was measured.

The error bars on switching times are $\sim \pm 10\%$ of the switching times. The following observations were made: (1) $\ln(t_{f, r})$ is linear with $1/E$, implying that the switching time depends exponentially on electric field E ; (2) the switching times, $t_f \propto 1/i_{f, \text{max}}$ and $t_r \propto 1/i_{r, \text{max}}$; (3) there is a clear change of slope in the linear fits for $\ln(t_{f, r})$ versus $1/E$, implying a change in activation field from low field to high field; (4) the activation field (slope of linear fits) is the same for wafers A and B, in both forward and reverse directions; and (5) the forward poling fields are lower for wafer B as compared to wafer A. The reverse poling fields are the same.

The large difference in the forward poling fields and reverse poling fields arises from the presence of internal fields, E_{int} aligned parallel to the polarization direction of the virgin LiTaO₃ crystals as described before. The magnitude of this field is given by $E_{\text{int}} = (E_f - E_r)/2$, where E_f is the field required for forward poling, and E_r is the field required for reverse poling. The internal

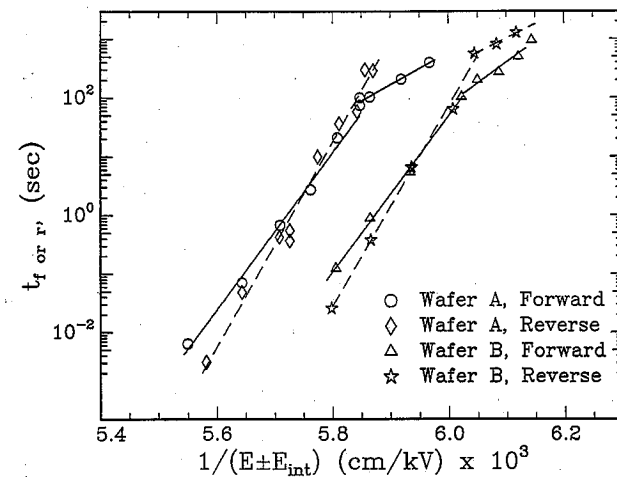


Fig. 52. The switching time, t_f and t_r for the forward and reverse poling, respectively, of 180° domains z -cut LiTaO_3 as a function of field $E \pm E_{\text{int}}$, where the minus sign is for forward poling and the plus sign for reverse poling. The E_{int} for wafers A and B are 46.36 kV cm^{-1} and 42.2 kV cm^{-1} , respectively. Reprinted from V. Gopalan, *J. Appl. Phys.*, 83, 941 (1998).

fields for wafer A and for wafer B were $E_{\text{int}, A} = 46.36 \text{ kV cm}^{-1}$ and $E_{\text{int}, B} = 42.2 \text{ kV cm}^{-1}$, respectively.

The field axis is therefore transformed as $E_f \Rightarrow E_f - E_{\text{int}}$ and $E_r \Rightarrow E_r + E_{\text{int}}$ and uses the appropriate internal field values for wafers A and B in the transformation as shown in Figure 52. Gopalan and Mitchell [134] denoted the field region $E \pm E_{\text{int}} < E_0$ as the "low-field regime" and $E \pm E_{\text{int}} > E_0$ as the "high-field regime" where $E_0 = 170.9 \text{ kV cm}^{-1}$ for wafer A and $E_0 = 165.8 \text{ kV cm}^{-1}$ for wafer B. The term $E \pm E_{\text{int}}$ should be interpreted as $E_f - E_{\text{int}}$ for forward poling and as $E_r + E_{\text{int}}$ for reverse poling. The switching time can now be written as a function of electric field, $E \pm E_{\text{int}}$ as

$$t_f = t_{f0} \exp \left[\frac{\delta_f}{E_f - E_{\text{int}}} \right] \quad (28)$$

$$t_r = t_{r0} \exp \left[\frac{\delta_r}{E_r + E_{\text{int}}} \right] \quad (29)$$

The values of the pre-exponents t_{f0} and t_{r0} and the activation fields δ_f and δ_r are listed for the two wafers A and B in Table V. The δ_f (or δ_r) has two distinct values: the values in the low-field regime are much smaller than the values in the high-field regime.

By transforming the field E to $E \pm E_{\text{int}}$ the switching time data for the forward poling and reverse poling cases overlap in the same field region for each wafer. However, the field regions $E \pm E_{\text{int}}$ where domain reversal occurs is still distinctly different for wafers A and B. Since nonstoichiometric point defects in LiTaO_3 crystals dramatically influence the coercive and internal fields as seen before, the slight variations in the concentration of point defects from wafer to wafer may explain the observed small differences in internal fields between the two wafers.

5.2.2. Domain Stabilization Times

It is observed that a voltage pulse of width <1.5 – 2 s and zero baseline voltage results in reversible domain wall motion during the forward poling. Hence, no net domain reversal is observed even at field values as high as 245 kV cm^{-1} . At this field, one would

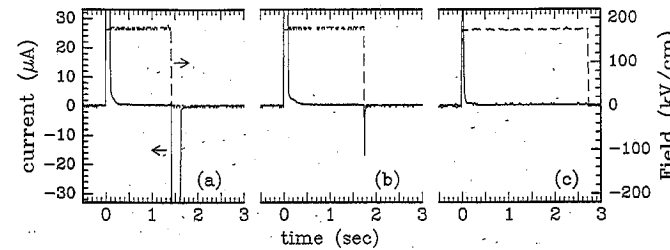


Fig. 53. Voltages of three different pulse widths (a)–(c) showing (a) completely reversible domain motion suggested by negative current after the pulse, (b) partial reversible domain motion, and (c) stabilized domain wall motion in congruent LiTaO_3 crystals.

expect switching times in the microsecond regime (from Fig. 52) using step voltages. Figure 53 shows three different voltage pulses that show stable domain reversal, unstable domain reversal, and partially stable domain reversal for forward poling. Similar experiments were done in reverse poling as well. From these experiments, the following conclusions were drawn:

(1) An initial voltage pulse with a field of sufficient magnitude (in the ranges shown in Fig. 52) will nucleate a few microdomains in the sample even with a pulse width as small as 100 ms in forward poling. The density of such nuclei is usually very small. These domains are most probably associated with physical defects in the crystal, where small 180° microdomains can be trapped and remain stable when the field is removed [136]. Etching experiments in LiNbO_3 and LiTaO_3 single crystals have shown that even in single crystal single domain wafers, 180° microdomains in concentration of $\sim 10^3$ – 10^5 cm^{-2} exist [137, 138].

(2) Independent of the magnitude of the field (certainly up to 245 kV cm^{-1} in forward poling up to 142.3 kV cm^{-1} in reverse poling), a voltage pulse with zero baseline voltage will not result in a net growth of any existing 180° domains, or the creation of any new domains in the crystal unless the voltage pulse is at least ~ 1.5 – 2 s wide in the forward poling direction and at least 0.1 – 0.3 s in the reverse poling direction. Thus, there is a large asymmetry in the stabilization times for forward and reverse poling.

(3) For an applied voltage pulse (with zero baseline voltage) of sufficient magnitude to induce polarization reversal but pulse widths of <1.5 – 2 s in forward poling and <0.1 – 0.3 s in reverse poling, any growth of existing domains or the nucleation of new domains is reversible, i.e., the existing domains return to their original size, and any newly nucleated domains disappear. The fact that actual nucleation and growth do occur for these short pulses is reflected from very clear transient current peaks. However, the time taken for the domain microstructure to switch back to its original state after the removal of the field can be much faster than the original switching time, especially at low fields.

The large asymmetry in the stabilization times for a 180° domain in the forward poling direction (~ 1.5 – 2 s) and the reverse poling direction (0.1 – 0.3 s) is reminiscent of the large asymmetry in the forward poling field, E_f , and the reverse poling field E_r , since the internal field, E_{int} , is parallel to the polarization direction in a virgin crystal. When the polarization of the crystal is reversed at room temperature by forward poling, the internal field becomes antiparallel to the polarization direction. However, annealing this crystal at a temperature above 200°C for less than 30 s and cooling back to room temperature results in $\sim 95\%$ realignment of the internal field parallel

Table V. The Values of Activation Fields and Pre-exponents for LiTaO_3 in Eqs. (28) and (29)*

	Field regimes ^a	$\ln(t_{f0}, \text{s})$	$\delta_f (\text{kV cm}^{-1})$	$\ln(t_{r0}, \text{s})$	$\delta_r (\text{kV cm}^{-1})$
Congruent LiTaO_3	$E \pm E_{\text{int}, A} < 170.9 \text{ kV cm}^{-1}$	-69.74 ± 6.78	$12,688 \pm 1151$	—	—
Wafer A	$E \pm E_{\text{int}, A} > 170.9 \text{ kV cm}^{-1}$	-185.45 ± 7.16	$32,441 \pm 1248$	230.48 ± 10.27	$40,232 \pm 1785$
Congruent LiTaO_3	$E \pm E_{\text{int}, B} < 165.8 \text{ kV cm}^{-1}$	-94.38 ± 18.13	$16,486 \pm 2965$	-61.92 ± 5.58	$11,287 \pm 917$
Wafer B	$E \pm E_{\text{int}, B} > 165.8 \text{ kV cm}^{-1}$	-177.91 ± 3.98	$30,350 \pm 670$	-231.63 ± 9.13	$39,389 \pm 1542$
Near-stoichiometric LiTaO_3	$E \pm E_{\text{int}} < 16.7 \text{ kV cm}^{-1}$	-81.24 ± 10.5	1275.3 ± 161	-66.73 ± 5.5	1047 ± 84
	$E \pm E_{\text{int}} > 16.7 \text{ kV cm}^{-1}$	-13.62 ± 0.4	-151.8 ± 7.4	-14.01 ± 0.6	161 ± 11

*Source: Ref. [134].

^a $E_{\text{int}, A} = 46.36 \text{ kV cm}^{-1}$; $E_{\text{int}, B} = 42.2 \text{ kV cm}^{-1}$; E_{int} (near-stoichiometric) = 1.8 kV cm^{-1} ; $E \pm E_{\text{int}, A}$ should be interpreted as $E_f - E_{\text{int}, A}$ for forward poling and $E_r - E_{\text{int}, B}$ for reverse poling; similarly for others.

to the new polarization direction. If the stabilization process for the 180° domains is related to the internal fields, then upon annealing a forward poled crystal above 150°C and cooling it back down to room temperature, the stabilization time for reverse poling back to its virgin state should increase from ~ 0.1 s to ~ 1.5 s. Indeed, experimentally it was found that a voltage pulse had to be at least ~ 1.25 s wide for the nucleation of new domains or the growth of existing domains. Though this value is slightly smaller than the stabilization time for forward poling (~ 1.5 – 2 s), it is much larger than the stabilization time (0.1 – 0.3 s) for reverse poling without annealing the crystal in its "domain-reversed state" or State II in Figure 20. This experiment strongly suggests a correlation between the internal fields and the stabilization mechanism of 180° domains in LiTaO_3 crystals.

One can construct the following plausible physical picture. In the virgin state of a congruent LiTaO_3 crystal, point defect complexes (consisting of nonstoichiometric point defects) with their own dipole moment are aligned parallel to the spontaneous polarization, P_s , in their lowest energy state. In this state, they can be imagined to give rise to an effective internal field, $E_{\text{int}, \text{total}}$, parallel to the spontaneous polarization of the crystal and contribute to the stabilization of P_s . When the polarization P_s is reversed at room temperature by an external field, these point defects now become antiparallel to the new polarization direction, $-P_s$, and hence become unstable. They in turn realign parallel to the new polarization direction. This realignment may have many time constants at a given temperature. Drawing analogy from similar internal field studies of doped BaTiO_3 ceramics [139, 141] we can hypothesize that the time dependence of the total internal field is

$$E_{\text{int}, \text{total}} = \sum_{i=1, 2, 3, \dots} E_{\text{int}, i} \left(2 \exp \left(-\frac{t}{\tau_i} \right) - 1 \right) \quad (30)$$

Thus, at $t = 0$ in the domain-reversed state (State II), the internal field $E_{\text{int}, \text{total}} = -\sum_i E_i$ and for $t = \infty$, $E_{\text{int}, \text{total}} = \sum_i E_i$. At time $t \sim 4\tau_i$, the field component E_i changes to $\sim -0.95 E_{\text{int}, i}$. There appear to be at least three different time constants, τ_i involved in relaxation process of internal fields at room temperature. Brown et al. [141] reported at least two constants τ_i of $\tau_1 \sim 8.3$ s and $\tau_2 \sim 132$ s. The faster relaxation component appears closer

to the stabilization time of 1.5 – 2 s seen in congruent LiTaO_3 . An additional slow relaxation component τ_3 seems to exist for the internal field of 5 kV mm^{-1} which is given by the offset of the polarization hysteresis in Figure 20. This component has a time constant $4\tau_3$ of the order of many months at room temperature and less than 30 s at temperatures above 200°C . The fast component is responsible for stabilization of newly created domains by forward poling, while the slow time constant (of months) reported earlier gives rise to the large asymmetry in forward (E_f) and reverse (E_r) poling fields at room temperature. It would then appear that the fast component responsible for stabilization requires the electric field to be "on" for 1.5 – 2 s after the creation of new 180° domains for the stabilization to take place in forward poling. Therefore, this relaxation must be a field driven process, and may involve the movement of electronic charges. However, the slow component of the internal field, E_{int} , exists even without the external field, and realigns parallel to the polarization direction in a domain-reversed state with time and temperature.

5.2.3. Ex situ Studies of Sideways Growth Velocity

The sideways wall velocity of 180° domains in the z -plane of LiTaO_3 was measured [134] by applying voltage pulses to the sample and observing it ex situ by transmitted light microscopy. Figure 54 shows an example of a sequence of pulses corresponding to a field of 215.3 kV cm^{-1} applied to a sample from wafer A in the forward poling direction. The total expected switching time from Figure 52 is ~ 120 s. The pulse widths varied from 10 – 15 s. After each pulse, the liquid electrodes were removed and the sample was observed by light microscopy without removing it from the holder used to apply high voltage pulses. Photographs were taken of the growing domains (at $72\times$ magnification using unpolarized transmitted light) in the z -plane of a fixed area of the sample after every pulse.

Figure 55(a) and (b) shows two snapshots of growing domains during this sequence. Figure 55(a) was taken after pulse (3) of Figure 54(a). Figure 55(b) was taken after pulse (4) of Figure 54(a) in the same area. One can clearly see a one-to-one correspondence between each domain in Figure 55(a) and (b). One example of a corresponding domain is shown by arrows. Each side a of the equilateral triangle of a domain was measured and the value of

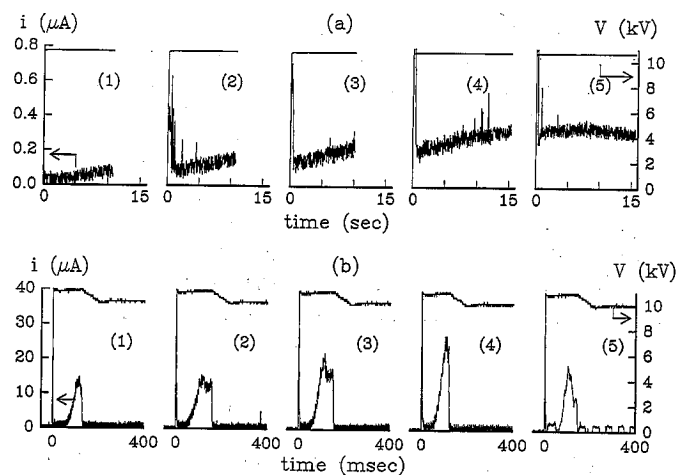


Fig. 54. A series of voltage pulses applied to measure the sideways velocity of 180° domains, v_s , during forward poling of a z-cut LiTaO₃ crystal, (wafer A). (a) Experiments at 215.3 kV cm^{-1} where switching time expected was $\sim 120 \text{ s}$, and (b) experiments at 221.2 kV cm^{-1} where the total switching time is $\sim 0.7 \text{ s}$. Since this is less than the stabilization time, a baseline voltage of 201 kV cm^{-1} is applied after the main voltage pulse. V. Gopalan, *J. Appl. Phys.*, 83, 941 (1998).

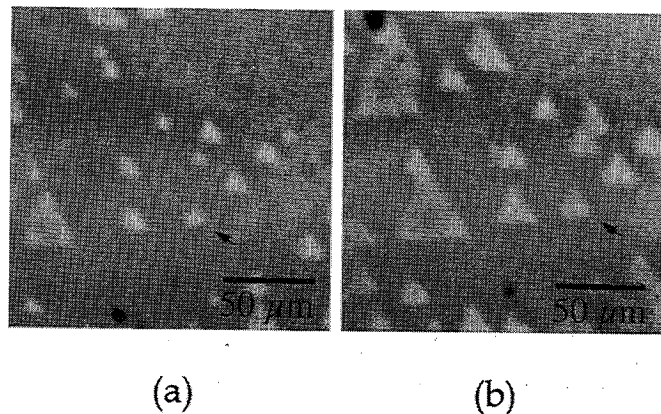


Fig. 55. Two snapshots in time of growing 180° domains in z-cut congruent LiTaO₃ crystals taken by light microscopy in unpolarized transmitted light. An electric field of 215.3 kV cm^{-1} for 15 s was applied for the growth. V. Gopalan, *J. Appl. Phys.*, 83, 941 (1998).

$b = a \cdot \tan(30^\circ)/2$ calculated. The value b represents the shortest distance of any side of the equilateral triangle from the point intersection of medians of the triangle. Since the triangles grow into larger triangles with field, b represents the distance that any side of the triangle grows away from the center of the triangle. The sideways velocity (v_s) for one growing domain was then calculated, for example, by measuring b_1 for a domain in Figure 55(a), and a value b_2 for the same domain in Figure 55(b), and calculating $v_s = (b_2 - b_1)/\Delta t$ where Δt , in this case, is the pulse width of pulse (4) in Figure 54(a). This was done for a number of individual growing domains for a fixed external field and an average taken of the values of v_s thus obtained. Care was taken to avoid considering domains which have merged together which would give an uncertainty in their individual sizes.

The previously described procedure works with applying square voltage pulses with zero baseline voltage, as long as the total switching time for a given field is greater than $1.5\text{--}2 \text{ s}$. However,

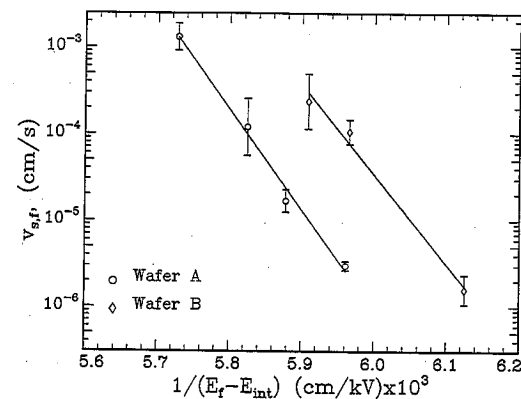


Fig. 56. The sideways wall velocity, v_s , of 180° domains during forward poling of a z-cut LiTaO₃ crystal as a function of electric field, $E_f - E_{\text{int}}$. V. Gopalan, *J. Appl. Phys.*, 83, 941 (1998).

for switching times of less than $1.5\text{--}2 \text{ s}$, one needs to apply voltage pulses even shorter than that. As seen in the previous section, such pulses result in *no net growth* of domains due to the requirement of $1.5\text{--}2 \text{ s}$ of stabilization time under a field after the pulse. Thus, to measure velocities at higher fields where switching times are less than a few seconds, voltage pulses with a baseline were used as shown in Figure 54(b). The sequence of pulses shown in Figure 54(b) was applied to a sample of wafer A corresponding to a field of 221.2 kV cm^{-1} in the forward poling direction. The total switching time at this field (from Figure 54) is $\sim 0.7 \text{ s}$. Each pulse consists of a $100\text{--}150 \text{ ms}$ width pulse of 221.2 kV cm^{-1} followed by a decrease of the field to a low value of 201 kV cm^{-1} where domain reversal is not observed (see Fig. 52). The transient current pulse is also arrested after the initial pulse and no further domain growth takes place at the baseline voltage. However, the presence of this baseline for at least $\sim 2 \text{ s}$ after the initial voltage pulse results in the stabilization of domains which have grown under the influence of that pulse. This way, the authors [134] could measure the sideways velocity of 180° domains at fields where switching times were less than $1.5\text{--}2 \text{ s}$. However, in this work [134] a systematic study of the effect of changing the baseline voltage on the stabilization process or the wall velocity was not performed. The baseline field of 201 kV cm^{-1} was arbitrary, which is close to the voltage range studied here, but where no domain reversal was observed over reasonable time scales ($\sim 1/2 \text{ h}$).

Figure 56 shows the sideways velocity of 180° domains in LiTaO₃ in the forward poling geometry for wafers A and B. The sideways velocity for forward poling geometry, $v_{s,f}$ can be written as

$$v_{s,f} = v_{s,fo} \exp \left(-\frac{\alpha_{s,f}}{E - E_{\text{int}}} \right) \quad (31)$$

The coefficients $\alpha_{s,f}$ and $v_{s,fo}$ are given in Table VI. We note that these velocities are underestimated by an order of magnitude due to the pulsed voltage measurement technique as shown in Section 5.2.4.

No measurements of the sideways wall velocity for the reverse poling direction were made. This was attributed to smaller nuclei sizes and larger density of nucleations, resulting in increased background scattering and birefringence in a crystal in a domain-reversed state. Thus, clear images of individual domains could not be obtained by light microscopy during reverse poling. However, drawing the analogy between forward and reverse poling from the

Table VI. The Values of Activation Fields and Pre-exponents in Eq. (31)^a

Velocity measurement \Rightarrow	Ex situ observation, pulsed voltage: Independent growing domains [134]	In situ observation, steady-state voltage: Independent domains [132]	In situ observation, steady-state voltage: merged domains [132]
	Wafer A	Wafer B	Wafer F
$\ln(v_{s,fo}, \text{cm s}^{-1})$	146.29 ± 10.27	132.55 ± 15.34	203.9 ± 25.3
$\alpha_{s,f} (\text{kV cm}^{-1})$	$26,698 \pm 3760$	$23,808 \pm 2556$	$35,200 \pm 4200$

$$^a E_{\text{int},A} = 46.36 \text{ kV cm}^{-1}; E_{\text{int},B} = 42.20 \text{ kV cm}^{-1}; E_{\text{int},F} = 44.15 \text{ kV cm}^{-1}.$$

switching times in Figure 25, one would expect an exponential behavior of sideways velocity in reverse poling geometry, $v_{s,r}$, with field as

$$v_{s,r} = v_{s,ro} \exp \left(-\frac{\alpha_{s,r}}{E + E_{\text{int}}} \right) \quad (32)$$

where the coefficients $\delta_{s,r}$ and $v_{s,ro}$ are expected to be comparable to the coefficients $\delta_{s,f}$ and $v_{s,fo}$, respectively. As proposed by Miller and Weinreich [142], the exponential behavior of v_s with external field E , of the form of Eq. (31) is obtained by considering the lateral movement of a 180° domain wall as a process of preferential nucleation at the wall surface. Assuming a dagger shaped critical nuclei with a thickness b equal to the smallest lattice constant in the direction of motion, a base of width $2a^*$, and height l^* , one can show that the sideways velocity [142]

$$v_s \propto \exp \left(-\frac{\Delta U^*}{kT} \right) \quad (33)$$

where T is the temperature, k is the Boltzmann constant, and ΔU^* is the net increase in total energy due to the critical nucleus, and is given by [142]

$$\Delta U^* = \frac{8b\sigma_p^{1/2}\sigma_w^{3/2}}{3\sqrt{3}P_sE} \quad (34)$$

The terms σ_p and σ_w are the depolarization energy per unit area and wall energy per unit area, respectively, and P_s is the spontaneous polarization.

On rewriting Eq. (33) as $v_s = v_{s,o} \exp(-\alpha_{s,o}/E)$, the value of α_s is $\sim 4313 \text{ kV mm}^{-1}$ (from Fig. 56). On combining Eqs. (33) and (34), one can relate the wall energies σ_p and σ_w to the measured constant, α_r . Following the treatment of Miller and Weinreich, σ_p can in turn be related to σ_w [142] and hence, one can estimate the wall energy, σ_w . Using the following parameters at $T = 300 \text{ K}$: $b = 5.15 \text{ \AA}$, dielectric constant $\epsilon \sim 45$, and $P_s = 50 \mu\text{C cm}^{-2}$, one calculates that a field of $E = 21 \text{ kV mm}^{-1}$ (the coercive field), the estimated wall energy is $\sigma_w \sim 35 \text{ mJ m}^{-2}$. This value compares well with the previous estimate of 10 mJ m^{-2} in Section 5.3.1 from domain wall birefringence. The critical nucleus size is $a^* \sim 22 \text{ \AA}$, and $l^* \sim 240 \text{ \AA}$. The depolarization energy $\sigma_p \sim 1365 \text{ mJ m}^{-2}$ which is much larger than σ_w as assumed in deriving Eq. (34). The term $0.5(a^*/l^*)^2$ is much less than unity as also assumed in deriving Eq. (34). The change in total energy ΔU^* is $\sim 99 \text{ kT}$. The relative contribution to ΔU^* from wall energy is about 3 times the contribution due to depolarization energy. In contrast, the wall energy [140] of BaTiO₃ is $\sim 0.42 \text{ mJ m}^{-2}$, which is 2 orders of magnitude smaller than the estimate for LiTaO₃. The critical nucleus size is $a^* \sim 360 \text{ \AA}$ and $l^* \sim 1600 \text{ \AA}$, which is an order

of magnitude larger than the corresponding critical nucleus size for LiTaO₃. The coercive field for BaTiO₃ is about 3 orders of magnitude smaller than the coercive field for congruent LiTaO₃. Zhu et al. [143] measured the activation field for switching times in LiTaO₃ as $\sim 0.1 \text{ MV mm}^{-1}$, which is an order of magnitude smaller than the activation fields measured for congruent LiTaO₃ crystals in the study by Gopalan and Mitchell [134]. However, no wall velocity measurements were made in the former report. One of the main differences between these studies is that LiTaO₃ crystals used in the study by Zhu et al. exhibited coercive fields of $\sim 13 \text{ kV mm}^{-1}$ or less, while the congruent crystals used in the study by Gopalan et al. exhibited coercive fields of $\sim 21 \text{ kV mm}^{-1}$. Since the near-stoichiometric LiTaO₃ crystals have coercive fields of $\sim 1.7 \text{ kV mm}^{-1}$ which is one-thirteenth of the coercive field for the congruent crystals, [Fig. 21] the crystals in Zhu's study [143] therefore appear to be of a composition between stoichiometric and congruent LiTaO₃. The estimated wall energy is also lower by an order of magnitude for these crystals, which is consistent with the observations that domain wall birefringence and strain decrease as the crystals get closer to stoichiometric compositions, as discussed in Section 4.3.2. These facts combine to suggest that the observed activation fields for switching times, and wall velocities should also be strongly nonstoichiometry dependent. Indeed, activation fields in stoichiometric crystals of LiTaO₃ are of the order of $\sim 18 \text{ kV mm}^{-1}$ which would yield wall energies consistent with that for BaTiO₃. These results are discussed in detail in Section 5.4

5.2.4. Real-time Studies of Domain Kinetics

The previous section on domain kinetics in LiTaO₃ were performed partly ex situ in the sense that constant voltage pulses were applied to the crystal to nucleate and to grow domains, and the evolution process was separately monitored after every pulse by optical observation under a light microscope [134]. The electrical field application and optical observation steps were separated. This methodology was also employed for measuring the domain wall mobility data by pulse voltage experiments reported in the literature for other ferroelectrics [144, 146]. This ex situ technique underestimates the wall velocities by an order of magnitude in congruent LiTaO₃. The second important phenomena which escaped careful observation by pulse voltage experiments is that merging of sideways growing domains results in an order of magnitude increase in the velocity of the serrated domain wall front that forms on merger.

By using real-time optical imaging, the constant voltage applied throughout the nucleation, growth, and merger of domains provides a contrast at the 180° walls through the electro-optic effect which is recorded on video. Importantly, it also eliminates having to apply pulse voltages to arrest domain growth for ex situ observation, thus eliminating possible reversible domain motion or domain wall pinning. The imaging also relies on the index difference at a domain wall due to the electro-optic effect, which is nondestructive, unlike acid etch techniques used previously [144–146]. Analyzing the video-data frame-by-frame, one can also monitor the kinetics of merging domains.

The electro-optic effect in noncentrosymmetric crystal structure produces a refractive index change (n_{ij}) in the material in response to an externally applied electric field (E_k) as

$$\Delta\left(\frac{1}{n_{ij}^2}\right) = r_{ijk}E_k \quad (35)$$

Since the electro-optic coefficients, r_{ijk} , form a tensor, the index change is dependent on the orientation of the crystal with respect to an applied electric field. As an example, let us consider a 180° ferroelectric domain wall in a uniaxial crystal such as LiTaO_3 (3m, C_{3v}). Under a uniform electric field E , the refractive index in one domain increases from $n \Rightarrow n + \Delta n$, while it decreases in the other from $n \Rightarrow n - \Delta n$, thus providing an index contrast across the domain wall. In LiTaO_3 , $r_{113} = r_{223} \sim 8.4 \text{ pm/V}$ (at 633 nm) [147] and therefore, under a field $E_3 \sim 21 \text{ kV mm}^{-1}$ (coercive field of congruent LiTaO_3) in the z -direction, one obtains a $\Delta n_{11} = \Delta n_{22} = 9.1 \times 10^{-4}$, where index increases in the domain where the external field is antiparallel to the direction of spontaneous polarization. Since the domain wall in congruent LiTaO_3 is perpendicular to the crystallographic y -direction, when one crosses the domain wall, this index difference Δn_{22} at the wall causes a scattering of the transmitted light in the crystal. This can be used to image a domain wall through the crystal thickness in a z -cut crystal under an optical microscope without any polarizers.

In addition to this contrast mechanism, birefringence ($n_{11} - n_{22}$) exists at the domain walls in congruent LiTaO_3 even without the presence of any external electric field which was shown to be related to the presence of internal fields and therefore to the lithium nonstoichiometry of the crystals [77]. This birefringence cannot be obtained from linear electro-optic effect since $r_{13} = r_{23}$. However, as shown in Section 4.3.1, a combination electrostriction, photoelasticity, and quadratic electro-optic effect gives rise to a birefringence ($n_{11} - n_{22}$) which has cross-terms proportional to E_2E_3 [82]. Since E_2 at the wall is now nonzero, an applied field E_3 along the z -axis can increase or decrease the birefringence at the wall linearly as seen in Figure 40 [82].

In any case, the domain walls studied in congruent LiTaO_3 are visible in plain transmitted light, both with and without cross-polarizers, and both with and without external electric field E_3 . However, the presence of a Nomarski slider (also called differential interference contrast) along with cross-polarizers considerably improves this contrast. Using this contrast mechanism, one can directly study the movement of 180° domains in ferroelectric LiTaO_3 under an external electric field. The schematic of an electro-optic imaging setup used by Gopalan et al. [133] is shown in Figure 57. In this study, the holder for applying voltage was specially designed to trap the liquid electrode columns on either side of the crystal with transparent glass slides. The entire holder assembly was readily insertable in a regular optical microscope in

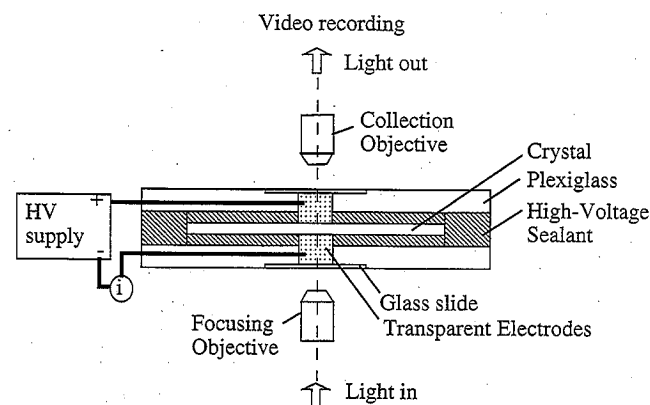


Fig. 57. A holder used for imaging ferroelectric domains in LiNbO_3 and LiTaO_3 using electro-optic contrast at domain walls. V. Gopalan and T. E. Mitchell, *J. Appl. Phys.* 85, 2304 (1999).

transmission mode, where light propagated through a first glass slide, the liquid electrode, the crystal, the second liquid electrode, and the second glass slide in succession, before being collected by a $4\times$ objective. The electrode area was a circle of 4-mm diameter. However, the imaging area on the video screen after magnification was only $0.97 \times 0.73\text{-mm}$ square situated at the center of the electrode area. The imaging was performed in transmission using cross-polarizers in combination with a Nomarski objective. With this setup, the transient current measurement during domain reversal and the optical observation of the evolving domain structures were monitored simultaneously. The video recording was performed with a digital camera, and a regular VCR with 30 frames per second. The recorded film was digitized using a video card and software on a Power Macintosh, through which every frame could be extracted. The final resolution was $\sim 6 \times 6 \mu\text{m}$ pixel size, and 160×120 -pixels image space.

Domain kinetics was studied under two applied electric-field conditions: (a) steady-state voltage application; (b) pulsed voltage application. In the steady-state voltage studies, a constant voltage was applied to the sample through the entire period of domain switching time. In pulsed voltage studies, a series of voltage pulses were applied through the switching process, each pulse resulting in a partial reversal of domains under the electrode area. In both these studies, in situ video observation was used to study domain kinetics using Electro-optic Imaging Microscopy (EOIM), in contrast to ex situ measurements reported in Section 5.2.3.

5.2.4.1. Domain Kinetics under Steady-State Fields

The following experiments performed by Gopalan and Mitchell [133] were on five different pieces of one wafer, labeled F. All the studies reported in this study corresponded to the first domain reversal of a crystal in the virgin state, called the forward poling [133]. The process of domain reversal was observed in situ at constant electric-field values applied as voltage steps. The samples were denoted as F207, F208, F210, F212, and F214 corresponding to electric fields of 206.9 kV cm^{-1} , 207.6 kV cm^{-1} , 210.0 kV cm^{-1} , 212.0 kV cm^{-1} , and 214.0 kV cm^{-1} , respectively. Simultaneous measurement of the transient current data along with the electro-optic imaging of the domain-inversion process was performed.

As an example, Figure 58 shows a series of frames obtained from the electro-optic imaging data for the F208 sample. Only a



Fig. 58. Selected video-frames from in situ recording of the nucleation and growth of 180° domains in congruent LiTaO_3 under an external field of 207 kV cm^{-1} (applied at $t = 0$ s) using electro-optic imaging. Frame (a) corresponds to $t = 30$ s, and all successive frames [(b)–(o)] are 15 s apart from each other. The polarization axis is normal to the image plane. The independently growing domains, (I–IV) and three merged domain fronts (V, VI, VII) for which domain mobilities were measured, are labeled. The arrows in frame (e) and (g) indicate the location and direction of the wall velocity measurement for the merged domains, V, VI, and VII. V. Gopalan et al., *J. Appl. Phys.* 86, 1638 (1999).

selective collage of frames is shown in the figure although we could extract 30 frames per second from the video from the start of the voltage pulse to the end of domain reversal process. If the step voltage was applied at time $t = 0$, the first frame (a) in Figure 58 corresponds to $t = 30$ s. Every successive frame is spaced by 15 s and named (b), (c), (d), etc. The final frame is Figure 58(o) and corresponds to $t = 240$ s. The polarization axis is normal to the plane of image. The 180° domains nucleate and grow in the form of triangular domains with domain walls perpendicular to the mirror plane (for example, domains I–IV shown in Figure 58(c) and (d)). The crystallographic y -axis corresponds to $[1100]$ and lies in the c -glide plane. Eventually, the domains merge sideways and form a merged domain front like the domains V–VII indicated in Figure 58(e) and (g). The arrows indicate the location and direction of sideways velocity measurement of these fronts, the results of which are presented in the next section.

The resolution with which one could estimate the position of the walls was within ~ 3 pixels. Assigning the bottom left-hand corner of every frame as pixel coordinate (0, 0), the origin of the triangular domains was determined. For example, domain I originates at $O_I(45, 17)$ at a nucleation time, $t_N = 21.83$ s and the origin of

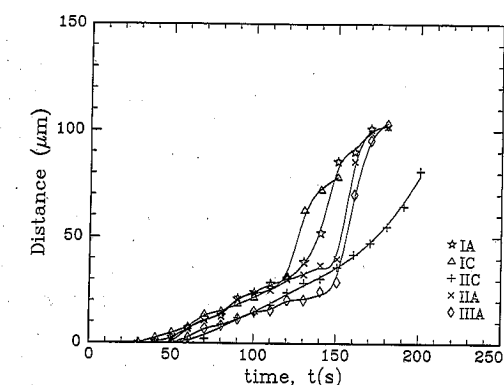


Fig. 59. The sideways movement of some representative 180° domain walls from Figure 58 (sample F208) as a function of time after application of a steady-state electric field ($E_f = 207.6 \text{ kV cm}^{-1}$) at $t = 0$ s. The notation IA, for example, stands for the measurements on side A of domain I in Figure 58. The solid lines are drawn as guides to the eye. V. Gopalan et al., *J. Appl. Phys.* 86, 1638 (1999).

domain II is $O_{II}(118, 44)$ at $t_N = 37.13$ s. The three domain walls of each of the triangular domains I were labeled as IA, IB, and IC as follows. Referring to the crystallographic x - and y -axes in Figure 58(a), the wall A is perpendicular to the y -axis, and B and C follow anticlockwise around the triangle from wall A.

The average distance travelled by each of the walls from the origin, O , in a direction normal to the wall was measured. As a representative example, Figure 59 shows the wall velocity for a number of walls in sample F208. In the initial stages after nucleation, the walls appear to move at a steady-state sideways velocity as seen from the linear part of the distance-time curves in Figure 59. However, around ~ 120 s after the start of the voltage step, the walls appear to show sharp rises in velocity indicating a speeding up process. This is the first indicator of the presence of two regimes in sideways wall velocity of moving domains: First is the lower steady-state velocity ($v_{s,f}$) of independently growing triangular domains such as domains I–IV where subscript s stands for sideways velocity and subscript f for forward poling. However, when these domains start merging with neighboring domains, they form serrated domain fronts such as V–VII which move with a higher steady-state velocity ($v_{s,fm}$) where the subscript m stands for a merged front. The sudden increases in the velocity of the individual domain walls in Figure 58 correspond to discrete merging events. For example, referring to Figure 58, domain I is growing independently until approximately frame 3(g) ($t = 12$ s), when it merges with two other domains. These two mergers around 120 s are reflected in the rise in velocities of edges IA and IC in Figure 58.

The distance moved versus time after nucleation of some representative walls in the independently growing domains is plotted in Figure 60 showing that, at a field 207.6 kV cm^{-1} , the sideways velocity of independently growing domain walls is $\sim 0.32 \mu\text{m s}^{-1}$. To measure the increased velocity of merging domains, we chose the merged domain fronts V–VII. Choosing an arbitrary point behind the moving front as the origin, we measured the velocity of these fronts at various points along the front as shown by arrows in Figure 58(e) and (g). The results are plotted in Figure 61, showing that they move at a higher steady-state velocity of $\sim 1.8 \mu\text{m s}^{-1}$.

Similar measurements of sideways domain wall velocity ($v_{s,f}$) of independently growing domains and of merged domain fronts ($v_{s,fm}$) were also performed for samples F207, F210, and F212.

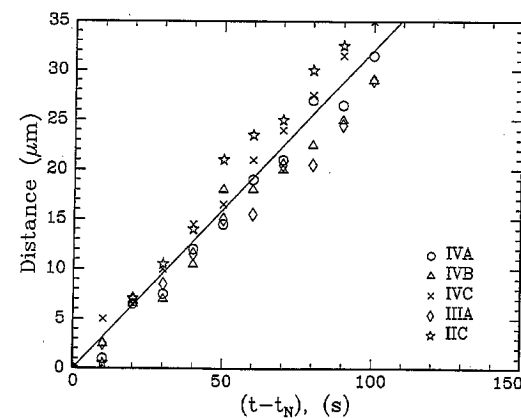


Fig. 60. The initial sideways movement of some representative 180° domain walls of independently growing domains III and IV in Figure 58 (sample F208) as a function of time t under an external electric field $E_t = 207.6$ kV cm^{-1} applied at $t = 0$ s. The solid line is a straight line fit. The nucleation time t_N of domains II, III, and IV were 37.13 s, 48.23 s, and 59.83 s, respectively. The average sideways velocity is $v_{s,f} \sim 0.32$ $\mu\text{m s}^{-1}$. V. Gopalan et al., *J. Appl. Phys.* 86, 1638 (1999).

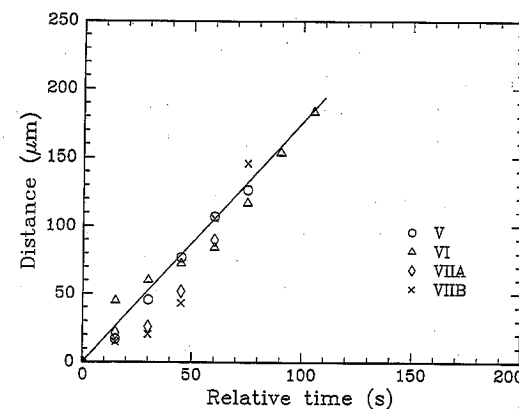


Fig. 61. Sideways movement of merged domain fronts V, VI, and VII in Figure 58 (sample F208) under an external electric field of 207.6 kV cm^{-1} . The average velocity of the front is $v_{s, fm} \sim 1.8$ $\mu\text{m s}^{-1}$. The solid line is a straight line fit. The data VIIA and VIIB denote two measurements along the pair of arrows on domain front VII shown in frame (g) of Figure 58. V. Gopalan et al., *J. Appl. Phys.* 86, 1638 (1999).

These velocity measurements are plotted in Figure 62 as a function of applied electric field on a semilog plot to illustrate the relation given in Eq. (31). Defining two activation fields $\alpha_{s,f}$ and $\alpha_{s, fm}$ for independently growing domain wall velocity and merged front velocity, respectively, the measured values from Figure 53 are $\ln(v_{s, fo}, \text{cm s}^{-1}) = 203.9 \pm 25.3$ and $\alpha_{s,f} = 35,200 \pm 4200$ kV cm^{-1} for independently growing domains, and $\ln(v_{s, fmo}, \text{cm s}^{-1}) = 237.8 \pm 20$ and $\alpha_{s, fm} = 40,500 \pm 3300$ kV cm^{-1} for merged domain fronts. These values of activation field are higher than the values for $\alpha_{s,f}$ reported earlier using pulsed voltage experiments followed by ex situ observation as shown in Table VI [134]. The actual magnitude of $v_{s,f}$ is significantly higher by an order of magnitude over previously reported results using pulsed voltage experiments. The merged front velocity is even higher. We discuss these further in Section 5.2.6.

The numbers of independent nucleation events (N_f) in the video-area recorded as a function of time and are shown in Fig-

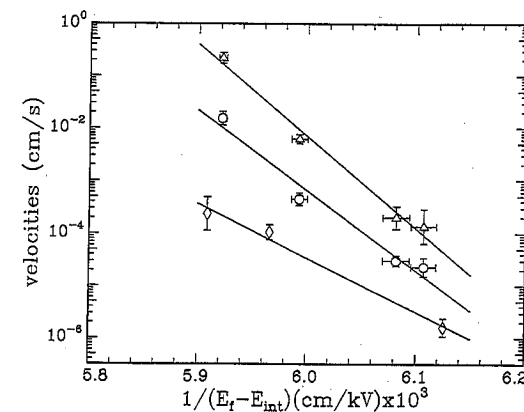


Fig. 62. The sideways wall velocities of 180° domain walls in congruent LiTaO_3 as a function of electric field, E_f , measured using EOIM. The velocities $v_{s,f}$ of independently growing domains in wafer F is shown in circles and velocities $v_{s, fm}$ of merged domain fronts in wafer F as triangles. The sideways velocity $v_{s,f}$ from wafer B measured in Ref. 128 (see Fig. 56 using pulsed voltage application followed by ex situ observation is also shown for comparison as rhombuses. The solid lines are straight line fits. The internal field E_{int} is 44.15 kV cm^{-1} for wafer F and 42.20 kV cm^{-1} for wafer B. V. Gopalan et al., *J. Appl. Phys.* 86, 1638 (1999).

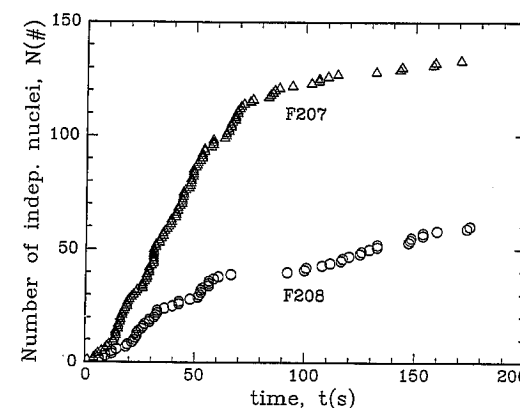


Fig. 63. The total number, N , of independently nucleating 180° domain nuclei as a function of time in the observation area (0.97×0.73 mm^2) of EOIM for (a) samples F207 ($E_f = 206.9$ kV cm^{-1}) and F208 ($E_f = 207.6$ kV cm^{-1}), and (b) samples F210 ($E_f = 210.0$ kV cm^{-1}), and F212 ($E_f = 212.0$ kV cm^{-1}). The fields were applied at time $t = 0$ s. Solid lines in (b) are straight line fits with the dotted line showing the saturation. V. Gopalan et al., *J. Appl. Phys.* 86, 1638 (1999).

ure 63(a) and (b). By independent nucleation events we mean those nuclei which nucleate in the original domain matrix independent of the presence of other domains around them. This would, for instance, preclude nucleation at a domain wall or on a merged front. The typical trend for this curve at all the fields studied here is an initial linear increase in the number of independent nuclei followed by a saturation where few new independent nucleations take place. This saturation value is denoted N_{sat} . The initial nucleation rate (N_f) and the saturation value of the number of nuclei (N_{sat}) for the video-area is plotted as a function of field in Figure 64. The saturation number of nuclei, N_{sat} , decreases with increasing field as expected. However, the initial nucleation rate appears to show a small initial decrease before increasing with increasing field. These features are discussed further in Section 5.2.6.

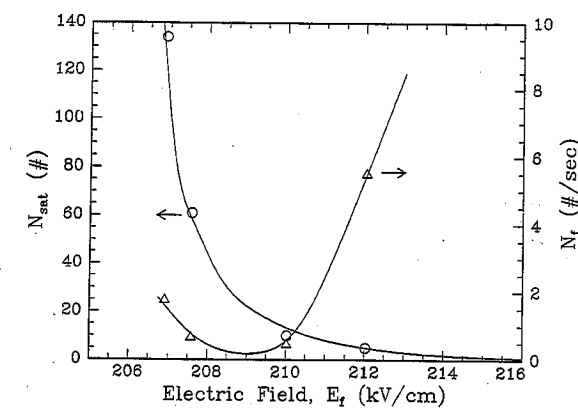


Fig. 64. The initial nucleation rate N_f (triangles) of independently nucleating 180° domains and the saturation number N_{sat} (circles) of domains as a function of electric field, E_f , measured from the data of Figure 63. Solid lines are drawn as a guide to the eye. The arrows indicate the relevant axes for the plots. V. Gopalan et al., *J. Appl. Phys.* 86, 1638 (1999).

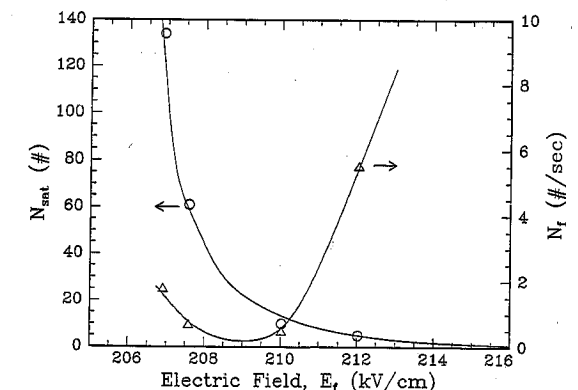


Fig. 65. Area fraction, x , of growing 180° domains (sample F208) resulting from (a) integrating the current pulse shown as solid line, and (b) from the total area of the growing domains from EOIM images in Figure 58, shown as circles. V. Gopalan et al., *J. Appl. Phys.* 86, 1638 (1999).

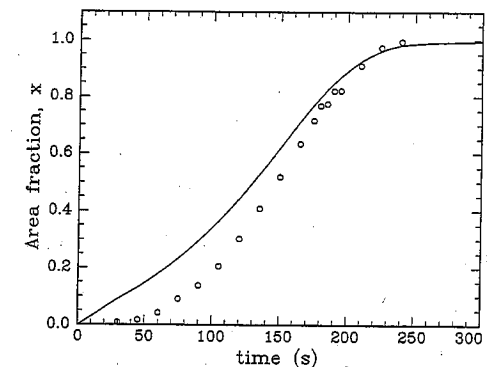


Fig. 66. The area fraction x of domain inverted region as a function of time for samples F207 (circles; $E_t = 206.9$ kV cm^{-1} , F208 (triangles; $E_f = 207.6$ kV cm^{-1}), F210 (xs; $E_f = 210.0$ kV cm^{-1}) and F212 (rhombuses; $E_t = 212.0$ kV cm^{-1}). The data are plotted such that the slope of the curves gives the Avrami exponent, n from Eq. (36). V. Gopalan et al., *J. Appl. Phys.* 86, 1638 (1999).

$\ln(\ln(1/(1-x)))$ versus t , one obtains the slope of the curve as the Avrami exponent, n . The video-data for all the fields are plotted in this form in Figure 66. For samples F207 and F208 with low fields, the Avrami exponent is 2.95 and 3.1, respectively, which is close to 3 as predicted by Eq. (36). However at higher fields, this exponent is continuously increasing with time and has a value of ~ 11 for the F212 sample ($E = 212$ kV cm^{-1}).

Figure 62 clearly shows that the independent domain wall velocities measured by EOIM are an order of magnitude larger than those measured earlier by pulsed voltage measurements followed by ex situ optical observation [134]. To investigate the reason for such behavior, pulsed voltage experiments on a sample F13 was performed from the same wafer F in combination with EOIM observation.

5.2.4.2. Pulsed Voltages Studies

The pulsed voltage experiment was performed at an electric-field value of 212 kV cm^{-1} which corresponds to the same field as sample F212, and therefore provides a comparison. Since the switching time at 212 kV cm^{-1} was ~ 1 s, voltage pulses of 300-ms width were chosen for application. However, since the stabilization time for 180° domains at room temperature is ~ 1.5 – 2 s, and therefore, a 300-ms pulse would result in a completely reversible domain wall motion and result in no net change in domain microstructure. Therefore, a baseline field of 205 kV cm^{-1} was chosen for the pulse similar to that shown in Figure 54(b). This baseline was chosen quite arbitrarily as a field value below the coercive field at which no domain wall motion was observed over many hours; the domain wall motion is therefore arrested at the end of the 300-ms pulse. This is seen from the transient current response which goes to zero after the 300-ms pulse. However, the baseline field, which stays on for 10–20 s after the pulse, allows the domain stabilization process to occur.

Figure 67 shows the movement of the three sides of an independently growing domain upon application of voltage pulses as described earlier. Four of those voltage pulses (field of 212 kV cm^{-1} , 300-ms width each) are shown. The start of each pulse is shown by an up arrow and the end (300 ms) is shown by a down arrow along the time axis. After the end of the 300-ms pulse, the baseline

The area fractions (x) of inverted domain regions as a function of time was measured from the video-data of Figure 58. This is shown for sample F208 in Figure 65. Also shown for comparison is the area-fraction data derived from integrating the transient current. It is seen that the area-fraction obtained from the transient current shows the beginning of nucleation and growth well before it is reflected in the video-data. This suggests that nucleation has slight preference at the electrode edges where there is a higher density of field lines due to fringing fields. This effect is observed in all the samples [for example, see Ref. [111] for data on sample F212]. Since the video-area is only $\sim 0.97 \times 0.73$ mm^2 at the center of the electrode region (4π mm^2), the edge effects are excluded in the video-data.

The Avrami nucleation and growth model [148] gives the area fraction x of growing triangles as a function of time t as

$$x = 1 - \exp(-Kv_s^2 N_f t^N) \quad (36)$$

where K is a constant, v_s is the (assumed) constant steady-state velocity, and N_f is the rate of nucleation per unit area. A two-dimensional model for triangular growth gives $K = \sqrt{3}$ and the Avrami exponent $n = 3$. Replotting the data in Figure 65 as

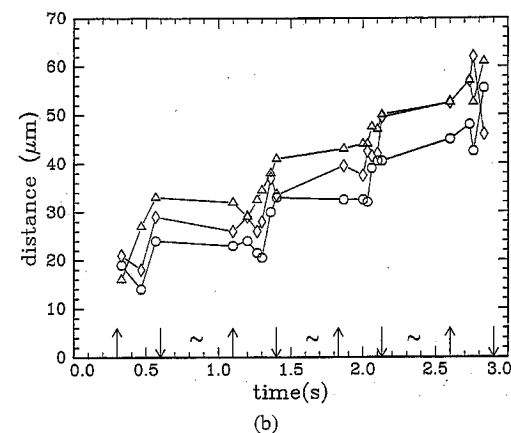
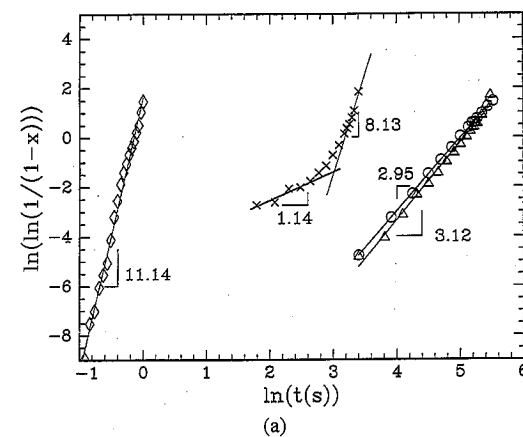


Fig. 67. The sideways movement of domain walls in independently growing 180° domains as a function of time upon application of voltage pulses similar to that shown in Figure 54(b). The movement of three sides of a triangular domain (shown by circle, triangle, and rhombus) in response to four successive pulses is shown. The start of a pulse is marked by an up arrow, and the end of the 300-ms pulse by a down arrow. The "///" signs between the pulses indicates a time lapse of 30–40 s. V. Gopalan et al., *J. Appl. Phys.* 86, 1638 (1999).

voltage was on for another 5–10 s, following which it was lowered to zero voltage. The time elapsed between independent pulses was 30–40 s as indicated by "///" signs between the pulses.

One can make some significant observations in Figure 67:

(a) The resolution with which the movement of the domain wall is tracked is a pixel ($\sim 6 \mu\text{m}$). Therefore one cannot make conclusions about any significant backtracking of a domain wall after each pulse.

(b) A common trend is that the movement of a domain wall within a 300-ms pulse is negligible for the most part of the pulse (50–90% of pulse width) followed by some significant movement near the very end of the pulse. By monitoring the voltage directly across the sample, the measured rise time was ~ 350 ns (much smaller than pulse width), thus confirming that the initial delay in domain wall movement is not due to pulse rise time.

(c) In all, ~ 18 pulses were required to completely reverse the domain under the electrode area which implies a switching time of ~ 5 –6 s. This is 5–6 times the switching time measured with a steady-state voltage. The switching time here is defined as the time required to completely reverse the domain under the electrode area as observed by EOIM.

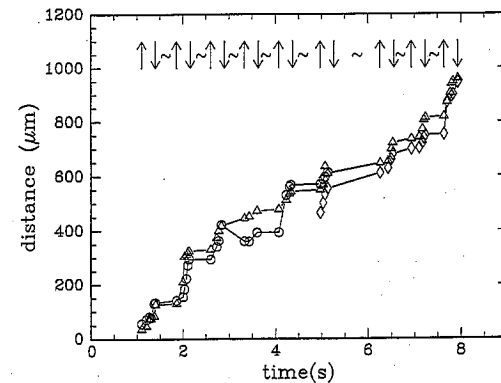


Fig. 68. The sideways movement of merged 180° domain fronts as a function of time upon application of voltage pulses as shown in Figure 54(b). The movement of the domain front at three different points along the front is shown by triangles, circles, and rhombuses. Each applied pulse was 300-ms long. The start of a pulse is marked by an up arrow, and the end of the pulse by a down arrow. The "///" signs between the pulses indicates a time lapse of 30–40 s. V. Gopalan et al., *J. Appl. Phys.* 86, 1638 (1999).

(d) The average velocity of a domain wall during each pulse as calculated by the net movement of the wall during the period of the pulse divided by the pulse width (300 ms) was measured to be $\sim 34 \mu\text{m s}^{-1}$. This value is also consistent with earlier measurement of $\sim 10 \mu\text{m s}^{-1}$ for sideways velocity of domains in wafer B (Fig. 56) for the same switching time of 1 s under a steady field.

Similar measurements were made for merged domain fronts with pulsed voltage application. Figure 68 shows the movement of a merged domain front made at three different locations along the front with application of voltage pulses. The average velocity of the merged front as measured by the net distance moved by the front during a pulse divided by pulse width (300 ms) was measured to be $\sim 340 \mu\text{m s}^{-1}$. We discuss these observations in Section 5.2.6.

5.2.5. Local Pinning and Bowing of a Ferroelectric Domain Wall

In addition to macroscopic domain wall motion under electric fields larger than the coercive field, Yang et al. [82] also observed that domain wall motion is possible at fields only a tenth of the coercive field in congruent LiTaO_3 . This motion is the submicroscopic bending of the domain wall between pinning sites. This provides the first direct evidence that coercive fields reported for many ferroelectrics may correspond to a pinning-depinning transition of domain walls.

The collection mode (near-field scanning optical microscope) CMNSOM [149] with a spatial resolution around a fifth of an optical wavelength is ideally suited for studying domain walls under uniform applied fields. A schematic of the experimental setup was shown in Figure 37. Light transmitted through the crystal is collected with an aluminum coated fiber probe (aperture < 100 nm and maintained < 5 nm from the surface) and its polarization rotation is measured. Yang et al. [82] performed the experiments on the room-temperature 3 m ferroelectric phase of congruent LiTaO_3 . Single domain crystals cut perpendicular to the c -axis (spontaneous polarization axis) and of 0.5-mm thickness were used. Crystal surfaces of optical polish were used. In the original single domain crystal, the internal field from the lithium de-

ficiency is oriented parallel to the spontaneous polarization direction through a poling process done at 600°C . Then 180° domains are created at room temperature with an external electric field. This room-temperature domain reversal process leaves the internal field due to the lithium nonstoichiometry in a frustrated state. Therefore, across domain walls studied here, while the spontaneous polarization rotates by 180° , the orientation of internal field remains the same [79]. A 20-nm semitransparent 60% Au+40% Pd electrode was sputter deposited on the top and bottom surfaces of the crystal. The bottom electrode and fiber probe are grounded. Both positive and negative voltages are applied to the top electrode.

In the experiment the fiber probe is first placed and maintained in the near-field (< 5 nm) of the crystal surface using the shear force technique [81]. Linear polarized light from an argon ion laser is passed through a half-wave plate (to change incident polarization) and is incident normally on the top surface of the crystal. The transmitted light collected by the fiber probe at the bottom surface is collimated and passed through a half-wave plate and a quarter-wave plate which are set to compensate for fiber birefringence. The light is then passed through an analyzer and is collected by a cooled Photomultiplier tube (PMT). At the start of the scan, the analyzer is rotated to null the transmitted light in a region away from the domain wall (region of isotropic refractive index). The background signal under crossed polarizers is measured and subtracted from all images. A 13×13 -m scan of the crystal surface around the birefringent domain wall is then made.

Figure 69(a) is a single 180° domain wall observed with both electrodes grounded. The incident light polarization was 70° to the domain wall. The FWHM of the birefringent region is $3 \mu\text{m}$. The large width of the birefringence is due to internal fields generated by defects pinning the domain wall. The width of the birefringent region in these samples range from less than 100 nm (instrument resolution limit) to a few microns [81, 82]. The dark feature $1.0 \mu\text{m}$ from the right and $5 \mu\text{m}$ from the bottom is due to a defect in the electrode which can be used as a position reference. From the reproducibility of optical features on repeated scans of the same region, the resolution is estimated to be ~ 150 nm. Next voltages in steps of $+100$ V are applied to the top electrode. Figure 69(b) shows the optical signal corresponding to the domain wall at an applied field of $+1.5 \text{ kV mm}^{-1}$. The bottom of the domain wall (shown by an arrow) is observed to have moved a distance of $3 \mu\text{m}$. Figure 69(c) is the optical signal at an applied electric field of $+2 \text{ kV mm}^{-1}$. From Figure 69(b) and (c) we observe that the domain wall has not moved but appears to be pinned at two points (shown by open circles X and Y). The pinning points are identified by their increased birefringence and the change in curvature of the domain wall around them. The exact nature of these pinning defects is not known at present, but they are believed to be physical defects such as dislocations or localized variations of point defects [134]. The increased birefringence at the pinning defects results from the associated fields and strains of these defects. Such bending of the domain walls around pinning defects was predicted in ferroelectric materials [150]. Next, the applied voltages on the top electrode is brought to zero and the domain wall was found to relax back to its original position as in Figure 69(a). Then negative voltages in steps of -100 V are applied to the top electrode. The domain wall at an applied electric field of -1.8 kV mm^{-1} is shown in Figure 69(d). Comparing to Figure 69(a), no movement of the domain wall is observed. Instead the birefringence (width and magnitude) at the domain wall

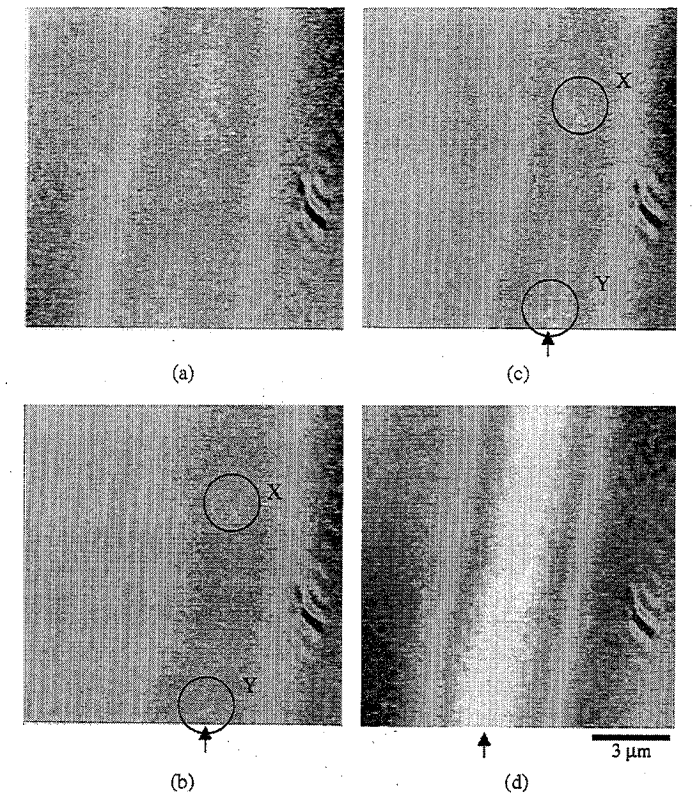


Fig. 69. CMNSOM optical signal around the 180° domain wall at applied fields of (a) 0 and (b) $+1.5 \text{ kV mm}^{-1}$ (c) $+2.0 \text{ kV mm}^{-1}$, (d) -1.8 kV mm^{-1} . The arrow identifies the bottom of the domain wall. The open circles X and Y in (b) and (c) identify pinning defects from the increased birefringence (brightness) and curvature of the domain wall. Reprinted from T. J. Yang et al., *Ferroelectrics*, 222, 609, (© 1999 Gordon & Breach); T. J. Yang et al., *Phys. Rev. Lett.*, 82, 4106, (© 1999 American Physical Society).

was observed to increase with increasing magnitude of the applied field. This asymmetry in domain wall motion with voltage polarity is consistent with the internal electric-field orientation which is parallel (antiparallel) to the spontaneous polarization to the left (right) of the domain wall. This is consistent with measurements of coercive field of 21 kV mm^{-1} (11 kV mm^{-1}) for domain movement to left (right) in congruent LiTaO_3 crystals.

From the profile of the pinned domain wall in Figure 69(b) and (c), the authors approximately estimate the domain wall energy based on a simple two-dimensional model shown in Figure 70. Let $y = g(x)$ represent a domain wall between two pinning sites $P_1(0, 0)$ and $P_2(d, 0)$ such that $g(0, 0) = g(d, 0) = 0$. Under an externally applied field E , the free energy change (ΔU) per unit thickness associated with the domain wall is

$$\Delta U(g) = -2P_s E \int_0^d g(x) dx + \sigma_w \int_0^d \sqrt{1 + \left(\frac{\partial g(x)}{\partial x}\right)^2} dx \quad (37)$$

where P_s is the spontaneous polarization and σ_w is the domain wall energy per unit area. The depolarization energy and the anisotropic elastic coupling are neglected in this two-dimensional model. The first term is the lowering of the electrostatic free energy by bending of the domain wall, and the second term is the increase in free energy due to increased wall length. For a material (constant P_s) at electric field E , the shape is given by the

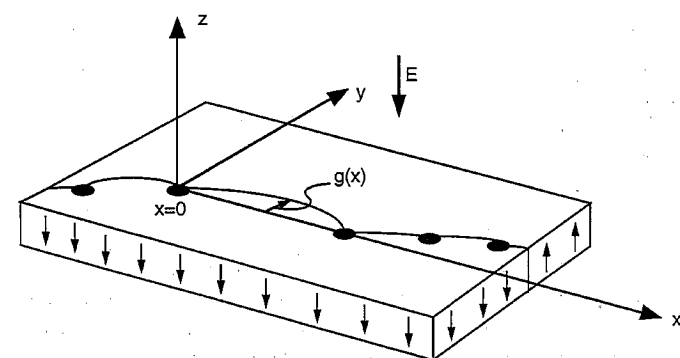


Fig. 70. Schematic of a bowed domain wall pinned by defects (dots) with an applied electric field E . Reprinted from T. J. Yang et al., *Ferroelectrics*, 222, 609, (© 1999 Gordon & Breach); T. J. Yang et al., *Phys. Rev. Lett.*, 82, 4106, (© 1999 American Physical Society).

Euler-Lagrange equation and one obtains [82]

$$g(x) = \pm \left\{ \sqrt{\left(\frac{\sigma_w}{2P_s E}\right)^2 - \left(x - \frac{d}{2}\right)^2} - \sqrt{\left(\frac{\sigma_w}{2P_s E}\right)^2 - \left(\frac{d}{2}\right)^2} \right\} \quad (38)$$

Hence $g(x)$ is the circle segment of radius $R = \sigma_w/(2P_s E)$. This implies that the domain wall curvature is unique for a given material at a fixed electric field E , independent of the distance between pinning sites. From the profile of the domain wall between the pinning sites in Figure 69(c) the radius of curvature is measured to be between 6–12 μm (inexactness due to the diffuse nature of the left edge) giving a domain wall energy per unit area of $\sigma_w = 0.2\text{--}0.4 \text{ J m}^{-2}$. This is higher than the previous estimates of 10–30 mJ m^{-2} in Sections 4.3.1 and 5.2.3. The order of magnitude difference primarily comes from the larger width of the birefringence region in the pinning studies presented in this section. Since regions of birefringence were observed to vary from 100 nm to many microns, this is reflected in an order of magnitude difference in wall energies as seen here. Nonetheless, they are all consistently at the higher end of some theoretical estimates of 0.1–0.01 J m^{-2} for BaTiO_3 [151, 152].

5.2.6. Discussion of Domain Kinetics Results in Congruent LiTaO_3

5.2.6.1. Sideways Wall Velocity

The sideways velocity of 180° domains made under steady-state electric field of 212 kV cm^{-1} was $\sim 200 \mu\text{m s}^{-1}$ for independently growing domains and $\sim 2300 \mu\text{m s}^{-1}$ for merged domain front. In contrast, the same measurement made using a pulsed voltage experiment at 212 kV cm^{-1} showed a velocity of $\sim 34 \mu\text{m s}^{-1}$ for independently growing domains and $\sim 340 \mu\text{m s}^{-1}$ for merged domain fronts. The switching time also increases from $\sim 1 \text{ s}$ under the steady-state electric field to $\sim 5\text{--}6 \text{ s}$ under the pulsed voltage application at 212 kV cm^{-1} .

Therefore, two questions arise. First, why does the pulsed voltage measurement result in an underestimation of steady-state sideways velocity of both independent and merged domain fronts by an order of magnitude? Second, why is a merged domain front faster than independently growing domains by an order of magnitude?

Two possible explanations exist in answering the first question. One possibility is that there might be a considerable backtracking or “inertial recoil” of a moving 180° domain wall at the end of a voltage pulse. The data in Figures 67 and 68 show that this inertial recoil, if any, has to be much less than a pixel movement ($\sim 6 \mu\text{m}$) and is therefore not the predominant reason for the observed discrepancy in velocity measurements by steady-state and pulsed voltage measurements. The second possibility is that there exists an incubation period of as much as 90% of the pulse width during which time there is negligible movement of the domain wall. This explanation is borne out by the data in Figure 68 which shows that indeed most of the movement occurs only toward the end of the pulse. The most plausible explanation for the incubation period required for the movement of a domain wall from rest is that, when a domain wall comes to rest for a long time (much longer than the stabilization time of 1–2 s), it is stabilized by elastic and electrostatic relaxation of the lattice near the domain wall in response to the interaction of point-defect complexes with the spontaneous polarization. This would therefore suggest that the time scale of the measurement of domain kinetics in congruent LiTaO_3 in particular, and similar ferroelectrics in general, is crucial in interpreting the domain wall mobility data reported in the literature.

The second question pertaining to the increased wall velocity of a merged domain front results from the formation of ledges upon domain merger. Based on simple energetics arguments, it can be shown that the activation energy for nucleation at a ledge is lower than that for nucleation at a flat wall on the sides of an independently growing domain. Figure 71 shows a schematic of the intersection of two growing 180° domain triangles to form a ledge. Following the argument of Miller and Weinrich [142] further growth of domain walls will occur by preferential nucleation at the domain wall. Assuming that the nuclei also possesses the same triangular symmetry of the larger domains in the z -plane, one can write down the change in free energy (ΔU_{3D}) in three dimensions due to the formation of a nucleus as,

$$\Delta U_{3D} = -2 \cdot P_s E \cdot \Delta V_{3D} + \sigma_w \Delta A_{3D} + U_d \quad (39)$$

where P_s is the spontaneous polarization, E is the external electric field, ΔV_{3D} is the volume of the nucleus, σ_w is the wall energy per unit area, ΔA_{3D} is the change in wall area due to the nucleus, and U_d is the depolarization energy. The first term in the equation is the decrease in the volume electrostatic energy, the second term is the net increase in domain wall energy, and the third term is the increase due to depolarization energy.

First, consider the energy change ΔU_{2D} in a simple two-dimensional picture of a merger as shown in Figure 71(a). In this two-dimensional picture, we can for the moment ignore the depolarization energy, U_d in Eq. (2). The volume change, ΔV_{3D} , in Eq. (39) can accordingly be replaced by an area change, ΔA_{2D} , in the z -plane (plane perpendicular to the polarization axis), and the wall area change ΔA_{3D} can be replaced by the wall length change ΔL_{2D} . Comparing nuclei A and B (or C), one can immediately deduce that for a fixed area of the nuclei ΔA_{2D} , the domain length change $\Delta L_{2D} = 0$ for nucleus A and $\Delta L_{2D} > 0$ for nuclei B and C . Thus the energy change $(\Delta U_{2D})_A < (\Delta U_{2D})_B$ or $(\Delta U_{2D})_C$. In other words, in this two-dimensional picture, the formation of nuclei A lowers the electrostatic energy, but costs no additional energy for the formation of domain walls, since the net wall length remains the same. This is true for any nucleation at the ledge similar to nuclei A , but with various levels of raggedness to the wall front, as depicted, for example, by broken lines of wall A'

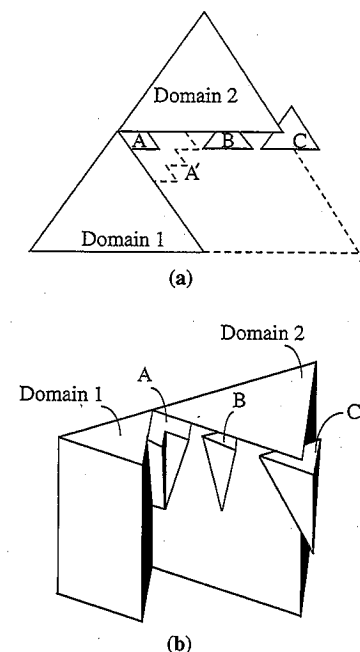


Fig. 71. A schematic considering possible nucleation sites upon merger in (a) a two-dimensional case and (b) three-dimensional case. Of the three possible nucleation sites, A , B , and C , nuclei A at the ledge is the most preferred since it involves no net change in domain wall length before and after nucleation. This nuclei will propagate out as a front A' with a higher sideways velocity until it reseach the larger triangle A'' . V. Gopalan, *J. Appl. Phys.* 85, 2304 (1999).

in Figure 71(a). This is however not true for nucleations at sites B or C , where there is a significant increase in the domain wall length. Thus, upon merger of triangular domain walls, ledges are formed at the intersection of these domains. These domains have a much stronger driving force for nucleation than the flat walls of an independently growing domain. The merged domain front in Figure 71(a) will speed up until it reaches the dotted line A'' , where the ledge disappears. Further growth from this point onward will be at a lower steady-state velocity as of domains I and II in Figure 58.

We must point out that in this two-dimensional case, $(\Delta U_{2D})_A = -2 \cdot P_s E \cdot \Delta A_{2D} < 0$. A steady-state velocity of the form $v_s \propto \exp(-(\Delta U_{2D})/kT)$, [142] is no longer physical since it would suggest that, at zero field, v_s is nonzero. Instead, a merged domain front such as A or A' should accelerate at a constant field under a force $-U/y$ where the coordinate y is normal to the domain walls. This is contrary to the observed steady-state velocity in Figure 61. Let us consider the more realistic three-dimensional case as depicted by Figure 64(b). The nuclei initially form daggers in the thickness direction of the z -cut crystal. The net area change of the domain wall, ΔA_{3D} , is not exactly zero for nucleus A anymore since the new wall segments are not necessarily parallel to the old walls in the planes parallel to the polarization direction. Further, one can no longer neglect the depolarization energy U_d in Eq. (39). However, one still retains the essence of the argument presented for the two-dimensional case if the dagger shaped nuclei have a very large aspect ratio, i.e., much longer in the polarization direction than they are wide in the z -plane. This implies that ΔA_{3D} , though finite, is very small for nucleus A and significantly larger for nuclei B and C . Finally, one also needs to take into

account additional frictional energy terms due to pinning mechanisms active during domain wall motion. Taking these changes into account, one could expect to obtain $(\Delta U_{2D})_A$ to be small but positive, which could account for an increased steady-state velocity v_s at a constant field.

5.2.6.2. Nucleation and Wall Pinning

Figure 64 shows a time dependence for the nucleation rate at a constant field value. The general trend is that there is a linear increase in the total number of independently growing domains, N , with time, t , after the onset of a steady-state voltage followed by saturation at some constant value N_{sat} . Another general feature that is observed is that the onset of saturation in the total number of independent nuclei coincides with the onset of merging events between independently growing domains. This suggests that the saturation of the number of independent nuclei is related to the merging events. If we think of the initial nucleation rate N_f as the probability of nucleation per unit time, then the saturation of N implies that this probability tends to zero. The probability of independent nucleation at any time t should be directly proportional to the untransformed area which is the area under the electrode where domain reversal has not yet taken place. Therefore, the probability N_f of nucleation per unit time should be directly proportional to the untransformed area. Since the untransformed area decreases with time and tends to zero after a time $t = t_s$, which is the switching time, the nucleation probability N_f also tends to zero. In other words, the probability of independent nucleations decreases with time because of the growth of the previously nucleated domains which overrun potential nucleation sites. These arguments should be true whether or not merging kinetics speed up the process of domain reversal. However, the merging accelerates this process by resulting in a faster decrease of the untransformed area with time and thereby giving a sharper saturation shoulder to the N - t curves.

The magnitude of N_{sat} itself should decrease with higher electric fields as observed in Figure 64, because of higher wall mobilities resulting in a faster overrunning of potential nucleation sites by fewer and fewer nuclei that nucleate at the start of the application of field. A higher electric field should result in a higher probability of nucleation per unit time. The initial nucleation rate N_f however shows a small initial decrease with field followed by a significant increase. Before this information is interpreted, it must be noted that the data in Figure 64 are based on four different video measurements at four field values. One of the assumptions in the measurement of nucleation statistics is that it is truly random spatially. In practice this could be questioned for a small number of measurement statistics, and therefore the initial drop in N_f in Figure 64 needs to be reconfirmed with a statistically significant number of measurements before being subjected to interpretation.

A simple estimate of the domain-reversal field in a ferroelectric would be $E \sim P_s/(\epsilon\epsilon_0)$ where P_s is the spontaneous polarization ($50 \mu\text{C cm}^{-2}$), ϵ (≈ 45) is the relative dielectric constant and ϵ_0 is the free space permittivity; this gives $E \sim 12,600 \text{ kV cm}^{-1}$, which is of the order of the observed activation fields δ_f . The actual domain-reversal fields (see Fig. 20) are 2 orders of magnitude smaller than this estimate. This suggests that the nucleation of 180° domains in LiTaO_3 is dominated by defects in the crystal which reduce the overall field required for domain reversal.

The initial nucleation of domains in the LiTaO_3 crystal occurs near line shaped defects that appear to criss-cross growing

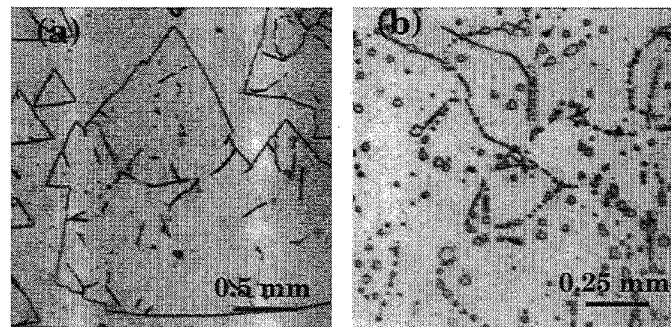


Fig. 72. Line shaped features observed inside growing 180° domains in forward poling where domain reversal occurs last inside the lines. (b) In reverse poling, initial nucleation of domains occurs first along these line shaped features. V. Gopalan, *J. Appl. Phys.* 83, 941 (1998).

domains. Etching of the crystal in 1HF+2HNO₃ at 90°C reveals faint lines in the *z*-plane of the crystals. Figure 72(a) shows such line features inside growing domains in a forward poling geometry. Similar features are also found in the growing domains observed in cross-section (+*y*-face). Careful observation reveals that these features are regions where domain reversal has *not* taken place in the initial stages, while domains nucleate in the regions around these features. In the forward poling geometry, domain reversal takes place *last* in these regions. At lower fields, some remnants of these line features remain after the end of the transient current in the form of microdomains. However, these features can be completely eliminated by applying a high electric field of ~245 kV cm⁻¹ in forward poling for about 5–10 min. This was confirmed by etching experiments. However, in the reverse poling geometry, domain reversal occurs *first* in these regions as shown in Figure 72(b) (not the same area as Fig. 72(a)).

One plausible explanation is that these line shaped features are local regions where the internal field is slightly *higher* than the surroundings. Since the internal field is related to nonstoichiometric point defects in the crystal, these regions would then correspond to local variations in the defect concentration in the crystal. The other possibility is that these defects are related to dislocations or low angle grain boundaries in the crystal. The strain field associated with these defects can then give rise to local electric-field gradients through the piezoelectric phenomenon, resulting in preferential nucleation of new domains around these defects [142]. Etching studies in the literature on LiNbO₃ and LiTaO₃ crystals reported the following types of defects: (a) dislocations propagating at an angle to the *c*-axis with a projection in the *c*-plane along [-1010] and [11-20] directions [153] with an area density of ~10⁻³–10⁻⁵ cm⁻²; (b) screw dislocations parallel to the *c*-axis [0001] with an area density of ~10⁻⁶ cm⁻² [154]; (c) 180° microdomains with an area density of 10⁻²–10⁻⁵ cm⁻² [137, 155]; (d) Possible compositional-point defect variations giving rise to differential etching rates on the *c*-surface [154].

The two different activation fields in Figure 52 in the low-field and high-field regimes are attributed by Gopalan and Mitchell [132] to arise from two distinct types of nucleation sites. The nucleation at low fields appears to arise from pre-existing microdomains in the crystals while at higher fields, other nucleation sites become active as well.

The fact that reversible domain wall motion occurs at electric fields an order of magnitude lower than the coercive fields for permanent domain motion suggests that the threshold field for

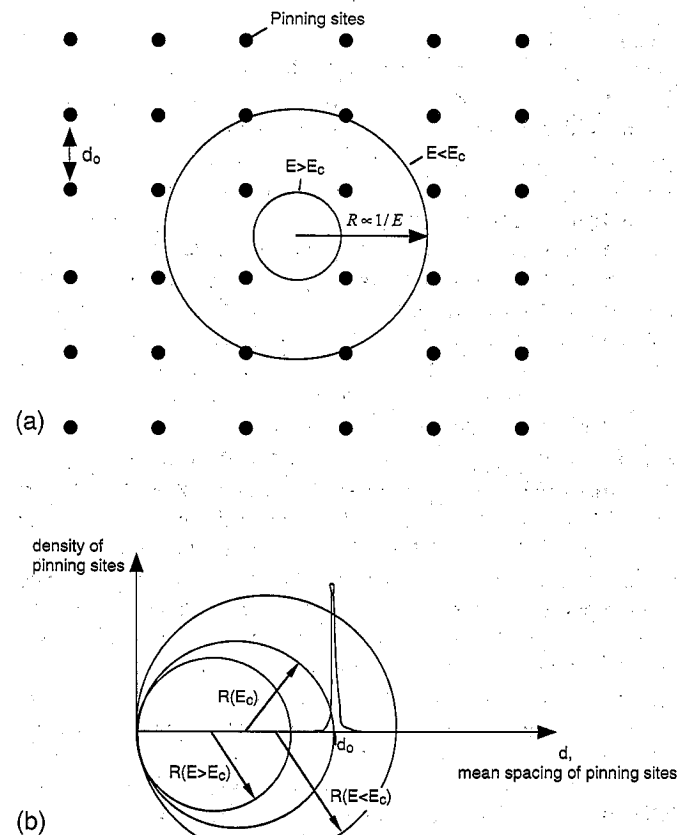


Fig. 73. Schematic showing that the average spacing, d_0 , between pinning sites, should be less than or equal to $2R$ where R is the radius of curvature of a bowing domain wall described by Eq. (38), and E_c is the coercive field.

domain motion may correspond to a pinning-depinning transition. In the simple model presented earlier, the radius of curvature $R = \sigma_w / (2P_s E)$. Since σ_w and P_s are material parameters which are a constant for a given material and composition, R is (inversely) proportional to only the external electric field. Therefore, for pinning sites with infinite pinning strength, a domain wall can only be pinned by pinning sites which are spaced by a distance $d = 2R$, as shown in Figure 73. If the threshold field is indeed a pinning-depinning transition, then it corresponds to an electric field E_c where $R = d/2$. For electric fields $E > E_c$, R will be less than $d/2$, and therefore domain pinning does not occur. This analysis, of course, assumes an infinite pinning strength of the pinning sites. In reality, there may be a distribution of pinning strengths for the pinning defects, thus broadening the range of electric fields over which depinning occurs. A domain wall could also possibly break free (depin) even for electric fields corresponding to $R > d/2$.

The physical nature of these pinning sites is yet unknown, but three possibilities are being investigated. First, the pinning sites may correspond to local variations in the lithium nonstoichiometry in the crystal. The congruent composition in both LiNbO₃ and LiTaO₃ correspond to $(\text{Li}/(\text{Li}+\text{Nb})) \approx \text{Li}/(\text{Li}+\text{Ta}) = 48.5\%$, and therefore, this argument seems questionable. However, it is now considered possible that the actual lithium deficiency in the so-called congruent LiTaO₃ available commercially may be even lower (~47.7%) [157]. This, if confirmed, would indeed support the previous argument. From the established correspondence be-

tween birefringence, strain, and correlation with lithium nonstoichiometry, one could also surmise that the pinning sites correspond to regions of increased lithium nonstoichiometry. The second possibility is that the pinning sites correspond to residual oxygen vacancies, which normally do not exist except when subjected to reducing atmosphere. The congruent LiTaO₃ crystals are grown in slightly reducing atmosphere, while the congruent LiNbO₃ crystals are not, which would support the second argument. Finally, the pinning sites may correspond to physical defects such as screw dislocations whose density may vary depending on the quality of crystal growth [154].

5.2.6.3. Avrami Exponents

The Avrami model leads to Eq. (36) for the transformed area (or the domain-reversed area) as a function of time at a constant electric field. The time exponent n which is predicted to be 3 for the two-dimensional case in Eq. (36), is in reality a function of time and electric field and exceeds values of 10, as shown in Figure 66. These apparent discrepancies relate to the fundamental assumptions made in the derivation of Eq. (36) which need to be reconsidered. The most important correction is that the sideways velocity $v_{s,f}$ at a given electric field is not a constant but rather a function of time. At the start of the domain reversal process, the sideways velocity of 180° domains is dominated by the growth of independent domains as shown by the data (as circles) in Figure 62. After the merger of domains, the sideways velocity is dominated by merged domain fronts as shown by the data (as triangles) in Figure 62. In the intermediate stages where both independent domains and merged domain fronts coexist, there is a distribution of velocities of domain growth.

At lower electric fields, the switching process is mainly dominated by the independently growing domains. In such a case, the time dependence of the sideways wall velocity can be ignored up until the very end of the switching period. Therefore, the assumption of a constant $v_{s,f}$ holds reasonably well in Eq. (36), and the time exponent n is close to 3 as predicted by the equation. This can be seen to be true for samples F207 and F208 in Figure 66 which show an Avrami exponent of 2.95 and 3.11, respectively. At high fields, the merging kinetics become increasingly important, and the assumption of a constant $v_{s,f}$ with time breaks down.

The effect of domain growth due to electrode edges also affects the Avrami exponent, typically lowering it due to a switch to a quasi-one-dimensional nucleation and growth problem along the edges [158]. However, in our EOIM measurements, we observe the kinetics only in a small area of $0.97 \times 0.73 \text{ mm}^2$ at the center of the electrode which is a circle of 4-mm diameter. The edge effects are therefore excluded from the measured data by EOIM. This is also reflected in the fact that the Avrami exponent obtained from the EOIM data for sample F208 is 3.11 while the same exponent obtained from the accompanying transient current data for the entire electrode area (see Fig. 65) is ~1.1 for the most part of the switching process (~70% t_s) and increases to ~2.9 toward the end of switching where merging dominates.

5.2.6.4. Residual Traces Behind a Moving Wall

Another interesting observation is evident in the electro-optic video images of domain walls. Inside a growing domain, one observes shadows or traces of the previous positions of the domain

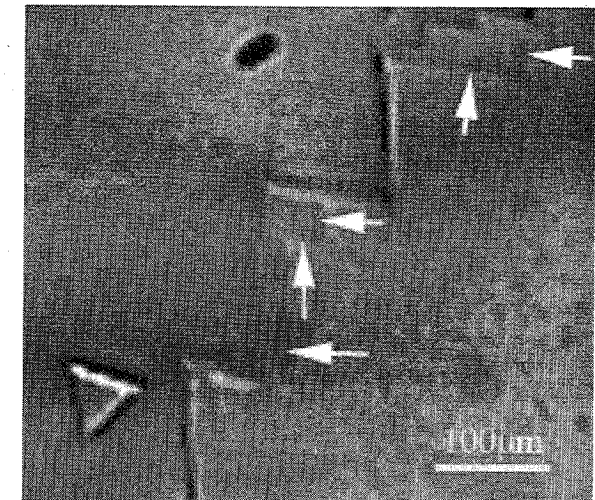


Fig. 74. Residual traces behind a moving domain wall in congruent LiTaO₃. V. Gopalan, *J. Appl. Phys.* 83, 941 (1998).

wall. This is most clearly seen in the merged domain fronts. Figure 74 shows an expanded version of a section of a video frame to illustrate this point. The traces are indicated by arrow heads. These traces disappear with time in ~0.1–1 s, and, since every frame in video is 1/30 s apart, these traces are therefore captured in real-time imaging. The time constant for disappearance immediately suggests a possible connection to the stabilization time of a domain wall in LiTaO₃ which is ~1 s. It is currently believed that this residual contrast is associated with a strain field associated with the domain wall. It was discussed earlier in Section 4.3 that a 180° domain wall in congruent LiTaO₃ is associated with a birefringence and a strain field, which also show a strong correlation to internal fields, which in turn arise from lithium nonstoichiometry in the crystals. Though it is not clear exactly how the point defects give rise to macroscopic strains and birefringence, one can say that when a domain wall moves in the crystal, the strain field associated with the wall should tend to disappear at the original location of the domain wall and reform at the new location. This process of disappearance of strain fields is seen as the disappearance of traces behind a leading domain wall front. The fading residual traces behind a moving domain wall cannot have origin in the electro-optic effect due to external field, since a domain wall does not exist at the site of a trace any longer. This contrast is most likely related to residual internal strains which are relaxing with time.

5.3. Congruent Lithium Niobate

There are a number of similarities and differences in the kinetics of 180° domains in LiNbO₃ and LiTaO₃. Among the similarities are the coercive fields for creating 180° domains, a large built-in internal field in virgin crystals and its correlation to the presence of nonstoichiometric point defects, exponential behavior of switching times with external field, a well-defined stabilization time for domain walls, and birefringence and weak scattering at domain walls created at room temperature [40, 41, 87]. The primary differences are in the magnitude of internal fields, the shape of the transient current pulse during domain creation, 2 orders of magnitude difference in stabilization times, and the shape of the nucleated domains as discussed later.

5.3.1. Domain Switching Times

To measure the switching time in an area of 18 mm^2 , step voltages of varying magnitudes were applied to the crystals, and the width of the transient current pulse was measured. Typical transient current pulses for LiNbO_3 and LiTaO_3 for an applied step voltage were shown in Figure 18(a) and (b), respectively. While the switching time is about the same in Figure 18(a) and (b), the shape of the current is very different. The current pulse is continuous in LiTaO_3 while it is in the form of sharp spikes typically a few milliseconds wide in LiNbO_3 . The value of the peak current can reach values of $>10 \text{ mA}$ for LiNbO_3 while it is $\sim 1 \text{ mA}$ for LiTaO_3 for similar switching times of $\sim 25 \text{ ms}$. The differences in the shape reflect very different domain kinetics in these structurally similar materials.

The switching times as a function of applied electric field are shown in Figure 75 for congruent LiNbO_3 . The field axis is plotted as $1/(E \pm E_{\text{int}})$, which should be interpreted as $1/(E - E_{\text{int}})$ for forward poling and $1/(E + E_{\text{int}})$ for reverse poling as before. Internal field values of $E_{\text{int, LN}} = 22.2 \text{ kV cm}^{-1}$ were used to plot the data such that the forward and reverse switching times overlap. The linear parts of Figure 75 can be expressed similar to that in Eqs. (28) and (29). The values of the fitting parameters in Eqs. (28) and (29) are: $\ln(t_{fo}(\text{s}))_{\text{LN}} = \ln(t_{ro}(\text{s}))_{\text{LN}} = -81 \pm 10$ and $\delta_{f, \text{LN}} = \delta_{r, \text{LN}} = 14,700 \pm 1350 \text{ kV cm}^{-1}$ for congruent LiNbO_3 .

At low fields, as the field $E \pm E_{\text{int}}$ approaches an intrinsic coercive field, E_o , one can observe deviations from Eqs. (28) and (29). From Figure 75, we can estimate $E_{o, \text{LN}} \sim 165 \text{ kV cm}^{-1}$, and $E_{o, \text{LT}} \sim 157 \text{ kV cm}^{-1}$. By definition, one can require that $E \pm E_{\text{int}} = E_o$, the switching time should tend to infinity. Hence, the behavior of switching time as it approaches this value can be written as, $t_f \propto 1/((E - E_{\text{int}}) - E_o)$ and $t_r \propto 1/((E + E_{\text{int}}) - E_o)$. However, there is a lack of sufficient data in this regime in Figure 75 to confirm this behavior. Therefore, in this regime, only a free-hand broken-line fit is shown as a guide to the eye.

5.3.2. Domain Stabilization Times

Similar to congruent LiTaO_3 , it is also observed in congruent LiNbO_3 that when 180° domains are created at room temperature,

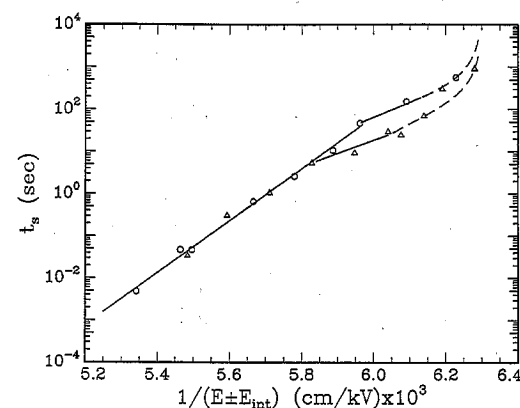


Fig. 75. The switching times of 180° domains in 18 mm^2 area of z-cut LiNbO_3 and LiTaO_3 crystals as a function of external field at room temperature. The field axis should be interpreted as $1/(E - E_{\text{int}})$ for forward poling and $1/(E + E_{\text{int}})$ for reverse poling. The internal field $E_{\text{int, LN}} = 22.2 \text{ kV cm}^{-1}$ was determined for LiNbO_3 , such that the forward and reverse switching times overlap. V. Gopalan, *Solid State Commun.* 109, 111 (1999).

the applied field must remain on for some time after the domains are created for these domains to be stable. If the field is removed before this time, called the stabilization time, the newly created domains disappear by reversible domain wall motion.

The stabilization times were measured by applying square voltage pulses of varying magnitudes and pulse widths and a zero baseline voltage to the crystals, and then observing under polarized light microscope to observe the 180° domains created [159]. Table VII summarizes the results of these experiments. Any voltage pulse less than 10-ms wide in LiNbO_3 results in a reversible domain wall motion during forward poling (State I to State II in Fig. 20). Above pulse widths of 30 ms in LiNbO_3 , the stabilization is complete. For pulse widths between 10–30 ms in LiNbO_3 , there is partial stabilization. Figure 76 shows the transient current pulses in each of these regimes. The negative current after the voltage pulse is indicative of the extent of reversible domain wall motion. These results were confirmed for fields up to 220 kV cm^{-1} in LiNbO_3 . At these fields, one would expect a switching time of $\sim 1 \text{ ms}$ from Eq. (9). In reverse poling, the stabilization time is 5 ms for LiNbO_3 , which is much lower than for forward poling. However, annealing the crystals in State II at 250°C for 1.5 h followed by cooling to room temperature results in a stabilization time of 10–20 ms in LiNbO_3 .

The stabilization mechanism of 180° domains appears to have a correlation to the internal field in the crystal similar to congruent LiTaO_3 . The internal field in turn was shown to clearly depend on lithium nonstoichiometry [77]. Therefore, the stabilization time appears to be directly related to the nonstoichiometric point defects. Video-data on domain kinetics in both LiNbO_3 and congruent LiTaO_3 show that after a domain wall has moved from its initial position to a new position, it leaves behind a trace at its original location which then disappears with time as discussed in the next section. The trace indicates the presence of an optical scattering region, which is in turn related to local strains through photoelastic constants. As suggested before, a plausible picture of domain stabilization is that in a crystal with nonstoichiometric point defect complexes with preferred orientation with respect to the polarization direction, the presence of a polarization gradient in the material (such as a domain wall) results in a relaxation of the defects in the wall region so as to stabilize this wall. The nature of this relaxation can have both elastic (strain) and electrostatic (electric fields) components since they are related in a piezoelectric material. There can be many time constants for this relaxation process as discussed in Section 5.2.2. At least one of these is suggested to

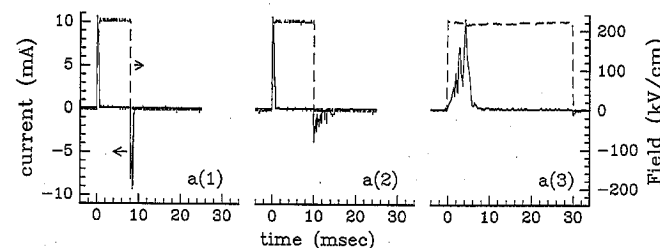


Fig. 76. The 180° domain stabilization phenomenon for LiNbO_3 (LN) crystals in forward poling. After a pulsed field is applied (broken line) with a width of $<10 \text{ ms}$ for LN, (see a(1)), reversible domain wall motion occurs as seen by the negative current. A pulse width of $>30 \text{ ms}$ for LN (see a(3)) results in complete stabilization of newly created 180° domains. In intermediate ranges of pulse widths, (see a(2)) partial stabilization occurs. V. Gopalan, *Solid State Commun.* 109, 111 (1999).

Table VII. Stabilization Times of 180° Domains in Congruent LiNbO_3 and Congruent LiTaO_3 Crystals at Room Temperature*

Crystal	Stabilization time, t_{stab} , required for 180° domains at room temperature		
	During forward poling (s)	During reverse poling (s)	During reverse poling after a 250°C anneal for 1.5 h (in s)
Congruent LiNbO_3	$10 \times 10^{-3} - 30 \times 10^{-3}$	$5 \times 10^{-3} - 8 \times 10^{-3}$	$10 \times 10^{-3} - 20 \times 10^{-3}$
Congruent LiTaO_3	1.4–2	0.1–0.3	0.9–1.6
Stoichiometric LiTaO_3	0.25–0.3	$20 \times 10^{-3} - 30 \times 10^{-3}$	—

*Source: V. Gopalan, *Solid State Commun.* 109, 111 (1999).

be of the order of the observed stabilization times. Wang et al. [88] measured the time dependence of the coercive field after domain reversal in forward and reverse directions. They performed experiments as follows: After forward reversal of domains at room temperature, they waited for a time Δt before switching back (reverse poling) the domain, and measuring the electric field required for the switch as a function of Δt . A similar experiment was done for reverse domain reversal as well. They found the following relationships for time dependence of forward and reverse domain reversal,

$$E_f(\Delta t) = E_f(\infty) - [E_f(\infty) - E_f(0)]e^{-\Delta t/\tau_f} \quad (40)$$

and

$$E_r(\Delta t) = E_r(\infty) - [E_r(\infty) - E_r(0)]e^{-\Delta t/\tau_r} \quad (41)$$

where the best fits for data were found to be $E_f(\infty) = 23 \text{ kV mm}^{-1}$, $E_f(0) = 21 \text{ kV mm}^{-1}$, $E_r(\infty) = 16 \text{ kV mm}^{-1}$, $E_r(0) = 14.8 \text{ kV mm}^{-1}$, $\tau_f \sim 60 \text{ s}$, and $\tau_r \sim 100 \text{ s}$. While the experimental data points were not sufficient to exclude further time constants for relaxation at small time scales, it does indicate at least one relaxation process on time scales of 60–100 s. The internal field E_{int} discussed before and corresponding to the offset in the hysteresis loops in Figure 20, would be equivalent to $(E_f - E_r)/2$ for large time scales ($\Delta t \gg \tau_f$ or τ_r). The relations (40) and (41) therefore give the time dependence of this internal field for the shorter time scales. The stabilization time would correspond to a much faster time constant relaxation which was not measured by Wang et al., and could be incorporated as additional exponential decay terms. Equation (30) appears to be of a single exponential form. However, similar measurements of change in coercive field with time by Brown et al. [141] in congruent LiTaO_3 , was carried out over a larger range of times (20–3600 s), which fit very well to double exponential similar to the form given by Eq. (30). In particular, the latter authors pointed out that a single exponential of the form of Eqs. (40) and (41) were unsatisfactory. Given the more limited range of time (25–400 s) over which Wang et al. [88] performed their experiments, it would appear that additional exponential decay terms should be included in Eqs. (40) and (41).

The reviewer feels that the application of Eq. (30) describing the possible variation of $E_{\text{int}}(t)$ to the variation of $E_f(\Delta t)$ or $E_r(\Delta t)$ [141] may not be correct since according to Eq. (30), $E_{\text{int, total}}(0) = -E_{\text{int, total}}(\infty)$, which need not to be true for $E_f(\Delta t)$ or $E_r(\Delta t)$. A physical model which incorporates multiple exponential terms as in Eq. (30), different values of τ_f and τ_r , as well as forces $E_f(0)$, $E_r(0)$ to a small negative value, would be as

follows

$$E_f(\Delta t) = E_f(0) + \sum_i E_{f,i} (1 - e^{-\Delta t/\tau_{f,i}}) \quad (42)$$

and

$$E_r(\Delta t) = E_r(0) + \sum_i E_{r,i} (1 - e^{-\Delta t/\tau_{r,i}}) \quad (43)$$

Since time Δt in the above equations is the time difference between forward poling event and a subsequent reverse poling sequence, by definition, $E_f(\Delta t = t_{\text{stab, r}}) = 0$ and $E_r(\Delta t = t_{\text{stab, f}}) = 0$, where $t_{\text{stab, f}}$ and $t_{\text{stab, r}}$ are the forward and reverse stabilization times, respectively. This defines the zero crossing of the E_f and E_r versus Δt plots. This can be imagined as follows: consider an electric field pulse with a width exactly equal to $t_{\text{stab, f}}$ which results in forward poling at the start of the pulse, and reverse poling (domain backswitching) immediately following the end of the pulse. (For example, see Figure 76.) The reverse poling in this case occurs at zero electric field because it occurs after the pulse is over, and therefore $E_{c, r} = 0$. The time difference between forward and reverse poling currents corresponding to this condition is $\Delta t \sim t_{\text{stab, f}}$, and therefore, $E_r(\Delta t = t_{\text{stab, f}}) = 0$. This discussion leads to the conclusion that for $\Delta t < t_{\text{stab, f}}$, for example, the $E_{c, r} < 0$ which literally means that an electric field in forward poling direction (negative $E_{c, r}$) causes domain reversal in reverse poling direction. The negative coercive fields, though counter-intuitive, refer to the minimum baseline voltage after the end of a pulse that is needed to prevent domain backswitching at the end of the pulse.

The variation of the internal field with time would then be given as $(E_f(t) - E_r(t))/2$. Once a domain wall has moved away to a new location, the defects in the original location relax back which is observed as a disappearing trace behind a domain wall. The defects in the new location of the wall have to relax to accommodate the presence of a polarization gradient in that region, which manifests as the stabilization time. It is however not clear why there is a large difference in the stabilization times of domains in congruent LiNbO_3 and LiTaO_3 . This may be related either to the density of point defect complexes, or differences in the physical nature of the defect complexes themselves.

5.3.3. Sideways Wall Velocity

The electro-optic imaging microscopy was used by Gopalan et al. [160] to observe the nucleation and growth kinetics of 180° domains in congruent LiNbO_3 crystals under an external electric field. There are significant differences in the domain kinetics between LiNbO_3 and LiTaO_3 crystals which are revealed by such a

study such as the domain shape, shape of transient currents, and the dependence of domain wall velocity with time at a constant electric field.

The congruent z-cut LiNbO₃ wafer used in this study was 0.25-mm thick. The coercive field for this wafer was measured to be 21.5 kV mm⁻¹. An external electric field of 21.6 kV mm⁻¹ was applied as a step voltage as shown in Figure 77 along with the resultant transient current data. The transient current shows a series of spikes resulting from the domain reversal in the entire electrode area. These spikes are more clearly seen in the expanded view of a small range of these current data as shown by the solid line curve in Figure 77(b). Overlapped on this plot are also two different measurements of the sideways wall velocities (shown as circles and triangles connected by a broken line) of a 180° domain front measured from the video-data as discussed in detail later.

Figure 78 shows a sequence of selected frames from the video-data on a congruent LiNbO₃ wafer. The polarization axis is normal to the image plane. It must be borne in mind that these data were collected only from a 0.97×0.73-mm area at the center of a much larger electrode area (4π mm²). The 18 frames labeled (a)–(r) show the 180° domain microstructure in the wafer at different times *t* after the application of the voltage pulse. The frame times are chosen at unequal intervals to reflect the nature of the “jerky” movement of the principal domain wall front, III, seen first in frame (f). The image contrast in the figure is original, and is not modified in any way. The only additions made are the superimposition of text and arrow labels. Some important observations can be made from this figure.

(1) The nucleating domains are six-sided polygons, all having the same orientation of the domain walls with respect to the crystallographic *x*- and *y*-axes shown in frame (a). The six-sides are best seen in the domain labeled I in frame (a) after it has grown larger (see frames (e)–(m)). A single 120° corner of a hexagon is also seen clearly in the top left-hand corner of the large domain front III in frame (p).

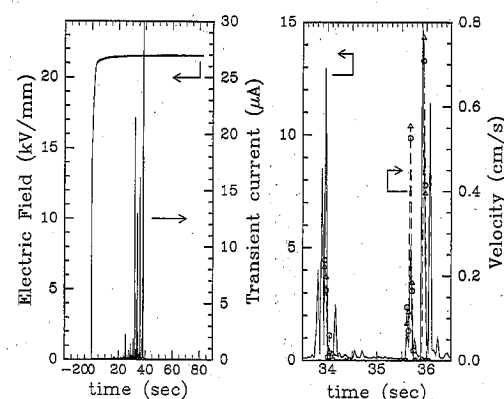


Fig. 77. (a) Applied voltage and the transient current response during domain reversal in congruent z-cut LiNbO₃ crystals. (b) The measured sideways wall velocity, v_s , of the 180° domain front (labeled III) as a function of time as measured from the electro-optic imaging data of Figure 78. Two sets of velocity measurements performed on a 180° domain front at the locations of the arrows in Figure 78(f) are plotted here as circles and triangles, and connected by a broken line. The transient current response from Figure 77(a) is also shown (solid line) for comparison. V. Gopalan, *Appl. Phys. Lett.* 75, 16 (1999).

(2) Independently growing domains (domains spatially well separated from other nuclei) appear to have sideways growth velocities, v_s ranging from no motion ($v_s \sim 0$) at times to an estimated value on the order of $\sim 0.1\text{--}1\text{ }\mu\text{m s}^{-1}$. On the other hand, adjacent nuclei which are close together in a cluster merge rapidly to form a much larger polygonal domain enclosing the cluster. For example, the domain cluster labeled II merges from frame (d) to (e) and cluster I merges from frame (a) through (e). However, after the merger, these independent domains do not appear to show any further significant growth until they are overrun by another larger domain in frames (k) and (n), respectively.

(3) A larger merged domain front labeled III appears in the field of view in frame (f) and sweeps through the frame. The velocity of this front is measured as a function of time at the locations, and in the direction, of the two arrows shown in frame (f). These two sets of measurements are shown in Figure 77(b) as triangles and circles connected by a broken line. The velocity appears to

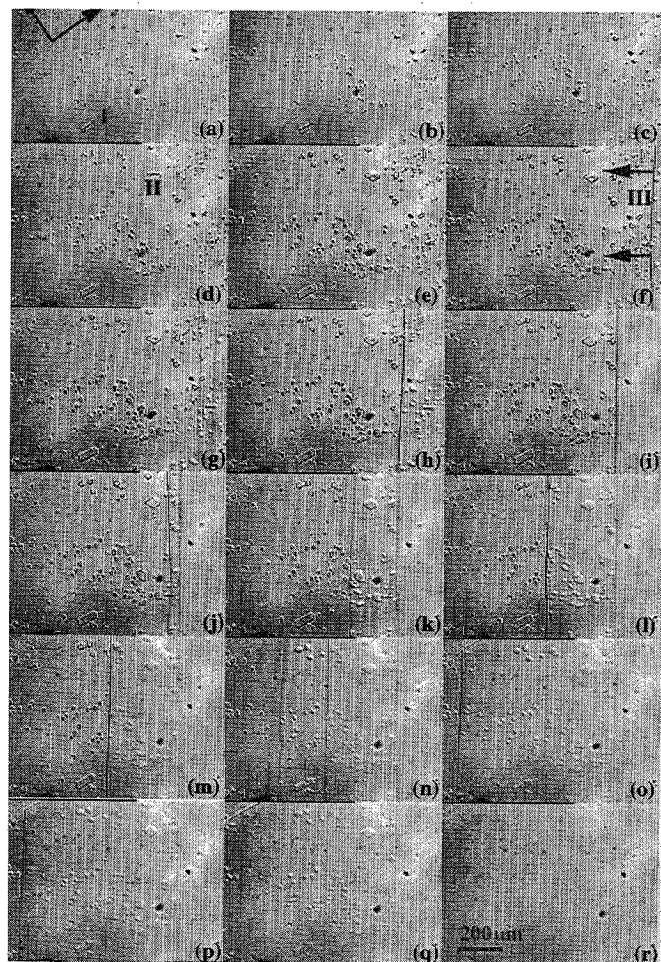


Fig. 78. Selected video-frames from in situ video recording of the 180° domain kinetics in congruent z-cut LiNbO₃ under an external field of 21.6 kV mm⁻¹ (applied at time $t = 0$). The time, t (in seconds) corresponding to each frame is: (a) 18.47, (b) 21.44, (c) 24.44, (d) 27.44, (e) 33.874, (f) 33.907, (g) 33.940, (h) 33.974, (i) 35.574, (j) 35.640, (k) 35.674, (l) 35.707, (m) 35.907, (n) 35.904, (o) 35.974, (p) 36.040, (q) 36.074, (r) 37.907. The polarization axes are normal to the image plane, and the crystallographic *x*- and *y*-axes are marked. V. Gopalan, *Appl. Phys. Lett.* 75, 16 (1999).

show a jerky behavior with time ranging from zero to $\sim 0.8\text{ cm s}^{-1}$ in this measurement, qualitatively similar to the transient current data. Here the value of 0.8 cm s^{-1} should be interpreted as a lower limit for the maximum velocity at this field, since our smallest time resolution is limited to one frame interval (33 ms). It also appears from Figure 77(b) that there is a possible quantitative correlation between the velocity measurement and the transient current data. Ideally, for the same area of measurement for transient current (I) and sideways wall velocity (v_s), a single domain front such as III, sweeping across the area with width W would give rise to a transient current $I \sim 2v_s WP_s$. However, in this measurement, the transient current reflects the domain-reversal process in the entire electrode region (area of $4\pi\text{ mm}^2$) while the velocity measurement is for a single domain front passing through an area of $0.97 \times 0.73\text{ mm}$ at the center of this electrode region. Therefore, this correlation though expected, is somewhat fortuitous in this case, perhaps due to the fact that this domain front is large enough to dominate the kinetics in the time interval shown.

(4) Smaller domains which are overrun by the larger domain still appear to show some contrast after being overrun as clearly seen in frames (j)–(q). This residual contrast exists despite the absence of a domain wall at the original location, and it decays with time typically on the time scale of $\sim 1\text{ s}$. This contrast appears to be related to the presence of strains adjacent to 180° domain walls in LiNbO₃ which in turn are related to the presence of lithium nonstoichiometry based point defect complexes [64, 77]. The residual contrast at the original location of a domain wall disappears as the strain relaxes at that location.

The spikelike transient current data during domain reversal is therefore due to a jerky motion of domain walls as reflected by a similar behavior of wall velocity with time as directly measured from the video-data. This behavior is strongly suggestive of a pinning–depinning type of mechanism for domain wall motion as discussed in Section 5.2.5. The process of the depinning of a domain wall from a pinning site, and its rapid movement until it encounters the next pinning site, would give rise to spikes in the transient current as observed here. The significant differences between the domain kinetics in congruent LiNbO₃ and congruent LiTaO₃ crystals for electric fields near the coercive fields are (a) the nucleating domains are triangular in shape in congruent LiTaO₃ while they are six-sided in congruent LiNbO₃; (b) the independently growing domains show a steady-state velocity with time at a constant field in LiTaO₃ while the velocity consists of a series of spikes with time at a constant field in LiNbO₃.

One of the possibilities for these differences in domain kinetics could arise due to the presence of a much larger density of pinning centers in congruent LiTaO₃ as compared to congruent LiNbO₃. Therefore, the pinning of a moving domain wall occurs as a constant friction in the background in LiTaO₃, resulting in a steady-state average velocity. On the local scale, the wall still pins and depins, implying that there should be discrete current spikes even in LiTaO₃. However, on the length scale of $10\text{ }\mu\text{m}$ or larger (scale of observation here), these events of pinning and depinning are so numerous due to the presence of abundant pinning sites that the current spikes merge together and appear as one continuous transient current curve. In LiNbO₃ on the other hand, the presence of pinning sites and hence the pinning events themselves are statistical in nature. Therefore, the spikes in transient current correspond to discrete depinning events and a fast movement of the domain wall segment before it encounters the next pinning site. The gaps

between current spikes (zero current) correspond to a pinned state of domain walls with zero mobility.

5.4. Stoichiometric Lithium Niobate and Tantalate

At the time of writing this review, very little information exists regarding the domain kinetics in stoichiometric LiTaO₃ and LiNbO₃. Studies by Kim and Gopalan [161] on stoichiometric LiTaO₃ are detailed here. The transient currents during domain reversal show a series of spikes as shown in Figure 19, indicating a pinning–depinning type of domain motion. Figure 79 shows the switching time for an area of $\sim 1\text{-mm}$ diameter in the forward and reverse poling directions. The switching time was directly measured by observing the area using electro-optic imaging, and comparing with the transient current measurements. The small difference in domain reversal fields between forward and reverse directions indicates the presence of a small internal field of $E_{\text{int}} \sim 0.18\text{ kV mm}^{-1}$ suggesting that the crystal stoichiometry may still be slightly lithium deficient. Two distinct activation fields appear to be present for each of the forward and reverse domain reversal processes, that follow the exponential switching time relationships of Eqs. (28) and (29). Table V also lists the activation fields, δ_f and δ_r , and the pre-exponents t_{f0} and t_{r0} for the forward and reverse directions, respectively. These activation fields are 2 orders of magnitude smaller than the values for congruent crystals listed in the same table. The values of activation field for the exponential dependence of wall velocity versus electric field will also be expected to be of similar order of magnitude as in congruent crystals of LiTaO₃. The domain wall energy, according to the Miller and Weinreich analysis [142] (see Eqs. (33) and (34)), should yield wall energies of the order of 0.1 mJ m^{-2} , which is closer to the values estimated for other ferroelectrics such as BaTiO₃. The stabilization times for domains were also measured and found to be $\sim 250\text{--}300\text{ ms}$ for forward domain reversal and $\sim 20\text{--}30\text{ ms}$ for reverse domain reversal. These values are again an order of magnitude smaller than the corresponding stabilization times measured in congruent LiTaO₃. From the correlation between the stabilization times and the lithium deficiency in these crystals, one can suggest that the stabilization time for a domain wall depends on the density of lithium nonstoichiometry defects in the crystal. If the stabilization time reflected an electrostatic or elastic relaxation of each defect complex, and if all defects are identical and independent, then this dependence of stabilization time on density of de-

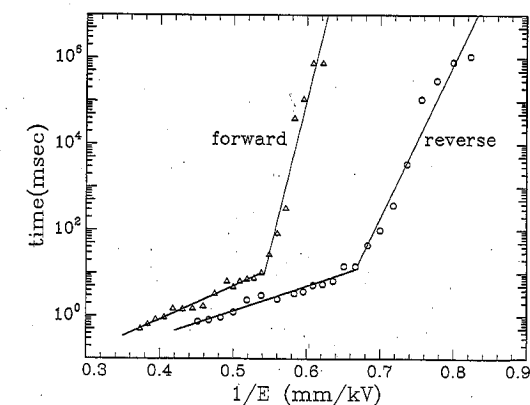


Fig. 79. Switching time as a function of electric field for forward and reverse domain reversals in stoichiometric LiTaO₃.

fects cannot be explained. The experimental confirmation of the latter therefore suggests that defect-defect interactions (which are density dependent) become important in determining the stabilization times of a domain wall. Similar experimental results are expected in stoichiometric LiNbO_3 , which are however not confirmed yet.

6. CONCLUDING REMARKS

6.1. Summary of Reviewed Work

One of the most interesting discoveries in LiNbO_3 and LiTaO_3 crystals was the realization of an immense length scale bridging all the way from point defects arising from lithium nonstoichiometry to macroscopic properties such as ferroelectric hysteresis and internal fields (Section 4). The direct consequence of this realization is that crystals in which domain reversal was considered nearly impossible now exhibit coercive fields as low as $\sim 2 \text{ kV mm}^{-1}$ in near-stoichiometric LiTaO_3 and $\sim 4 \text{ kV mm}^{-1}$ in near-stoichiometric LiNbO_3 at room temperature (Section 4.2). The very large internal fields exhibited by nonstoichiometric compositions appear to be directly related to the lithium deficiency. Even near-stoichiometric LiTaO_3 ($\text{Li}/(\text{Li}+\text{Ta}) \sim 0.499$) exhibit internal fields of $\sim 0.18 \text{ kV mm}^{-1}$, and congruent LiTaO_3 ($\text{Li}/(\text{Li}+\text{Ta}) \sim 0.485$) exhibits internal fields of 5 kV mm^{-1} . The influence of lithium deficiency on domain shape, domain wall birefringence and strains, and motion of domain walls under external fields is equally stark (Section 4.3). With increasing lithium deficiency in LiTaO_3 , the preferred domain wall orientation switches from the six y - z -planes forming hexagons in stoichiometric compositions, to three of the six x - z -planes forming a triangle (at low driving fields) and all six x - z -planes forming a hexagon (at high driving fields) in congruent compositions. In contrast, both stoichiometric and congruent compositions of LiNbO_3 show hexagonal domains with walls parallel to the y - z -planes, though defect mediated triangular domains were observed in doped LiNbO_3 crystals. Lithium nonstoichiometry in congruent crystals also induces strong optical birefringence ($\sim 10^{-5}$ in LiTaO_3), strains ($\sim 10^{-4}$ in LiTaO_3) and local electric fields ($\sim 10 \text{ kV mm}^{-1}$ in-plane in LiTaO_3), over regions which extend over many micrometers adjacent to domain walls. These features tend to disappear in stoichiometric crystals.

These discoveries have become possible with the possibility of growth of high quality noncongruent crystals using the double crucible Czochralski (DCCZ) technique for the growth of stoichiometric LiNbO_3 and LiTaO_3 (Section 2). With the already large scale commercialization of wafers and boules of these materials, there has also been an increasing demand for in situ and non-destructive techniques to characterize crystal and device quality. Two significant advances were made in this regard. The detailed experiment and theory of using Maker fringe analysis as a characterization tool for wafer thickness, composition, strain, and internal field variations over an entire 2–3-in wafer of LiNbO_3 or LiTaO_3 was realized (Section 3). Second, the use of the electro-optic effect to image domains and domain motion in real-time in LiNbO_3 and LiTaO_3 using optical microscopy resulted in a real-time study of the nucleation and growth dynamics of ferroelectric domains in these materials. This has enabled a direct measurement of domain wall mobilities, nucleation growth, and merger dynamics, which could only be performed ex situ before. From a technological viewpoint, the microengineering of ferroelectric domains

for integrated optical applications also benefited from a real-time and nondestructive monitoring of the domain engineering process during device fabrication.

6.2. Fundamental Scientific Issues

The advances described earlier provide a mere glimpse of the importance of point defects, dopants, and their influence on the physical properties of LiNbO_3 and LiTaO_3 crystals. Much remains to be explored in understanding these fascinating material systems. Some of the key issues, in our opinion, are listed as follows:

- (1) What is the exact nature of point defect complexes arising from lithium nonstoichiometry? What are the elastic distortions and dipolar charge distributions associated with a point defect complex? How are these elastic and electrical fields of a defect coupled to the lattice. How do defect clusters interact with each other? How do the defect complexes evolve with temperature?
- (2) How thick are the domain walls? How do point defect complexes interact with the polarization gradient at a wall? How does this interaction influence the optical and strain contrast at the walls? How does this interaction determine the preferred domain wall orientations in equilibrium and under slow and fast driving fields? What is the influence of surfaces on domain wall structure and mobility?
- (3) What determines the coercive fields for domain reversal? What are the extrinsic (defect mediated) and intrinsic (structural) components to the observed coercive fields.
- (4) What are the defects that give rise to domain nucleation and domain wall pinning? What is the influence of commonly used doping elements such as hydrogen, titanium, MgO, iron, and erbium on the defect chemistry, domain structure, and dynamics in LiNbO_3 and LiTaO_3 ?

ACKNOWLEDGMENTS

We benefited greatly from many helpful discussions with U. Mohideen, M. C. Gupta, A. Itagi, P. Swart, A. Roshko, B. Steiner, K. K. Wong, and D. J. Jundt. We also thank Crystal Technology for providing, used in the Maker fringe Studies.

REFERENCES

1. B. T. Matthias and J. P. Remeika, *Phys. Rev.* 76, 1886 (1949).
2. R. L. Byer, *J. Nonlinear Opt. Phys. Materials* 6, 549 (1997).
3. R. G. Hunsperger, "Integrated Optics: Theory and Technology", 4th ed., Springer-Verlag, New York, 1995.
4. C. S. Tsai, "Guided-Wave Acousto-Optics: Interactions, Devices, and Applications." Springer Series in Electronics and Photonics, Vol. 23. Springer-Verlag, New York, 1990.
5. D. Psaltis and G. W. Burr, *Computer* 31, 52 (1998).
6. "Harnessing Light: Optical Science and Engineering for the 21st Century," National Academy Press, Washington, D.C., 1998.
7. H. D. Megaw, *Acta Crystallogr.* 7, 187 (1954).
8. A. M. Prokhorov and Y. S. Kuzminov, "Physics and Chemistry of Crystalline Lithium Niobate," Hilger, Bristol, 1990.
9. A. Rauber, in "Chemistry and Physics of Lithium Niobate," Current Topic in Materials Science (E. Kaldis, Ed.), North-Holland, New York, 1978.

10. J. R. Carruthers, G. E. Peterson, M. Grasso, and P. M. Bridenbaugh, *J. Appl. Phys.* 42, 1846 (1971).
11. S. Miyazawa and H. Iwasaki, *J. Cryst. Growth* 10, 276 (1971).
12. T. Fukuda, S. Masumura, H. Hirano, and T. Ito, *J. Cryst. Growth* 46, 179 (1979).
13. K. Kitamura, J. K. Yamamoto, N. Iyi, S. Kimura, and T. Hayashi, *J. Cryst. Growth* 116, 327 (1992); also see *Ferroelectrics* 21, 202 (1997).
14. Y. Furukawa, K. Kitamura, E. Suzuki, and K. Niwa, *J. Cryst. Growth* 197, 889 (1999).
15. P. Lerner, C. Legras, and J. P. Dumas, *J. Cryst. Growth* 3–4, 231 (1968).
16. L. O. Svaasand, M. Eriksrud, A. P. Grande, and F. Mo, *J. Cryst. Growth* 18, 179 (1973).
17. K. Kitamura, in "Crystal Growth of Novel Electronic Materials, Ceramics Transactions" (R. K. Pandey and R. Guo, Eds.), Vol. 60, p. 37, Westerville, OH, Am. Ceramic Soc., 1995.
18. C. D. Brandle and D. C. Miller, *J. Cryst. Growth* 24–25, 432 (1974).
19. J. Koppitz, O. F. Shirmer, and A. I. Kuznetsov, *Europhys. Lett.* 4, 1055 (1987).
20. S. C. Abrahams and P. Marsh, *Acta Crystallogr. B* 42, 61 (1986).
21. S. Matsumura, *J. Cryst. Growth* 51, 41 (1981).
22. K. Shigematsu, Y. Anzai, S. Morita, M. Yamada, and H. Yokoyama, *Jpn. J. Appl. Phys.* 26, 1988 (1987).
23. P. F. Bordui, R. G. Norwood, C. D. Bird, and J. T. Carella, *J. Appl. Phys.* 78, 4647 (1995).
24. R. L. Barnes and J. R. Carruthers, *J. Appl. Crystallogr.* 3, 395 (1970).
25. H. M. O'Bryan, P. K. Gallagher, and C. D. Brandle, *J. Am. Ceram. Soc.* 68, 493 (1985).
26. B. M. Park, K. Kitamura, K. Terabe, Y. Furukawa, Y. Ji, and E. Suzuki, *J. Cryst. Growth* 180, 101 (1997).
27. R. Stubbe, G. Edwall, S. Sahlgren, and L. Svahn, *J. Lightwave Technol.* 10, 1489 (1992).
28. L. E. Myers and W. R. Bosenberg, *IEEE J. Quantum Electron.* 33, 1663 (1997).
29. R. S. Moyer, R. Grenavich, F. F. Judd, R. C. Kershner, W. J. Minford, and R. W. Smith, *IEEE Trans. Comp., Packag., Manufact. Technol. B* 21, 130–135 (May 1998).
30. H. Nagata, *Opt. Eng.* 37, 1612 (1998).
31. H. Nagata, S. Oikawa, and M. Yamada, *Opt. Eng.* 36, 283 (1997).
32. E. J. Murphy, T. O. Murphy, A. F. Ambrose, R. W. Irvin, B. H. Lee, P. Peng, G. W. Richards, and A. Yorinks, *J. Lightwave Technol.* 14, 352 (1996).
33. N. Dagli, *IEEE Trans. Microwave Theory Tech.* 47, 1151 (1999), and references therein.
34. K. K. Wong, A. C. G. Nutt, D. F. Clark, J. Winfield, P. J. R. Laybourn, and R. M. De LaRue, *Proc. IEEE* 133-J, 113 (1986).
35. R. J. Holmes and W. J. Minford, *Ferroelectrics* 75, 63 (1987).
36. L. McCaughan and K. D. Choquette, *IEEE J. Quantum Electron.* 22, 947 (1986).
37. A. Yariv and P. Yeh, "Optical Waves in Crystals," Wiley, New York, 1984.
38. P. F. Bordui, R. G. Norwood, C. D. Bird, and G. D. Calvert, *J. Cryst. Growth* 113, 61 (1991).
39. J. G. Bergman, A. Ashkin, A. A. Ballman, J. M. Dziedzic, H. J. Levinstein, and R. G. Smith, *Appl. Phys.* 12, 92 (1968).
40. P. D. Maker, R. W. Terhune, M. Nisenhoff, and C. M. Savage, *Phys. Rev. Lett.* 8, 21 (1962).
41. N. A. Sanford and J. A. Aust, in "Lasers and Optics for Manufacturing," 1997 OSA Trends in Optics and Photonics Series, Vol. 9, pp. 23–32. (A. C. Tam, Ed.), Optical Soc. of America, Washington, D.C., 1997.
42. S. R. Lunt, G. E. Peterson, R. J. Holmes, and Y. S. Kim, *Proc. SPIE* 578, 22 (1985).
43. S. R. Lunt and G. E. Peterson, *Ferroelectrics* 75, 87 (1987).
44. N. A. Sanford and J. A. Aust, *J. Opt. Soc. Am. B* 15, 2885 (1998).
45. J. A. Aust, Ph. D. Thesis, Department of Electrical and Computer Engineering, University of Colorado, Boulder, 1999.
46. I. Shoji, T. Kondo, A. Kitamoto, M. Shirane, and R. Ito, *J. Opt. Soc. Am. B* 14, 2268 (1997).
47. Y. R. Shen, "The Principles of Nonlinear Optics," Wiley, New York, 1984.
48. D. A. Kleinman, *Phys. Rev.* 126, 1977 (1962).
49. G. J. Edwards and M. Lawrence, *Opt. Quantum Electron.* 16, 373 (1984).
50. D. F. Nelson and R. M. Mikulyak, *J. Appl. Phys.* 45, 3688 (1974).
51. J. R. Carruthers, I. P. Kaminov, and L. W. Stulz, *Appl. Opt.* 13, 2333 (1974).
52. R. L. Byer, J. F. Young, and R. S. Feigelson, *J. Appl. Phys.* 41, 2320 (1970).
53. L. I. Ivleva, Y. S. Kuz'minov, and L. S. Shumskaya, *Fiz. Tverd. Tela* 14, 3137 (1972).
54. Z. I. Ivanova, A. I. Kovrighin, G. V. Luchinsky, L. N. Rashkovich, N. M. Rubina, and A. I. Kholodnykh, *Kvant. Elek.* 7, 1013 (1980).
55. V. G. Dmitriev, G. G. Gurzadyan, and D. H. Nikogosyan, "Handbook of Nonlinear Optical Crystals," Springer-Verlag, Berlin, 1991.
56. K. Hagimoto and A. Mito, *Appl. Opt.* 34, 8276 (1995).
57. B. Steiner, National Institute for Standards and Technology, Gaithersburg, MD, personal communication, 1998.
58. P. Bordui, Crystal Technology Inc., Palo Alto, CA, personal communication, 1997.
59. The value for d_{22} for LiNbO_3 was inferred by using the results of Ref. [20] for KDP taken together with the results of R. C. Miller and W. A. Norland, *J. Appl. Phys.* 42, 4145 (1971), who measured d_{22} with respect to KDP.
60. R. S. Weiss and T. K. Gaylord, *Appl. Phys. A: Solids Surf.* 37, 191 (1984). See also, J. F. Nye, "Physical Properties of Crystals," Oxford Univ. Press, New York, 1995.
61. L. P. Avakyants, D. F. Kiselev, and N. N. Shchitov, *Sov. Phys. Solid State* 18, 899 (1976).
62. M. E. Lines and A. M. Glass, "Principles and Applications of Ferroelectrics and Related Materials," Clarendon, Oxford, 1977.
63. Y. Ohmori, Y. Yasojoma, and Y. Inuishi, *Appl. Phys. Lett.* 25, 716 (1974).
64. V. Gopalan and M. Gupta, *Ferroelectrics* 198, 49 (1997).
65. S. C. Abrahams and J. L. Bernstein, *J. Phys. Chem. Solids* 28, 1685 (1967).
66. S. C. Abrahams, W. C. Hamilton, and A. Sequeira, *J. Phys. Chem. Solids* 28, 1693 (1967).
67. S. C. Abrahams, E. Buehler, W. C. Hamilton, and S. J. Laplace, *J. Phys. Chem. Solids* 34, 521 (1973).
68. S. C. Abrahams, C. W. Hamilton, and J. M. Reddy, *J. Phys. Chem. Solids* 27, 1013 (1966).
69. S. C. Abrahams, H. J. Levinstein, and J. M. Reddy, *J. Phys. Chem. Solids* 27, 1019 (1966).
70. S. C. Abrahams, J. M. Reddy, and J. L. Bernstein, *J. Phys. Chem. Solids* 27, 997 (1966).
71. P. K. Gallagher and H. M. O'Bryan, Jr., *J. Am. Ceram. Soc.* 68, 147 (1985).
72. V. Gopalan, M. J. Kawas, T. E. Schlesinger, M. C. Gupta, and D. D. Stancil, *IEEE Photon. Technol. Lett.* 8, 1704 (1996).
73. M. Yamada, M. Saitoh, and H. Ooki, *Appl. Phys. Lett.* 69, 3659 (1996).
74. R. L. Byer, *J. Nonlinear Opt. Phys. Mater.* 6, 549 (1997).
75. A. A. Ballman and H. Brown, *Ferroelectrics* 4, 189 (1972).
76. N. Niizeki, T. Yamada, and H. Toyoda, *Jpn. J. Appl. Phys.* 6, 318 (1967).
77. V. Gopalan, T. E. Mitchell, K. Kitamura, and N. Furukawa, *Appl. Phys. Lett.* 72, 1981 (1998).
78. K. Kitamura, Y. Furukawa, K. Niwa, V. Gopalan, and T. E. Mitchell, *Appl. Phys. Lett.* 73, 3073 (1998).
79. V. Gopalan and M. C. Gupta, *Appl. Phys. Lett.* 68, 888 (1996).
80. V. Gopalan and M. C. Gupta, *J. Appl. Phys.* 80, 6099 (1996).
81. T. J. Yang and U. Mohideen, *Phys. Lett. A* 250, 205 (1998).

82. T. J. Yang, U. Mohideen, V. Gopalan, and P. J. Swart, *Ferroelectrics* 222, 609 (1999); T. J. Yang, U. Mohideen, V. Gopalan, and P. Swart, *Phys. Rev. Lett.* 82, 4106 (1999).
83. J. A. Aust, B. Steiner, N. A. Sanford, G. Fogarty, B. Yang, A. Roshko, J. Amin, and C. Evans, "Conference on Lasers and Electro-Optics," 1997 OSA Technical Digest Series, Vol. 11, p. 485. Optical Soc. of America, Washington, D.C., 1997.
84. L. L. Pendergrass, *J. Appl. Phys.* 62, 231 (1987).
85. K. Nakamura, H. Ando, and H. Shimizu, *Appl. Phys. Lett.* 50, 1413 (1987).
86. J. A. Aust, N. A. Sanford, and J. Amin, "Proceedings of the Tenth Annual Meeting of the IEEE Lasers and Electro-Optics Society," IEEE Lasers and Electro-Optics Society, Piscataway, NJ, 1997, p. 114(B).
87. A. Mendez, A. Garcia-Cabanes, E. Dieguez, and J. M. Cabrera, *Electron. Lett.* 35, 498 (1999).
88. H. F. Wang, Y. Y. Zhu, S. N. Zhu, and N. B. Ming, *Appl. Phys. A* 65, 437 (1997).
89. S. N. Kaul and K. Singh, *Solid State Commun.* 26, 365 (1978).
90. N. Niizeki, T. Yamada, and H. Toyoda, *Jpn. J. Appl. Phys.* 6, 318 (1967).
91. V. V. Zhdanova, V. P. Klyuev, V. V. Lemanov, I. A. Smirnov, and V. V. Tikhonov, *Sov. Phys. Solid State* 10, 1360 (1968).
92. P. K. Gallagher, H. M. O'Bryan, E. M. Gyorgy, and J. T. Krause, *Ferroelectrics* 75, 71 (1987).
93. W. D. Johnston, Jr. and I. P. Kaminov, *Phys. Rev.* 168, 1045 (1968).
94. E. Schempp, G. E. Peterson, and J. R. Carruthers, *J. Chem. Phys.* 53, 306 (1970).
95. S. Breer, K. Buse, K. Peithmann, H. Vogt, and E. Kratzig, *Rev. Sci. Instrum.* 69, 159 (1998).
96. W. Bollmann, *Phys. Status Solidi A* 104, 643 (1987).
97. G. Bergmann, *Solid State Commun.* 6, 77 (1968).
98. P. Baldi, M. P. de Mitchell, K. El Hadi, S. Nouh, A. C. Cino, P. Aschierl, and D. B. Ostrowsky, *Opt. Eng.* 37, 1193 (1998).
99. L. Kovacs, V. Szalay, and R. Capelletti, *Solid State Commun.* 52, 1029 (1984).
100. A. Grone and S. Kapphan, *J. Phys. Chem. Solids* 52, 797 (1991).
101. Y. Kong, J. Xu, W. Zhang, and G. Zhang, *Phys. Lett. A* 250, 211 (1998).
102. D. M. Smyth, *Ferroelectrics* 50, 93 (1983).
103. O. F. Schirmer, O. Thiemann, and M. Wohlecke, *J. Phys. Chem. Solids* 52, 185 (1991).
104. H. J. Donnerberg, S. M. Tomlinson, and C. R. A. Catlow, *J. Phys. Chem. Solids* 52, 201 (1991).
105. P. Lerner, C. Legras, and J. P. Dumas, *J. Cryst. Growth* 3-4, 231 (1968).
106. N. Iyi, K. Kitamura, F. Izumi, J. K. Yamamoto, T. Hayashi, H. Asano, and S. Kimura, *J. Solid State Chem.* 101, 340 (1992).
107. N. S. Zotov, H. Boysen, F. Frey, T. Metzger, and E. Born, *J. Phys. Chem. Solids* 55, 145 (1994).
108. E. M. Ivanova, N. A. Sergeev, and A. V. Yatsenko, *Kristallografiya* 43, 337 (1998).
109. A. V. Yatsenko, E. N. Ivanova, and A. Sergeev, *Phys. B* 240, 254 (1997).
110. A. V. Yatsenko, *Phys. Solid State* 40, 109 (1998).
111. G. S. Zhdanov, S. A. Ivanov, E. V. Kolontsova, and A. E. Korneev, *Ferroelectrics* 21, 463 (1978).
112. S. A. Ivanov, A. E. Korneev, E. V. Kolontsova, and N. Yu. Venentsev, *Kristallografiya* 23, 1071 (1978).
113. N. Zotov, F. Frey, H. Boysen, H. Lehnert, A. Hornsteiner, B. Strauss, R. Sonntag, H. M. Mayer, F. Guthoff, and D. Hohlweg, *Acta Crystallogr. B* 51, 961 (1995).
114. K. Nassau and M. E. Lines, *J. Appl. Phys.* 41, 533 (1970).
115. Y. Furukawa, K. Kitamura, E. Suzuki, and K. Niwa, *J. Cryst. Growth* 197, 889 (1999).
116. A. A. Ballman and H. Brown, *Ferroelectrics* 4, 189 (1972).
117. C. C. Battle, S. Kim, V. Gopalan, K. Barcosy, M. C. Gupta, Q. X. Jia, and T. E. Mitchell, *Appl. Phys. Lett.* 76, 2436 (2000).
118. G. Bergmann, *Solid State Commun.* 6, 77 (1968).
119. N. F. Evlanova, Moscow University, 1978, p. 160, as quoted in A. M. Prokhorov and Yu S. Kuzminov, "Physics and Chemistry of Crystalline Lithium Niobate," p. 131. Hilger, New York, 1990.
120. D. L. Staebler and J. J. Amodei, *Ferroelectrics* 3, 107 (1972).
121. N. Ohnishi and T. Lizuka, *J. Appl. Phys.* 46, 1063 (1975).
122. U. Mohideen, personal communication.
123. "Landolt-Bornstein: Numerical Data and Functional Relationships in Science and Technology, New Series" (K.-H. Hellwege, Ed.), Vol. 3, Chap. 16, p. 160. Springer-Verlag, Berlin, 1981.
124. K. H. Hellwege, in "Crystal and Solid State Physics" Landolt-Bornstein, New Series, Group III (T. Mitsui and S. Nomura, Eds.), Vol. 16. Springer-Verlag, Berlin, 1981.
125. B. Steiner, M. Kuriyama, R. C. Dobbryn, and U. Laor, *J. Res. Natl. Bur. Stand.* 93, 577 (1988).
126. M. Kuriyama, B. W. Steiner, and R. C. Dobbryn, *Annu. Rev. Mater. Sci.* 19, 183 (1989).
127. B. Steiner, M. Kuriyama, and R. C. Dobbryn, *Prog. Cryst. Growth Charact.* 20, 189 (1990).
128. B. Steiner and R. C. Dobbryn, *Am. Ceram. Soc. Bull.* 70, 1017 (1991).
129. V. Gopalan, S. Kim, and B. Steiner, *Appl. Phys. Lett.* 77, 1774 (2000).
130. L. Galambos, Stanford University, personal communication.
131. A. Itagi, V. Gopalan, A. Saxena, P. Swart, T. E. Schlesinger, and D. D. Stancil, unpublished.
132. V. Gopalan, S. S. A. Gerstl, A. Itagi, T. E. Mitchell, Q. X. Jia, T. E. Shlesinger, and D. D. Stancil, *J. Appl. Phys.* 86, 1638 (1999).
133. V. Gopalan and T. E. Mitchell, *J. Appl. Phys.* 85, 2304 (1999).
134. V. Gopalan and T. E. Mitchell, *J. Appl. Phys.* 83, 941 (1998).
135. S. Chao and C.-C. Hung, *Appl. Phys. Lett.* 69, 3803 (1996).
136. H. Cerva, P. Pongratz, and P. Stalicky, *Philos. Mag. A* 54, 199 (1986).
137. T. Nozawa and S. Miyazawa, *Jpn. J. Appl. Phys.* 35, 107 (1996).
138. J. D. Venables, *Appl. Phys. Lett.* 25, 254 (1974).
139. P. V. Lambeck and G. H. Jonker, *J. Phys. Chem. Solids* 47, 453 (1986).
140. R. Lohkemper, H. Neumann, and G. Arlt, *J. Appl. Phys.* 68, 4220 (1990).
141. P. T. Brown, G. W. Ross, R. W. Eason, and A. R. Pogosyan, *Opt. Commun.* 163, 310 (1999).
142. R. C. Miller and G. Weinreich, *Phys. Rev.* 117, 1460 (1960).
143. S. Zhu et al., *J. Appl. Phys.* 77, 5481 (1995).
144. W. J. Merz, *Phys. Rev.* 95, 690 (1954).
145. R. C. Miller and A. Savage, *Phys. Rev.* 115, 1176 (1959).
146. E. G. Fesenko, A. F. Semenchov, and V. G. Gavril'yachenko, *J. Appl. Phys.* 34, 3255 (1963).
147. K. Onuki, N. Uchida, and T. Saku, *J. Opt. Soc. Am.* 62, 1030 (1972).
148. M. Avrami, *J. Chem. Phys.* 8, 212 (1940).
149. E. Betzig and J. K. Trautman, *Science* 257, 151 (1967).
150. E. K. H. Salje and Y. Ishibashi, *J. Phys. Condens. Matter* 8, 8477 (1996).
151. J. Paddila, W. Zhong, D. Vanderbilt et al., *Phys. Rev. B* 53, R5969 (1996).
152. R. E. Loge and Z. Suo, *Acta Mater.* 44, 3429 (1996).
153. V. P. Sergeev, E. A. Budovskikh, L. B. Zuev, and G. I. Gol'denberg, *Sov. Phys. Crystallogr.* 31, 361 (1986).
154. J. D. Venables, *Appl. Phys. Lett.* 25, 254, 1974.
155. N. Ohnishi and T. Lizuka, *J. Appl. Phys.* 46, 1063 (1975).
156. W. L. Holstein, *J. Cryst. Growth* 171, 477 (1997).
157. K. Kitamura and Y. Furukawa, personal communication.
158. L. E. Levine, K. L. Narayan, and K. F. Kelton, *J. Mater. Res.* 12, 124 (1997).
159. V. Gopalan, T. E. Mitchell, and K. E. Sickafus, *Solid State Commun.* 109, 111 (1999).
160. V. Gopalan, Q. X. Jia, and T. E. Mitchell, *Appl. Phys. Lett.* 75, 16 (1999).
161. S. Kim and V. Gopalan, unpublished.

Chapter 3

BISMUTH VANADATE: A VERSATILE FERROELECTRIC MATERIAL

K. Shantha, K. B. R. Varma

Materials Research Centre, Indian Institute of Science, Bangalore-560 012, India

Contents

1. Introduction	116
1.1. Structural Origin of Ferroelectricity in the Aurivillius Family of Oxides	116
1.2. Application Potential of Bismuth Vanadate	117
2. Crystal Structure of Bismuth Vanadate	117
2.1. The $\text{Bi}_2\text{O}_3\text{-V}_2\text{O}_5$ Phase Diagram	117
2.2. The Role of Stoichiometry	117
2.3. Room-Temperature Structure (α -Phase) of BiV	117
2.4. Polymorphs of Bismuth Vanadate	118
3. Bismuth Vanadate Ceramics and Single Crystals	119
3.1. Preparation	119
3.2. Dielectric Properties	120
3.3. Ferroelectric and Pyroelectric Properties	122
4. Nanocrystalline Bismuth Vanadate	123
4.1. Mechanochemical Synthesis of Nano-BiV Powders	124
4.2. Stabilization of the Paraelectric Tetragonal Phase at Room Temperature	124
4.3. Optical Properties of Nano-BiV Powders	124
5. Microstructure-Property Correlation in BiV Ceramics	124
5.1. Grain-Size Control	125
5.2. Grain-Boundary Modification	127
5.3. Grain-Orientation	129
6. Bismuth Vanadate Thin-Films	131
6.1. Pulsed Laser Deposition (PLD)	131
6.2. RF Sputtering	131
6.3. Dielectric Properties	131
7. Compositional Modification of Bismuth Vanadate	131
7.1. Doping Mechanisms	132
7.2. Influence of Doping on Polar Properties	132
7.3. Influence of Doping on Ionic Conductivity	132
8. Composites Based on Bismuth Vanadate	133
8.1. Glass Nanocomposites (GNC)	133
8.2. Diphasic Ceramic Composites	134
9. Nonpolar Applications	135
10. Future Directions	136
11. Conclusions	136
Acknowledgments	136
References	136

Handbook of Advanced Electronic and Photonic Materials and Devices, edited by H.S. Nalwa

Volume 4: Ferroelectrics and Dielectrics

Copyright © 2001 by Academic Press

All rights of reproduction in any form reserved.

ISBN 0-12-513754-0/\$35.00